Doctoral Dissertation

Data scientific structure search for ternary hydride high-temperature superconductors

PENG SONG

Supervisor: Ryo Maezono

Graduate School of Advanced Science and Technology
Japan Advanced Institute of Science and Technology

Information Science

September, 2023

Abstract

Superconducting hydrides have attracted significant attention in recent years due to their potential for achieving high-temperature superconductivity under high-pressure conditions. The discovery of high-temperature superconductivity in hydrogen-rich materials, such as sulfur hydride (H_3S) and phosphine (PH_3), has spurred extensive research efforts to explore novel superconducting hydride materials with the aim of understanding the underlying mechanisms and optimizing their properties for practical applications. Ternary hydrides, comprising multiple metal elements and hydrogen, offer promising candidates for further investigation due to their complex compositions and the possibility of fine-tuning their electronic and structural properties. In this context, this thesis focuses on the investigation of ternary hydrides composed of lanthanum, yttrium, magnesium, scandium, and cerium to uncover new stable phases with enhanced superconducting transition temperatures.

In the La-Y-H system, we investigated their phase and structural stabilities under high pressure using a genetic algorithm and $ab-initio$ calculations. Our study revealed that $Pm\bar{3}m$-$LaYH_{12}$ was unstable and identified new stable crystal structures, such as $Cmmm$-$LaYH_{12}$ and $Cmmm$-LaY_3H_{24}. The $Cmmm$ phases exhibited a T_c of approximately 140 K due to their extremely high electron-phonon coupling constant, with an increased T_c in $Cmmm$-LaY_3H_{24} attributed to the chemical pressure of Y.

For the $YMgH_x$ system, the investigation probed the structural stabilities of high-pressure $YMgH_x$ phases and their superconductivities using an evolutionary-algorithm-based crystal search combined with first-principles calculations. The study identified several stable and metastable phases, with high-T_c values ($\geq$ 77 K) predicted for H-richer phases, such as $P4/mmm$-$YMgH_8$ (124 K at 300 GPa), $Cmmm$-$YMgH_{12}$ (152 K at 250 GPa), and $Fd\bar{3}m$-$YMgH_{12}$ (190 K at 200 GPa). These phases feature clathrate structures composed of H_{14}, H_{18}, H_{24}, and H_{24} cages.

The $Mg_xSc_yH_z$ system was examined under high pressure ($100 \leq P \leq 200$ GPa), resulting in the identification of four thermodynamically stable compounds in the hydrogen-middle range, including $R\bar{3}m$-$MgScH_6$, $C2/m$-Mg_2ScH_{10}, $Immm$-$MgSc_2H_9$, and $Pm\bar{3}m$-$Mg(ScH_4)_3$. Among them, $R\bar{3}m$-$MgScH_6$ was predicted to exhibit the highest T_c (i.e., 41 K) at 100 GPa.

In the Y-Ce-H and La-Ce-H systems, the study employed the evolutionary-algorithm-based crystal structure prediction method and first-principles calculations to investigate stability and superconductivity under high pressure. Several stable phases were identified, with T_c values predicted using the Allen-Dynes-modified McMillan formula to be 122 K for $R\bar{3}m$-$YCeH_{20}$ at 300 GPa, 116 K for $R\bar{3}m$-$LaCeH_{20}$ at 250 GPa, and 173 K for $P\bar{6}m2$-$YCeH_{18}$ at 150 GPa. The pressure required to stabilize $P\bar{6}m2$-$YCeH_{18}$ can be reduced to 150 GPa, suggesting an accessible condition for its high-pressure synthesis.

This comprehensive study offers valuable insights into high-temperature superconducting materials and their potential applications. The identification of stable and metastable

phases in these ternary hydride systems and the prediction of their superconducting transition temperatures enhance our understanding of these materials.

Keywords: First-principles calculation, Pressure effects, Structural properties, Hydride ,Superconducting phase transition

Contents

Abstract i

1 Introduction 1
- 1.1 Background . . . 1
- 1.2 Motivation . . . 11
- 1.3 Chapter Organization . . . 13

2 Methodology 15
- 2.1 Crystal structure properties . . . 15
  - 2.1.1 Density function theory . . . 17
  - 2.1.2 Strongly correlated electron systems . . . 23
  - 2.1.3 Evolutionary Crystal Structure Prediction . . . 35
  - 2.1.4 Convex Hull and Thermodynamic Stability . . . 39
  - 2.1.5 The finite displacement and lattice dynamical stability . . . 40
- 2.2 Electron-Phonon Coupling and Superconductivity . . . 43
  - 2.2.1 Electron-Phonon Interaction . . . 43
  - 2.2.2 Eliashberg Theory and McMillan's Equation . . . 44
  - 2.2.3 Allen-Dynes-modified McMillan Formula . . . 46
  - 2.2.4 Computational Software Packages for Electron-Phonon Coupling . . . 46
- 2.3 Parallelism and Computational Cost . . . 48

3 High-T_c superconducting hydrides formed by LaH_{24} and YH_{24} cage structures as basic blocks 52
- 3.1 Motivation and Research Background . . . 52
- 3.2 Computational Details . . . 54
- 3.3 Results . . . 55
- 3.4 Discussion . . . 56
- 3.5 Conclusions . . . 60

4 The systematic study on the stability and superconductivity of Y-Mg-H compounds under high pressure 62
- 4.1 Motivation . . . 62
- 4.2 Research Background . . . 63
- 4.3 Method . . . 65
- 4.4 Results and discussion . . . 67
  - 4.4.1 Pressure-dependent phase diagram . . . 67
  - 4.4.2 Superconducting transition temperatures . . . 71
  - 4.4.3 Structural and chemical bonding analyses . . . 76

4.5 Conclusion . . . 79

5 High-Pressure Mg-Sc-H Phase Diagram and Its Superconductivity from First-Principles Calculations 81
5.1 Motivation . . . 81
5.2 Research Background . . . 82
5.3 Computational Methods . . . 84
5.4 Results and discussion . . . 85
5.4.1 First-principles phase diagram of Mg-Sc-H system . . . 85
5.4.2 Predicted superconductivity of Mg-Sc-H system . . . 90
5.5 Conclusion . . . 96

6 Potential high-T_c superconductivity in $YCeH_x$ and $LaCeH_x$ under pressure 98
6.1 Motivation . . . 98
6.2 Research Background . . . 99
6.3 Method . . . 102
6.4 Results and discussion . . . 105
6.4.1 Phase stability and crystal structural of $YCeH_x$ and $LaCeH_x$ . . . 105
6.4.2 Electronic Properties and Superconductivity . . . 109
6.4.3 Discussion . . . 112
6.5 Conclusion . . . 117

7 Conclusion and Future Works 118
7.0.1 Conclusion . . . 118
7.0.2 Future Works . . . 119

Biblography 121

Publications 146

List of Figures

1.1 The left panel presents a visual representation of the Diamond Anvil Cell (DAC), a fundamentally indispensable instrument within the realm of high-pressure physics, known for its compatibility with a wide array of spectroscopic techniques and in situ characterization of electrical and magnetic attributes. The middle panel provides a schematic layout of the DAC, detailing essential components including the anvil seats, gasket, and pistons. The right panel displays a photograph of an extant Diamond Anvil Cell, offering a tangible view of the equipment in question. (Figure adapted from ref [1]) 3

1.2 Right panel: The panel depicts the crystal structure of H_3S, demonstrating the arrangement and bonding of atoms. Left panel: The panel portrays the temperature-dependent magnetization of sulfur hydride at a pressure of 155 GPa in two different conditions - zero-field cooled (ZFC) and 20 Oe field cooled (FC) modes (represented by black circles). The characteristic critical temperature (T_c) under these conditions is noted to be 203 K. (Figure from ref [2, 3]) 4

1.3 Left panel: The panel illustrates the clathrate structures of REH_6, REH_9, and REH_{10}. Here, small and large spheres are representative of Hydrogen and Rare Earth (RE) atoms, respectively. The figure further explicates the RE-centered H_{24}, H_{29}, and H_{32} cages for REH_6, REH_9, and REH_{10}, serving to elucidate their respective symmetries and geometrical arrangements. Right panel: The panel showcases the superconducting transitions in LaH_{10} samples, synthesized from La + H_2 mixtures. These transitions are measured at various pressures and critical temperatures (T_c), thus highlighting the material's superconducting properties under different conditions. (Figure from ref [4, 5]) 6

1.4 The graph representing enthalpy versus pressure for LaH_{10} structures, intentionally excludes zero-point energy calculations. The Born-Oppenheimer energy surface, denoted by $V(\mathrm{R})$, displays local minima for distorted structures, showcasing the potential energy of the system in various configurations. Conversely, when considering quantum effects, the configurational energy surface, denoted by $E(\mathrm{R})$, coalesces into a singular, highly symmetric phase represented by the $Fm\bar{3}m$ crystallographic point group. This suggests that quantum fluctuations play a crucial role in determining the stable phase under given conditions. (Figure from ref [6]) 8

2.1 Self-consistent iterative flowchart of HK equation. 20

2.2 Jacob's Ladder of DFT towards Chemical Accuracy.(Figure from ref [7]) . 23

2.3 Left panel: Flowchart of the evolutionary algorithm for crystal structure prediction. Right panel: Schematic representation of specific crossover and mutation operations in the structures. 36
2.4 The relationships of the maximum atoms of the system and the possible of the combinations. 51

3.1 Clathrate structure of $LaYH_{12}$ (left panel, at 200 GPa) and LaY_3H_{24} (right panel, at 180 GPa) with $Cmmm$, consisting of La-centered H_{24} cages and Y-centered H_{24} cages. Each H_{24} cage is surrounded by six squares and eight hexagons. These structural models were drawn by using VESTA. [8] . . . 53
3.2 Convex hull of La–Y–H at pressures of 100 GPa, 200 GPa, and 300 GPa. 57
3.3 Comparisons of candidate structure enthalpies for $LaYH_{12}$ [panel (a)] and LaY_3H_{24} [panel (b)]. Such structures giving higher values than those of 'YH_6 + LaH_6' (for the left panel), '3(YH_6) + LaH_6' (for the right), and '$LaYH_{12}$ + 2(YH_6)' (for the right), are predicted to exhibit instability toward decomposition into these binary compounds. 57
3.4 Phonon dispersions, projected phonon densities of states, and Eliashberg spectral function for $Cmmm$-$LaYH_{12}$ clathrate at 200 GPa. 57
3.5 Phonon dispersions and projected phonon densities of states for $Pm\bar{3}m$-$LaYH_{12}$ at 180 GPa. 59
3.6 Structures and the XRD patterns of (a) $Im\bar{3}m$-YH_6, (b) $Pm\bar{3}m$-$LaYH_{12}$, and (c) $Cmmm$-$LaYH_{12}$. 60

4.1 Pressure-dependent phase diagram of the Y-Mg-H system. The phases shown here are both thermodynamically and dynamically stable, while metastable phases do not appear. 68
4.2 Convex hull diagrams of $YMgH_x$ relative to $YMgH_2$ and H-$C2/c$ [9] at the pressure of (a) 100 GPa, (b) 150 GPa, (c) 200GPa, (d) 250 GPa, and (e) 300 GPa. To ensure the relative stabilities of $YMgH_x$ compounds, the relative stability of $YMgH_2$ against several decomposition possibilities is also given in (f). 69
4.3 The clathrate structure of (a) $P4/mmm$-$YMgH_6$, (b) $P4/mmm$-$YMgH_8$, (c) $Cmmm$-$YMgH_{12}$, (d) $Fd\bar{3}m$-$YMgH_{12}$. 70
4.4 Predicted superconducting transition temperatures (T_c) of the stable and metastable phases at certain pressures ($\mu^* = 0.1$). 71
4.5 Phonon band structures and Eliashberg spectral functions for (a) $P6_3/mmc$-$YMgH_3$, (b) $Imma$-$YMgH_5$, (c) $P4/mmm$-$YMgH_6$, (d)$P4/mmm$-$YMgH_8$, (e) $Cmmm$-$YMgH_{12}$, and (f) $Fd\bar{3}m$-$YMgH_{12}$. 74
4.6 Electronic band structures for (a) $P6_3/mmc$-$YMgH_3$, (b) $Imma$-$YMgH_5$, (c) $P4/mmm$-$YMgH_6$, (d)$P4/mmm$-$YMgH_8$, (e) $Cmmm$-$YMgH_{12}$, and (f) $Fd\bar{3}m$-$YMgH_{12}$. 75
4.7 The contour plots of electron localization function (ELF) on (a) (200) plane of $P4/mmm$-$YMgH_6$, (b) (100) plane of $P4/mmm$-$YMgH_8$, (c) (100) plane of $Cmmm$-$YMgH_8$, and (d) (100) plane of $Fd\bar{3}m$-$YMgH_{12}$ with an isosurface value of 0.5. 78
4.8 Partial (electronic) density of states (pDOS) and projected crystal orbital Hamilton population (pCOHP) for (a) $P4/mmm$-$YMgH_6$, (b) $P4/mmm$-$YMgH_8$, (c) $Cmmm$-$YMgH_{12}$, and (d) $Fd\bar{3}m$-$YMgH_{12}$. 79

5.1 (a) Ternary convex hulls of the Mg-Sc-H system at a pressure of 200 GPa. (b) and (c) are the convex hulls of Gibbs free energy at 0K and a finite temperature (1000 K), respectively. The stable and metastable phases are shown by circles and diamond, respectively. 86
5.2 The enthalpy per atom of $(ScH_3)_{1-x}$ $\frac{1}{2}(MgH_2 + MgH_4)_x$ as a function of x at the pressure of 100, 150, and 200 GPa, where x is defined as $N_{ScH_3}/\left(N_{ScH_3} + \frac{1}{2}\left(N_{MgH_2} + N_{MgH_4}\right)\right)$. The stable phase and the metastable phase are connected by solid and dashed lines, respectively. 86
5.3 Phase diagram of Mg-Sc-H in the pressure range of 100–200 GPa. 87
5.4 Predicted crystal structures of (a) $R\bar{3}m$-$MgScH_6$, (b) $C2/m$-Mg_2ScH_{10}, (c) $Immm$-$MgSc_2H_9$, (d) $Pm\bar{3}m$-$MgSc_3H_{12}$ at 200 GPa. Bottom panels show the corresponding contour plots of electron localization function (ELF) in these structures. 88
5.5 Electronic band structures and atom-projected electronic density of states of (a) $R\bar{3}m$-$MgScH_6$, (b) $C2/m$-Mg_2ScH_{10}, (c) $Immm$-$MgSc_2H_9$, (d) $Pm\bar{3}m$-$MgSc_3H_{12}$ at 200 GPa. 91
5.6 Phonon dispersion and atom-projected phonon density of states (pDOS), and Eliashberg spectral of (a) $R\bar{3}m$-$MgScH_6$, (b) $C2/m$-Mg_2ScH_{10}, (c) $Immm$-$MgSc_2H_9$, (d) $Pm\bar{3}m$-$MgSc_3H_{12}$ at 200 GPa. 93
5.7 Pressure-dependent superconductivity of $R\bar{3}m$-$MgScH_6$, $C2/m$-Mg_2ScH_{10}, $Immm$-$MgSc_2H_9$, $Pm\bar{3}m$-$MgSc_3H_{12}$. (a) T_c from the McM equation, (b) EPC constant λ, (c) logarithmic phonon average ω_{log} and (d)the total DOS at the Fermi level N_{Ef}. 95

6.1 Ternary convex hulls of $YCeH_x$ and $LaCeH_x$ at 200 GPa. The stable and metastable phases are highlighted by the symbols of circles and red diamond, respectively. The right panels are the convex hull at 0 K (with the correction of zero-point energy) and 1000 K. 106
6.2 The clathrate structures of stable $YCeH_x$ and $LaCeH_x$. 107
6.3 The phonon spectra with a projection of mode-resolved EPC constant $\lambda_{q\nu}$ (red circle), atom-projected phonon density of states (PHDOS), and Eliashberg function of (a) $P\bar{6}m2$-$YCeH_{18}$ at 150 GPa, (b) $R\bar{3}m$-$YCeH_{20}$ at 300 GPa, and (c) $R\bar{3}m$-$LaCeH_{20}$ at 250 GPa. The mode-revolved EPC constant $\lambda_{q\nu}$ is defined as $\lambda_{q\nu} = \frac{\gamma_{q\nu}}{\pi\hbar N(E_F)\omega_{q\nu}^2}$, where $\gamma_{q\nu}$ is phonon linewidth, $N(E_F)$ is the DOS at the Fermi level, and $\omega_{q\nu}$ is the mode-resolve phonon frequency. 111
6.4 The Crystal Orbital Hamilton Population (COHP) of some representative atom pairs (H-H, Y-H, La-H, and Ce-H) in $P4/mmm$-YCeH8, $P\bar{6}m2$-$YCeH_{18}$, $R\bar{3}m$-$YCeH_{20}$, $P4/mmm$-$LaCeH_8$, and $R\bar{3}$m-$LaCeH_{20}$ at the pressure of 100, 150, 300, 100, and 250 GPa, respectively. 113

List of Tables

3.1 T_c (expressed in K) estimated using the Allen–Dynes formula through *ab initio* phonon calculations for $LaYH_{12}$ and LaY_3H_{24} at each pressure. λ and $\omega_{\log}$ (expressed in K) are the parameters appearing in the formula. The values of $D(\varepsilon_F)$ are expressed in [states/eV/atom]. 58

4.1 Setting of k-point meshes in the self-consistent field (SCF) calculations and that of q-point meshes in the phonon calculations for stable/metastable $YMgH_x$ phases. 67

4.2 Calculated electron-phonon coupling parameters (λ), the logarithmic average phonon frequency $\omega_{\log}$ (K), electronic density of states at the Fermi level $N(E_F)$ (in states/eV/^{3}), and superconducting critical temperatures T_c (K) with $\mu^* = 0.10$ and 0.13 for stabel/metastable $YMgH_x$ compounds at selected pressures. 72

4.3 Distances of the first nearest neighboring atomic pairs, Y–H, Mg–H, and H–H for stable/metastable $YMgH_x$ compounds at selected pressures. The units are given in Å. 77

5.1 T_c estimated by McMillan formula using first-principles phonon calculations for Mg-Sc-H at each pressure. λ and $\omega_{\log}$ are the parameters appearing in the formula. 96

6.1 Superconducting transition temperature (T_c) predicted by the original McMillan formula (abbreviated to McM), the Allen-Dynes-modified McMillan (McM) formula (abbreviated to AD), and the model (i.e., Eq. (6.9)) proposed by Belli *et al.*, (abbreviated to ELF) for A-Ce-H (A = Y and La) at some selected pressures. Accordingly, the values of some key parameters contained in these formulas and model are also listed. 117

Chapter 1

Introduction

1.1 Background

Physics, as a fundamental discipline, continually pushes the boundaries of our understanding of the universe and the forces that govern it. As we explore the frontiers of this ever-evolving field, new discoveries and breakthroughs continue to challenge our perceptions and open up new horizons for scientific exploration. From the subatomic realm of quantum mechanics to the vast expanse of cosmology, cutting-edge research in physics has the potential to transform our world in ways that were once unimaginable.

At the forefront of these advances are various areas of investigation, including high-energy particle physics, condensed matter physics, quantum computing, and astrophysics, among others. Each of these subfields delves into distinct aspects of our physical reality, unraveling the mysteries of the cosmos and the building blocks of matter. These pursuits are driven by a collective desire to comprehend the fundamental principles that underlie the fabric of the universe and to harness this knowledge for the betterment of humanity.

In recent years, numerous innovations have emerged from the vanguard of physics research. For instance, the discovery of the Higgs boson at CERN's Large Hadron Collider has provided crucial insights into the origin of mass in elementary particles, while the detection of gravitational waves by the LIGO-Virgo collaboration has confirmed the existence of ripples in spacetime, as predicted by Einstein's general theory of relativity. [10]

As the field of physics continues to advance and uncover the fundamental principles governing the natural world, certain areas of research have emerged at the forefront, capturing the attention of scientists and the broader community alike. One such area is the study of superconductivity, a remarkable phenomenon that holds the potential to revolutionize diverse domains, from energy systems to quantum computing. As a critical intersection between condensed matter physics, materials science, and cutting-edge technology, the pursuit of understanding and exploiting superconductivity represents a vital step forward in pushing the boundaries of what is possible within the realm of modern physics.

Superconductivity embodies an intriguing physical occurrence, fundamentally typified by the absolute cessation of electrical resistivity in specified materials upon reaching a temperature below a defined critical threshold (T_c). The discovery of superconductivity in 1911 by Heike Kamerlingh Onnes has sparked tremendous scientific interest and driven significant technological advancements. Over the past century, researchers have made great strides in understanding the underlying mechanisms of superconductivity and have discovered a wide range of superconducting materials, including metallic alloys, ceramic compounds, and organic materials. [11]

One class of materials that has garnered significant attention in recent years is metal hydrides. Metal hydrides are compounds formed between hydrogen and another element, typically a metal. The identification of high-temperature superconductivity in copper oxide-based ceramics, commonly known as cuprates, in 1986 marked a significant watershed in superconductor research, ultimately catalyzing the pursuit of materials capable of exhibiting superconductivity at ambient conditions. [12] While cuprates and other unconventional superconductors have pushed the boundaries of T_c, they still require cryogenic cooling to achieve superconductivity, which limits their practical applications.

The theoretical postulation by Ashcroft in 2004, which proposed high-T_c superconductivity in doped metal hydrides, marked a pivotal turning point in the domain of superconductivity. This suggested that compounds abundant in hydrogen could potentially hold the key to accomplishing superior T_c values. [13] This prediction was based on the notion

that hydrogen, being the lightest element, could give rise to strong electron-phonon coupling, which is one of the key mechanisms responsible for conventional superconductivity. Furthermore, the high-frequency phonon modes associated with hydrogen could enable higher T_c values compared to heavier elements.

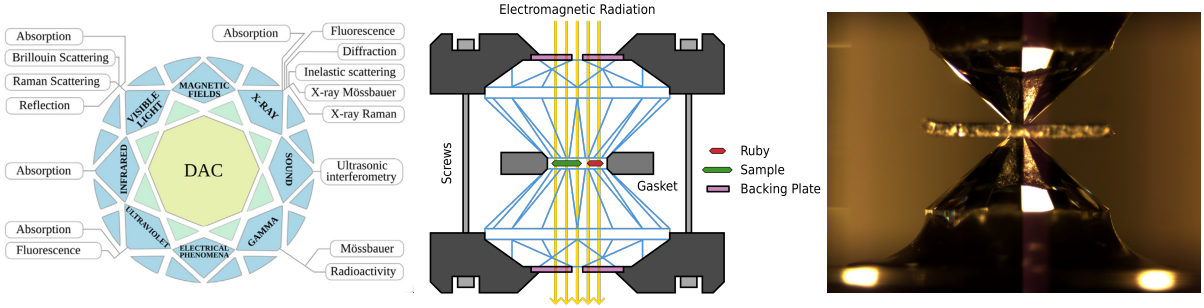

Figure 1.1: The left panel presents a visual representation of the Diamond Anvil Cell (DAC), a fundamentally indispensable instrument within the realm of high-pressure physics, known for its compatibility with a wide array of spectroscopic techniques and in situ characterization of electrical and magnetic attributes. The middle panel provides a schematic layout of the DAC, detailing essential components including the anvil seats, gasket, and pistons. The right panel displays a photograph of an extant Diamond Anvil Cell, offering a tangible view of the equipment in question. (Figure adapted from ref [1])

Metallic hydrides typically require extremely high pressures to form stable compounds. Under these demanding conditions, the diamond anvil cell (DAC) has emerged as a cornerstone of high-pressure research, enabling scientists to study matter under extreme density conditions. [14] By achieving and maintaining such high pressures, DACs have facilitated the investigation of metallic hydrides, paving the way for a deeper understanding of their properties and potential applications in various scientific fields. [15]

DACs exhibit exceptional versatility, accommodating an extensive assortment of characterization techniques that span various spectroscopy methods and probes (Fig. 1.1). Furthermore, contemporary DACs enable the synthesis and concurrent in situ characterization of materials across an expansive temperature spectrum, from millikelvin to several thousand kelvin [16]. The operational principle of a DAC in high-pressure experiments is essentially straightforward, entailing the placement and subsequent compression of the sample between two diamond surfaces. Nonetheless, more intricate experimental designs

may involve a complex interplay of numerous components and microscopic elements.

These advancements in DAC technology have made it possible to achieve pressures up to 300 GPa with relative ease, opening the door to the high-pressure synthesis of hydride materials. Under these extreme conditions, researchers can synthesize hydrogen-rich materials with unique electronic and structural properties conducive to superconductivity. As such, the ongoing development of high-pressure experimental apparatus, particularly the DAC, has played a crucial role in the investigation and synthesis of hydride superconductors under extreme conditions.

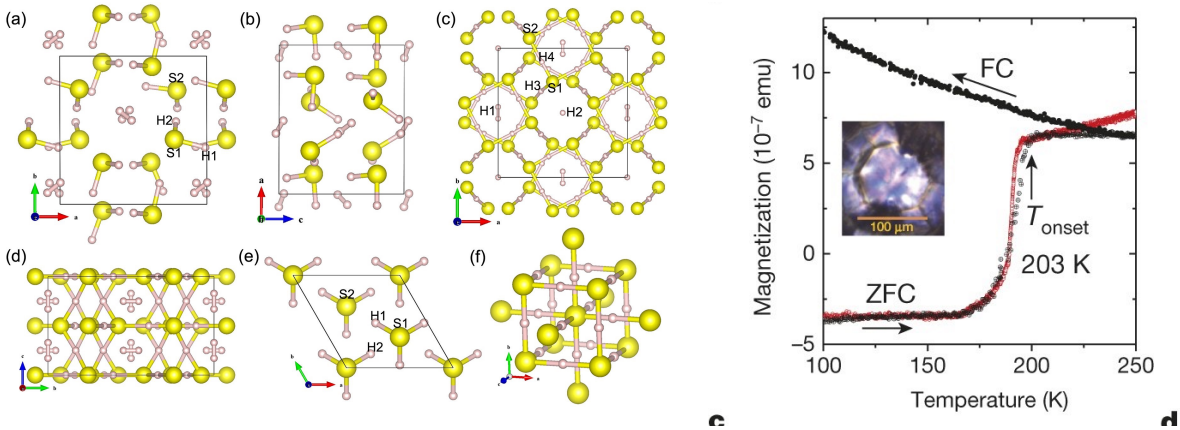

Figure 1.2: Right panel: The panel depicts the crystal structure of H_3S, demonstrating the arrangement and bonding of atoms. Left panel: The panel portrays the temperature-dependent magnetization of sulfur hydride at a pressure of 155 GPa in two different conditions - zero-field cooled (ZFC) and 20 Oe field cooled (FC) modes (represented by black circles). The characteristic critical temperature (T_c) under these conditions is noted to be 203 K. (Figure from ref [2, 3])

The subsequent experimental studies in this area have led to the discovery of several high-pressure hydride superconductors. The first significant breakthrough occurred in 2015 when Drozdov et al. [2] reported the observation of superconductivity in sulfur hydride (H_3S) at pressures above 150 GPa and T_c values as high as 203 K, setting a new record for the highest T_c in a hydrogen-rich compound.(Fig. 1.2) This milestone discovery not only validated Ashcroft's prediction but also opened a new avenue for the exploration of novel high-T_c superconducting materials based on metal hydrides.

Since then, research on hydride superconductors has been growing rapidly, and a variety of hydride compounds have been synthesized and characterized under high-pressure

conditions. Some notable examples include phosphorus hydrides, germanium hydrides, and lanthanum hydrides, which have exhibited T_c values well above those of conventional superconductors [5, 17]. These discoveries have prompted the scientific community to further investigate the potential of hydrides as high-T_c superconductors and to explore the underlying mechanisms responsible for their extraordinary superconducting properties.

In addition to the experimental discoveries, theoretical studies have played a crucial role in advancing our understanding of hydride superconductors. First-principles calculations based on density functional theory (DFT) have been employed to predict and understand the crystal structures, electronic properties, and phonon-mediated superconductivity in various hydride systems [4, 18]. These theoretical studies have not only provided valuable insights into the electronic and phononic properties of hydrides, but have also guided experimentalists in their search for new high-T_c materials.

One of the key challenges in the study of hydride superconductors is the necessity to work under extreme high-pressure conditions. These conditions pose experimental difficulties and often require the use of sophisticated techniques, such as diamond anvil cells, to generate the required pressures [19]. Moreover, the high-pressure environment can lead to complex phase behavior and chemical reactions, making the interpretation of experimental results challenging. Consequently, close collaboration between experimentalists and theoreticians is essential for making progress in this field.

Despite the remarkable advancements in hydride superconductors, the ultimate goal of achieving room-temperature superconductivity remains elusive. However, the rapid progress in recent years has sparked renewed optimism that this goal may eventually be attainable. One promising avenue for achieving higher T_c values is to explore novel hydrogen-rich materials, such as hydrogen-dense alloys or hydrogen clathrates [4]. These materials are expected to exhibit unique electronic and structural properties that could potentially give rise to unconventional superconductivity.

In the latest experimental investigations, high-temperature superconductors, such as CaH_6 [20], LaH_{10} [5], YH_9 [21], YH_6 [22], and CeH_9 [23], have been observed to adopt clathrate structures, as depicted in Figure 2.4. These clathrate architectures signifi-

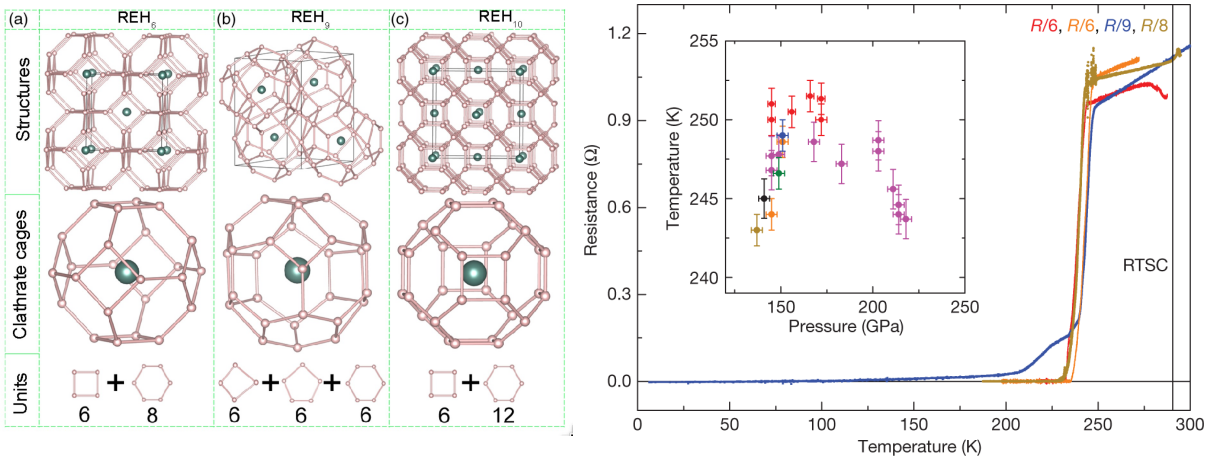

Figure 1.3: Left panel: The panel illustrates the clathrate structures of REH_6, REH_9, and REH_{10}. Here, small and large spheres are representative of Hydrogen and Rare Earth (RE) atoms, respectively. The figure further explicates the RE-centered H_{24}, H_{29}, and H_{32} cages for REH_6, REH_9, and REH_{10}, serving to elucidate their respective symmetries and geometrical arrangements. Right panel: The panel showcases the superconducting transitions in LaH_{10} samples, synthesized from La + H_2 mixtures. These transitions are measured at various pressures and critical temperatures (T_c), thus highlighting the material's superconducting properties under different conditions. (Figure from ref [4, 5])

cantly enhance the density of electronic states derived from hydrogen at the Fermi level. A positive correlation exists between the superconductivity of hydrides and the density of electronic states, which consequently promotes the electron-phonon coupling effect, leading to high T_c values. [4] Moreover, these materials generally form solid compounds with hydrogen under ambient pressure, further increasing the potential for high-pressure synthesis. [24] Nonetheless, not all such materials can achieve high T_c values. In compounds composed of rare-earth metals and hydrides, the intrinsic T_c values display a strong correlation with the types of electrons present. [25–27] For instance, the presence of f-electrons in elements like Eu augments their magnetic properties. [27] Owing to the competition between magnetism and superconductivity, the T_c values of hydrides with clathrate structures exhibit a negative correlation with the f-electron content. [28] The magnetic properties introduced by the f-electrons tend to suppress superconducting behavior, rendering the attainment of high-T_c values in hydrides with considerable f-electron contributions a challenging endeavor. [29]

Following the recent advancements in experimental techniques for studying hydride

superconductors under high-pressure conditions, our understanding of their superconducting properties has deepened significantly. These techniques, such as resistance and magnetic susceptibility measurements, synchrotron x-ray diffraction, Raman and infrared spectroscopy, and nuclear magnetic resonance (NMR) spectroscopy, have provided valuable insights into the crystal structures, electronic properties, and superconducting phase transitions of various hydride compounds.

As these measurement techniques have progressed, they have revealed crucial details about the nature of hydride superconductors. For instance, synchrotron x-ray diffraction has allowed researchers to identify the structural phases of hydrides, as well as the pressure-induced changes in their lattice parameters. Raman and infrared spectroscopy have been instrumental in probing the vibrational properties of hydrides, which in turn has helped to elucidate the electron-phonon coupling mechanism responsible for superconductivity in these materials.

Nuclear magnetic resonance (NMR) spectroscopy has provided insights into the local electronic environments of hydrides, shedding light on the unconventional superconducting pairing mechanisms and the role of hydrogen in these compounds. Additionally, resistance and magnetic susceptibility measurements have enabled the precise determination of superconducting transition temperatures (T_c) and critical magnetic fields, which are essential for understanding the limitations and potential applications of hydride superconductors. These advances in experimental techniques, combined with ongoing theoretical studies, have significantly expanded our knowledge of the complex interplay between structural, electronic, and vibrational properties in hydride superconductors. This deeper understanding will ultimately help guide the development of new materials with even higher T_c values and improved superconducting performance.

An additional vital facet of hydride superconductor research pertains to deciphering the parameters that regulate the T_c in these materials. While robust electron-phonon coupling and high-frequency phonon modes are acknowledged as critical constituents for high-T_c superconductivity, the exact dynamics between these elements and their consequential role in shaping the T_c remains an area of ongoing inquiry [13]. Furthermore, the

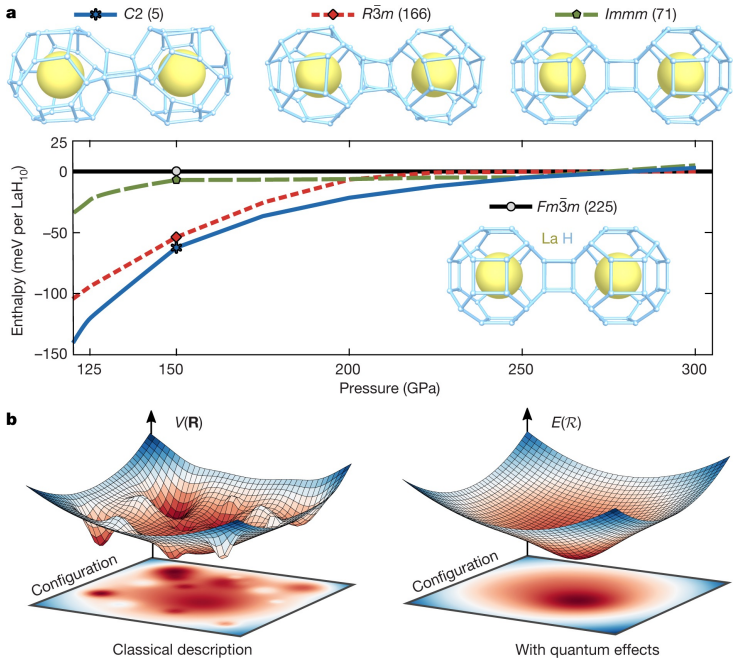

Figure 1.4: The graph representing enthalpy versus pressure for LaH_{10} structures, intentionally excludes zero-point energy calculations. The Born-Oppenheimer energy surface, denoted by $V(\mathrm{R})$, displays local minima for distorted structures, showcasing the potential energy of the system in various configurations. Conversely, when considering quantum effects, the configurational energy surface, denoted by $E(\mathrm{R})$, coalesces into a singular, highly symmetric phase represented by the $Fm\bar{3}m$ crystallographic point group. This suggests that quantum fluctuations play a crucial role in determining the stable phase under given conditions. (Figure from ref [6])

potential influence of other factors, such as unconventional pairing mechanisms, necessitates exploration in order to procure a more holistic comprehension of hydride superconductors.

The identification of superconductivity at 200 K in the hydrogen sulfide system under high pressures [2] effectively underscored the capacity of hydrogen-rich materials to act as high-temperature superconductors. The recent theoretical projections concerning rare-earth hydrides encased in hydrogen cages [5], coupled with the ensuing synthesis of LaH_{10} exhibiting a superconducting critical temperature (T_c) of 250 K, have progressively edged these materials towards the long-cherished aspiration of achieving room-temperature superconductivity.

Employing both electrical and X-ray diffraction assessments, a faintly pressure-dependent T_c for LaH_{10} has been observed, occurring between 137 and 218 GPa. This relates to a structure which demonstrates a face-centered cubic pattern of lanthanum atoms [30]. Over this pressure range, quantum atomic fluctuations appear to stabilize an extremely symmetrical $Fm\bar{3}m$ crystal structure. This observed structure, which aligns with experimental data, boasts a remarkably high electron-phonon coupling constant of 3.5. [6] Despite *abinitio* classical computations predicting potential distortion of this $Fm\bar{3}m$ structure at pressures below 230 GPa, resulting in a multifaceted energy landscape, the integration of quantum effects portrays it as the authentic ground-state structure (Fig. 1.4). The convergence between the theoretically computed and experimentally measured T_c values reinforces the supposition that this particular phase instigates the superconductivity detected at 250 K.

The significance of quantum fluctuations poses a substantial challenge to numerous crystal structure predictions propounded for hydrides within a classical framework, which presently steer the experimental pursuit for room-temperature superconductivity [6]. Moreover, quantum effects have been determined to be pivotal for the consolidation of solids characterized by high electron-phonon coupling constants, which could conversely be destabilized by the intense electron-phonon interaction, thereby mitigating the pressures necessitated for their synthesis.

Additionally, the evolution of novel computational resources and algorithms will bear a pivotal role in hastening the discovery of innovative high-T_c superconducting materials. Machine learning methodologies, specifically, bear substantial potential for prognosticating the properties of materials and directing the quest for novel superconductors. By harnessing the potency of computational strategies and high-throughput screening, the expansive chemical terrain of hydrides can be adeptly navigated, thereby enabling the identification of promising candidates suitable for experimental scrutiny.

Recent investigations have leveraged machine learning techniques to pinpoint superconducting hydrides that function nearer to ambient conditions, such as RbH_{12}, which exhibits a T_c of up to 115 K at 50 GPa, thereby broadening the functional pressure-temperature spectrum of hydride superconductors towards ambient conditions. [31] Concurrently, contemporary machine-learning methodologies have been harnessed to refine the Allen–Dynes formula for T_c predictions, accommodating for more generalized configurations of the α^2F function and delivering improved performance for higher-T_c superconductors. [32] This novel equation possesses the potential to supplant the Allen–Dynes formula for forecasting higher-temperature superconductors.

An alternative approach involves the establishment of a guideline for predicting the maximum T_c, derived from the electronic structure of metal atoms. This principle has facilitated the focused exploration of hydride systems and the anticipation of new higher hydrides in various systems under high pressures. [29] The study discovered that the highest-temperature superconducting hydrides are composed of metals residing in the "lability belt", which roughly spans between the 2nd and 3rd groups of the Periodic Table. A specifically designed neural network was utilized to gauge the upper boundary for T_c of hydrides and has demonstrated high precision in forecasting T_c for various hydrides. This guideline, which is based on the regular behavior of the maximum attainable critical temperature as a function of the number of d + f electrons, facilitates focused predictions concerning the emergence of new high-T_c superconductors.

The exploration of superconductivity within hydrides encapsulates an invigorating frontier in condensed matter physics and the realm of materials science. The prospect

of unearthing materials boasting higher T_c values and unique superconducting attributes has intrigued researchers on a global scale. Through the integration of experimental, theoretical, and computational methodologies, the domain of hydride superconductors is primed for achieving substantial advancements in our comprehension of superconductivity, thereby setting the stage for the development of transformative technologies.

1.2 Motivation

Recent strides in high-temperature superconducting hydrides have incited a wave of interest within the field of condensed matter physics, predominantly driven by their prospective applications in energy, power transmission, and maglev transportation. Among diverse hydride systems, compressed polyhydrides are regarded as propitious contenders for high-T_c superconductors, due to the high vibrational frequencies furnished by hydrogen atoms and the inclusion of supplementary elements, which deliver the requisite pre-compression for the whole system to preserve its metallic and superconducting state even under diminished pressures.

Many theoretical and experimental studies have confirmed the potential for high-T_c in compressed polyhydrides. The majority of these investigations have focused on binary compounds, with some syntheses reporting the achievement of high-T_c, such as LaH_{10} (260 K at 200 GPa), YH_6 (224 K at 166 GPa), and TH_{10} (159 K at 174 GPa), among others. These remarkable achievements have spurred the research community to further explore the underlying mechanisms of high-T_c superconductivity in compressed polyhydrides and investigate novel compounds with potentially higher T_c values. [1]

A primary challenge in progressing the field of high-temperature superconducting hydrides resides in diminishing the pressure prerequisites whilst retaining high-T_c values. Such a modification would render these materials more suitable for practical implementations, as the considerable pressures presently necessitated restrict their broader applicability. Consequently, concerted efforts persist in identifying novel hydride systems that demonstrate high-T_c superconductivity under more feasible pressure conditions. Inves-

tigations into superconductivity in compressed hydrides are receiving notable attention, motivated by measurements of high critical temperatures proximal to ambient conditions, initiated with the observations of LaH_{10} within the range of 170–190 GPa. Nonetheless, the pressures mandated for the synthesis of these high-T_c superconducting hydrides continue to be exceedingly high. [5]

Recent explorations into the La-B-H system under pressure, leveraging particle-swarm intelligence structure-search techniques in conjunction with first-principles calculations, have yielded encouraging findings. Intriguingly, the hydrogen atoms in $LaBH_8$ were observed to engage with B atoms in a fashion reminiscent of that in H_3S. Lattice dynamics computations suggest that $LaBH_7$ and $LaBH_8$ attain dynamic stability at pressures as modest as 109 and 48 GPa, respectively. [33] Additionally, both phases were projected to exhibit superconductivity, possessing a critical temperature T_c of 93 K and 156 K at 110 GPa and 55 GPa, correspondingly. An alternative promising trajectory in the quest for high-T_c superconductors incorporates the ternary Li_2MgH_{16} compound. [34] This compound has been characterized as possessing an alternate clathrate structure, with a strikingly elevated estimated T_c of 473 K at 250 GPa, potentially enabling the attainment of room-temperature or even higher-temperature superconductivity. The ternary Li_2MgH_{16} compound emulates a Li- or electron-doped binary hydride of MgH_{16}. The progenitor hydride contains H_2 molecules and does not demonstrate strong superconducting properties. The introduced surplus electrons disrupt the H_2 molecules, augmenting the proportion of atomic hydrogen relative to the progenitor hydride, a necessity for stabilizing the clathrate structure or other high-T_c formations.

These discoveries imply that ternary hydride systems possess substantial promise for realizing high-temperature superconductivity under reduced pressures. This paves the way for fresh research directions and prospects in fabricating practical high-T_c superconducting materials. The current outcomes offer direction for forthcoming experiments that aim to produce hydride superconductors with both diminished synthesis pressures and elevated T_c, underlining the promising potential of ternary and even more intricate hydride systems within this domain.

This study predominantly zeroes in on binary hydride systems, aiming to explore their capacity to yield stable and superconducting ternary hydride compounds. By unravelling the mechanisms underpinning the genesis of ternary hydrides, we endeavour to elucidate the elements contributing to their enhanced superconductivity and stability. A thorough examination of binary superconducting hydrides has yielded meaningful insights. Initially, the "lability belt" within Mendeleev's Table, which encapsulates the majority of high-temperature superconducting metal hydrides, includes Sc-Y-La-Ce (d1 belt), Mg-Ca-Sr-Ba-Ra (d0 belt), and Th. [29] These elements manifest orbital populations that are sensitive to their atomic environments, attributable to their electronic lability, culminating in substantial electron-phonon coupling. Subsequently, a profound correlation with superconducting properties is evident in the count of d- and f-electrons. An augmentation in the number of d- and f-electrons precipitates a significant decline in the superconducting attributes of hydrides. Specifically, as the quantity of f-electrons escalates, the critical temperatures of lanthanoid and actinoid hydrides wane almost uniformly.

In light of these discoveries, ternary hydrides incorporating elements from the d0 belt, d1 belt, and Th are deemed highly promising candidates for high-T_c superconductors. The manifestation of superconductivity at 253 K in lanthanum yttrium ternary hydrides stands as a prime exemplar. Therefore, the main objectives of this study are to identify the most suitable pairings between the d0 and d1 belts, utilize an evolutionary algorithm to pinpoint their stable phases under pressures achievable through high-pressure experiments, and utilize the McMillan formula to investigate whether these stable ternary hydrides exhibit high-temperature superconductivity. This investigation will deliver crucial guidance and novel synthesis concepts for future high-pressure experiments, potentially paving the way for the unveiling of innovative high-temperature superconducting ternary hydrides consisting of lanthanum, yttrium, magnesium, scandium, and cerium.

1.3 Chapter Organization

The dissertation is organized as follows:

- Chapter 2 outline the comprehensive methodology that combines density functional theory, evolutionary crystal structure prediction, thermodynamic stability analysis, lattice dynamical stability, and electron-phonon coupling evaluations using density functional perturbation theory and Migdal-Eliashberg theory to investigate superconductivity in ternary hydrides.

- Chapter 3 High-T_c superconducting hydrides formed by LaH_{24} and YH_{24} cage structures as basic blocks

- Chapter 4 The systematic study on the stability and superconductivity of Y-Mg-H compounds under high pressure

- Chapter 5 High-Pressure Mg-Sc-H Phase Diagram and Its Superconductivity from First-Principles Calculations

- Chapter 6 Potential high-T_c superconductivity in $YCeH_x$ and $LaCeH_x$ under pressure

- Chapter 7 Conclusion serves as a summary of the previous Chapters 3, 4, 5, and 6.

Chapter 2

Methodology

2.1 Crystal structure properties

The study of the properties of crystal structures is vital to understanding the physical and chemical characteristics of materials, including their potential for superconductivity. This understanding is especially relevant when researching ternary hydrides, where predicting these properties can aid in identifying promising candidates for high-temperature superconductivity. Several computational methodologies facilitate this examination, including density functional theory (DFT), evolutionary crystal structure prediction (CSP), convex hull plotting, and lattice dynamical stability analyses.

Density functional theory (DFT) is an influential computational instrument employed across materials science, condensed matter physics, and chemistry for executing electronic structure computations. [35] It empowers researchers to derive vital data about the ground-state characteristics of materials, including atomic geometry, electronic densities, and bonding traits. DFT calculations are fundamental in comprehending the electronic and structural qualities of ternary hydrides, crucial aspects for their superconductivity potential.

Evolutionary crystal structure prediction (CSP) offers a proficient way to navigate the expansive configurational space of crystal structures, targeting the most thermodynami-

cally stable phases. [36] Integrating DFT calculations with globally optimized algorithms, evolutionary CSP can conduct systematic searches for the lowest-energy structures of specific compounds. This method has shown considerable success in foreseeing novel crystal structures in ternary hydrides, providing valuable direction for experimental initiatives towards promising high-temperature superconductors.

Upon predicting stable crystal structures, it is paramount to scrutinize their thermodynamic stability, ensuring their synthesis and sustainability under experimental conditions. The construction of a convex hull, a visual representation of energetically favorable phases at specific pressures and compositions, is a frequent method. By graphing the formation energies of various crystal structures in relation to their composition, researchers can pinpoint the lowest-energy structures that form the phase diagram's "convex hull." This process is instrumental in understanding the thermodynamic stability of ternary hydrides and focusing the hunt for potential high-temperature superconductors.

Beyond thermodynamic stability, an assessment of lattice dynamical stability is required for the predicted structures. This can be achieved using the finite displacement technique, which calculates the phonon frequencies of the materials by modifying the atoms' positions within the crystal lattice and studying the resultant forces. Phonon frequencies offer insights into the vibrational attributes of materials, which are integral to their mechanical and dynamical stability. A stable crystal structure should exhibit no imaginary phonon frequencies, implying that the material is both mechanically and dynamically stable under the existing conditions.

The examination of lattice dynamical stability can also shed light on the electron-phonon coupling strength, a pivotal factor for the superconducting properties of materials. An intense electron-phonon coupling can trigger high-temperature superconductivity, marking it an essential parameter to evaluate when determining the potential of ternary hydrides as efficient superconductors.

A thorough analysis of crystal structure properties is key to unlocking the potential of ternary hydrides as high-temperature superconductors. Utilizing computational tech-

niques such as density functional theory, evolutionary crystal structure prediction, convex hull formulation, and lattice dynamical stability analysis, we can glean substantial insights into these materials' structural, electronic, and vibrational characteristics. This understanding is instrumental in not only identifying potential candidates for high-temperature superconductivity but also offering crucial direction for experimental endeavors in fabricating and characterizing innovative ternary hydride superconductors.

2.1.1 Density function theory

Density functional theory (DFT) is a quantum mechanical technique extensively employed to examine the electronic structure of diverse materials, encompassing solids, molecules, and intricate systems. [37] Since its inception in the mid-20th century, DFT has become a cornerstone in condensed matter physics, materials science, and computational chemistry, delivering crucial insights into the fundamental properties of an array of systems. DFT's effectiveness stems from its capability to efficiently simulate the many-body issue of interacting electrons within a material, achieving a harmony between computational expense and precision.

The Hohenberg-Kohn theorem is fundamental to DFT, asserting that a system's ground-state characteristics are uniquely defined by its electron density. [38] This density can be determined by minimizing a universal functional - the energy functional, with respect to the electron density. However, the exact shape of this functional remains elusive, and several approximations have been devised to facilitate tractable DFT computations. The Local Density Approximation (LDA) and the Generalized Gradient Approximation (GGA) are among the most prevalent approximations, utilized successfully across a broad spectrum of materials. [39]

DFT computations furnish essential data about the electronic and structural attributes of materials, including atomic geometry, electronic densities, band structures, and bonding traits. Understanding these properties is vital to comprehend the behavior of materials, including their mechanical, electronic, magnetic, and optical features. In the context of

high-temperature superconducting ternary hydrides, DFT is pivotal in describing these materials' ground-state properties, which have a direct impact on their superconductivity potential.

Along with the electronic structure, DFT can also be applied to compute the vibrational properties of materials via density functional perturbation theory (DFPT). [40] This method facilitates the calculation of phonon frequencies, delivering information about lattice dynamics and the electron-phonon coupling strength, a crucial determinant in the superconducting characteristics of materials. A robust electron-phonon coupling can engender high-temperature superconductivity, thereby rendering DFT-based phonon calculations a crucial aspect in the pursuit of novel superconducting materials.

Hohenberg-Kohn theorem

The Hohenberg-Kohn (HK) theorem forms an integral principle in density functional theory (DFT), laying the groundwork for the investigation of the electronic structure of multi-body systems. [38] The HK theorem shows that the ground-state attributes of a system are solely determined by its electron density, which simplifies the many-body issue to a more manageable form.

The HK theorem is comprised of two parts:

1. The initial portion of the theorem declares that the ground-state electron density, $\rho(\mathbf{r})$, determines the external potential, $V_{\text{ext}}(\mathbf{r})$, exclusively up to a constant. As the external potential sets the Hamiltonian of the system, this implies that properties in the ground state, such as energy, are functionals of the electron density. This can be mathematically expressed as:

$$E[\rho(\mathbf{r})] = T[\rho(\mathbf{r})] + V_{\text{ee}}[\rho(\mathbf{r})] + \int \rho(\mathbf{r}) V_{\text{ext}}(\mathbf{r}) d\mathbf{r} \tag{2.1}$$

Here, $E[\rho(\mathbf{r})]$ is the total energy functional, $T[\rho(\mathbf{r})]$ is the kinetic energy functional, $V_{\text{ee}}[\rho(\mathbf{r})]$ is the electron-electron interaction energy functional, and $\rho(\mathbf{r})$ is the ground-

state electron density.

2. The latter portion of the theorem presents a variational principle for the ground-state energy. It states that for any trial electron density, $\rho'(\mathbf{r})$, which integrates to the correct number of electrons, the total energy functional evaluated with the true ground-state electron density, $\rho(\mathbf{r})$, is always lower or equal to the functional evaluated with the trial density:

$$E[\rho(\mathbf{r})] \leq E[\rho'(\mathbf{r})] \tag{2.2}$$

This variational principle permits us to search for the ground-state electron density by minimizing the total energy functional with respect to the electron density. The Hohenberg-Kohn theorem sets the foundation for density functional theory, asserting that the ground-state properties of a system are uniquely determined by its electron density. This notion allows us to express total energy as a functional of electron density and offers a variational principle for locating the ground-state electron density through the minimization of energy functional. The HK theorem thereby considerably simplifies the many-body problem of interacting electrons, paving the way for efficient computational methodologies to study electronic structures and properties of materials.

Kohn-Sham equation

The Kohn-Sham (KS) equations are a crucial component of density functional theory (DFT), delivering a practical method to tackle many-body electronic structure problems. [41] The KS equations convert the complex many-body problem into a series of single-particle Schrödinger-like equations, facilitating more manageable computational efforts.

The Kohn-Sham approach's central concept is to portray the system of interacting electrons as a fictitious non-interacting system, in which each electron operates in an effective potential. This effective potential comprises the external potential, the Hartree potential, and the exchange-correlation potential. The effective Kohn-Sham potential can be expressed as:

$$V_{\mathrm{KS}}(\mathbf{r}) = V_{\mathrm{ext}}(\mathbf{r}) + V_{\mathrm{H}}[\rho(\mathbf{r})] + V_{\mathrm{XC}}[\rho(\mathbf{r})] \tag{2.3}$$

Here, $[\rho(\mathbf{r})]$ is the Hartree potential, and $V_{\mathrm{XC}}[\rho(\mathbf{r})]$ is the exchange-correlation potential.

The Kohn-Sham equations for the single-particle wavefunctions, $\psi_i(\mathbf{r})$, are as follows:

$$[-\frac{\hbar^2}{2m}\nabla^2 + V_{\mathrm{KS}}(\mathbf{r})]\psi_i(\mathbf{r}) = \epsilon_i\psi_i(\mathbf{r}) \tag{2.4}$$

where ϵ_i are the single-particle eigenvalues. By solving the Kohn-Sham equations, we can obtain the single-particle wavefunctions, which can then be utilized to calculate the electron density as:

$$\rho(\mathbf{r}) = \sum_{i=1}^{N} |\psi_i(\mathbf{r})|^2 \tag{2.5}$$

where N is the number of electrons in the system. The specific flow schematic of the KS equation is displayed in the figure below (Fig. 2.1).

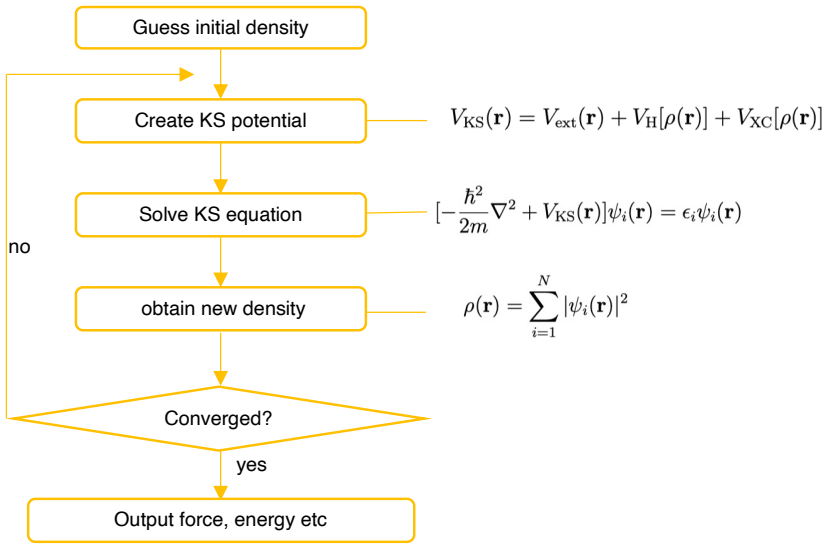

Figure 2.1: Self-consistent iterative flowchart of HK equation.

The significant challenge in solving the Kohn-Sham equations is approximating the exchange-correlation potential, $V_{\mathrm{XC}}[\rho(\mathbf{r})]$. Various approximations have been proposed

over the years, including the local density approximation (LDA), the generalized gradient approximation (GGA), and hybrid functionals, each with its own advantages and limitations.

The Kohn-Sham equations offer a practical approach to solving electronic structure problems within density functional theory by transforming the many-body problem into a set of single-particle equations. The KS equations incorporate the effective potential, which includes the external potential, the Hartree potential, and the exchange-correlation potential. The main challenge in the Kohn-Sham formalism is approximating the exchange-correlation potential, with various approximations developed over the years to balance accuracy and computational cost.

Exchange-correlation functional

In the subsequent chapter, we will explore the exchange-correlation functional, a critical component in the Kohn-Sham equation. This functional represents the combined effects of exchange and correlation energies due to the interactions between electrons in a many-electron system. The main objective is to approximate this functional as accurately as possible to acquire reliable electronic structure and total energy calculations.

One of the most common methods for constructing exchange-correlation functionals is the density functional theory (DFT) framework. In DFT, the system's energy can be expressed as a functional of the electron density:

$$E[\rho] = T[\rho] + V_{ne}[\rho] + V_{ee}[\rho], \tag{2.6}$$

where $E[\rho]$ represents the total energy, $T[\rho]$ the kinetic energy, $V_{ne}[\rho]$ the nuclear-electron interaction energy, and $V_{ee}[\rho]$ the electron-electron interaction energy.

The electron-electron interaction energy can be further divided into classical electrostatic (Coulomb) energy and the exchange-correlation energy:

$$V_{ee}[\rho] = V_C[\rho] + E_{xc}[\rho], \tag{2.7}$$

where $V_C[\rho]$ represents the classical electrostatic (Coulomb) energy and $E_{xc}[\rho]$ the exchange-correlation energy.

Over the years, various exchange-correlation functionals have been proposed to approximate the $E_{xc}[\rho]$ term, each with its unique strengths and limitations. According to J.P. Perdew's categorization, exchange-correlation functionals can be divided into the following types (Fig. 2.2):

1. Local Density Approximation (LDA): In this simplest approximation, the exchange-correlation energy density depends solely on the local electron density. LDA functionals are computationally efficient and often yield reasonably accurate results for simple systems. However, they might not perform well for more complex systems or those with strong electron correlation effects.

2. Generalized Gradient Approximation (GGA): GGA functionals consider not only the local electron density but also its gradient. This extra information allows for a more accurate description of the exchange-correlation energy in many cases. GGA functionals have been found to perform better than LDA functionals for a broader range of systems, particularly those with inhomogeneous electron densities.

3. Meta-GGA [42]: These functionals take a step further by incorporating the second derivatives of the electron density (i.e., the Laplacian) and the kinetic energy density. Meta-GGA functionals aim to further improve the description of exchange-correlation energy, especially for systems with rapidly varying electron densities.

4. Hybrid Functionals [43]: Hybrid functionals are a combination of Hartree-Fock exchange and DFT exchange-correlation functionals. By integrating a fraction of the exact exchange energy from Hartree-Fock theory, hybrid functionals can often provide more accurate results than their pure DFT counterparts. Popular hybrid functionals include B3LYP and PBE0.

5. Range-separated Hybrid Functionals [44]: These functionals are designed to treat short-range and long-range interactions separately. By combining different exchange-correlation functionals for different interaction ranges, range-separated hybrids can provide a more accurate description of systems with both strong and weak interactions.

6. Double Hybrid Functionals [45]: Double hybrid functionals combine DFT exchange-correlation functionals, Hartree-Fock exchange, and a perturbative treatment of the correlation energy. These functionals can be highly accurate but are also computationally more demanding than the other categories.

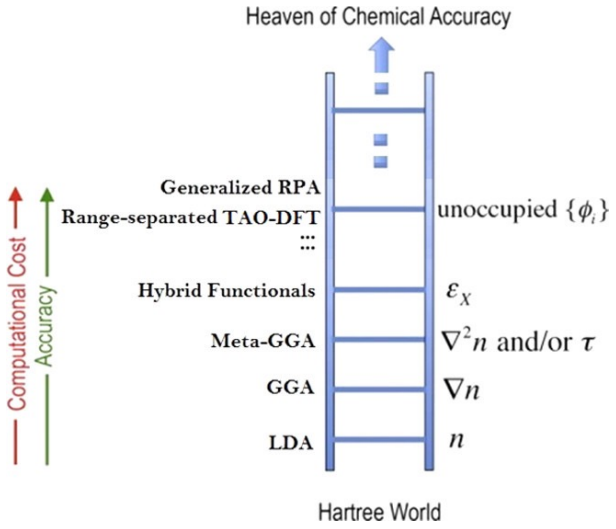

Figure 2.2: Jacob's Ladder of DFT towards Chemical Accuracy.(Figure from ref [7])

2.1.2 Strongly correlated electron systems

The one system under consideration in this thesis involves Lanthanum/Yttrium-Cerium-Hydrogen (La/Y-Ce-H), with the electronic configuration of Cerium (Ce) being [Xe] $4f^1 5d^1 6s^2$. The electronic configuration of Ce significantly influences its chemical and physical properties, and it plays a critical role in interactions within the La/Y-Ce-H system.

The orbitals of particular interest are the d and f orbitals of Ce. The strong on-site Coulomb repulsion among the electrons in these localized orbitals makes the standard DFT description inadequate. These localized electron states are not accurately described in traditional DFT, which can lead to inaccurate descriptions of the electronic structure, leading to erroneous predictions of various properties such as magnetism and conductivity.

A correction to DFT is necessary for a more accurate description of the system. The DFT+U method is designed for such a scenario. [46] It incorporates the Hubbard U

correction, accounting for the strong on-site Coulomb interactions in the d and f orbitals of Ce. The Hubbard model within DFT+U introduces an additional term in the energy functional that is dependent on the occupation number of these localized states, effectively treating the strong correlation and improving the description of the electronic structure of the system.

Therefore, this section primarily elaborates on the details of the DFT+U method. Given the unique electronic configuration of Cerium (Ce) and the importance of accurate descriptions of its d and f orbitals in the La/Y-Ce-H system, the utilization of DFT+U becomes indispensable. This method, with its ability to account for the strong on-site Coulomb interactions, can yield a more accurate electronic structure and other related properties of the system, aligning better with experimental observations.

Self-interaction Correction

Self-interaction Correction (SIC) is a computational method used in quantum mechanics primarily to correct the description of electron interactions. In many theoretical computations, such as the Hartree-Fock method and Density Functional Theory (DFT), the behavior of each electron is considered independently. However, this simplified description overlooks the correlation effects among electrons, meaning, the behavior of one electron impacts the behaviors of others, leading to self-interaction errors.

To rectify these errors, Perdew et al. [47] introduced the method of self-interaction correction. Simply put, the self-interaction correction method involves subtracting each electron's interaction with itself during calculations, thereby more accurately simulating the interactions between electrons.

$$E_{XC}^{SIC} = E_{XC}^{LDA}[\rho(r)] - \sum_{i,\delta} f_i^{\delta}(E_H[\rho_i^{\delta}(r)] - E_{XC}^{LDA}[\rho_i^{\delta}(r)]) \tag{2.8}$$

where $\delta = \uparrow,\downarrow$ denotes the spin index, f_i^{δ} is the occupation number of orbital $\phi_i^{\delta}(r)$, and $\rho_i^{\delta} = \phi_i^{\delta}(r)^2$. The SIC-LDA method, while physically intuitive and capable of entirely rectifying the self-interaction error for single-electron systems, encounters significant diffi-

culties with N-electron systems, both theoretically and pragmatically. Initial issues arise from its origination in basic physical ideas, which results in a lack of a robust theoretical foundation encompassing many-body systems. Furthermore, the non-invariance of the SIC-LDA total energy under a unitary transform of occupied orbitals introduces substantial complications to the method's application and obscures the physical interpretation of single-particle orbitals. Finally, while the SIC-LDA method can effectively address the self-interaction error prevalent in single-electron systems, it falls short in correcting the same for many-electron systems, an error tied to the noncompliance with the piecewise linearity (PWL) condition of the ground state total energy as a function of electron number. [48]

Incorporating the SIC-LDA method into extended systems is complex due to the ineffectiveness of SIC with Bloch-type orbitals and the necessity for localized Wannier-type orbitals to achieve considerable physical effects. Svane and his team implemented this approach using linear muffin-tin orbitals (LMTOs) coupled with the atomic sphere approximation (ASA) and applied it successfully to a range of strongly correlated d- and f-electron systems. [49] Notably, this technique allowed first-principles predictions of the valence of lanthanide ions across different compounds and addressed the qualitative failure of LDA/GGA for strongly correlated systems by integrating the pseudo-potential approach.

On the front of continuous improvements to the SIC-LDA method, various efforts have been made, most notably the attempts to restore the PWL condition. For instance, Marzari, Cococcioni, and collaborators proposed the use of Koopmans compliant (KC) functionals on standard semilocal functionals, improving the description of electronic properties without compromising structural property accuracy and atomization energies - a stark contrast to the original SIC-LDA approach. Simultaneously, Yang and his team introduced a scaling correction scheme to restore the PWL condition for finite systems, enhancing the description of ionization potentials and electron affinities. However, these advancements are mostly tested for molecular systems with closed-shell electronic configurations, and their applicability to extended systems, especially their potential to improve

the description of strongly correlated systems, remains unclear.

Exact exchange

The hybrid functional approach incorporates a portion of the exact (Fock) exchange (α_{HF}) into the LDA/GGA exchange-correlation, thereby yielding superior accuracy relative to both the LDA/GGA and the HF method. [43] This method has achieved substantial success in molecular systems by leveraging the error cancellation between LDA/GGA and HF-exchange. Although its application to extended systems such as solids and surfaces has been more recent, the approach is gaining traction, notably following the development of screened hybrid functionals by Heyd et al. These functionals, combining the screened exchange (SEX) approach with the PBE0 hybrid functional [50], enhance the band gaps of semiconductors and address the delocalization error of LDA/GGA, providing a more accurate portrayal of structural, energetic, and electronic properties in many strongly correlated systems.

Nevertheless, the hybrid functional approach does come with significant theoretical challenges. The results hinge on the considered fraction of the exact exchange or the screening strength, and parameters are often experimentally fitted for optimal performance, detracting from the approach's purely first-principles nature. Furthermore, its performance can be inconsistent across different systems or properties, limiting its predictive power.

These constraints have stimulated recent attempts to create new hybrid functionals, featuring system-specific parameters that auto-tune by imposing constraints like Koopmans' theorem. These tuned functionals significantly enhance the depiction of electronic and optical properties in molecular systems. However, extending such strategies to broader systems is challenging due to a lack of clear guidelines. Recent suggestions to improve this include empirically determining the system-specific mixing parameter with the density gradient or optimizing the value of α_{HF} based on its relation to the calculated dielectric constant. These methodologies mainly aim to refine band gap predictions for standard semiconductors, but their effectiveness for strongly correlated systems remains

to be verified.

DFT + U [51]

Density Functional Theory (DFT) is known for undervaluing band gaps, prompting some to question its universality and leading to various solutions, including the well-known DFT+U. The 'U' here, often related to 'Hubbard's U', represents site-specific repulsion strength in the Hubbard model. This model clarifies that antiferromagnetism manifests through energy gains from a 'virtual intermediate state' in antiparallel spin pairs.

However, the Hubbard model's clarity sometimes leads to misconceptions about DFT+U. For instance, in the Hubbard model, 'U = 0' implies no electron-electron interactions. This notion can lead to incorrect interpretations such as 'DFT does not include electronic correlation' and 'the U parameter forcibly adds electron correlation to DFT'. Importantly, DFT inherently accounts for electron-electron interactions and correlation effects, with the 'U' parameter in DFT+U serving as an exchange effect correction.

Misunderstandings from the Hubbard model that 'conduction band drops due to lack of U, causing undervalued band gaps' are common. In reality, band gap underestimation stems from damage in self-interaction cancellation, with the more accurate depiction being 'the valence band rises, causing undervalued gaps'. Here, the valence band's energy levels are overvalued due to overcounted repulsion, and the conduction band doesn't rise, narrowing the gap.

In these "metal-insulators," the band gap occurs between bands of the same orbital character, such as 3d character, arising from crystal field splitting or Hund's rule. The insulating character of the ground state originates from the intense Coulomb repulsion between electrons, forcing them into a state of atomic-like orbital localization (Mott localization). This localization-inducing Coulomb potential is represented by the term "U," and in conditions of strong localization, electrons are restricted from free atomic movement, instead "hopping" between neighboring atoms. The hopping mechanism, with an amplitude denoted as t, is proportional to the dispersion (the bandwidth) of the valence electronic states. The formation of the energy gap, therefore, can be characterized by

the competition between the Coulomb potential U between 3d electrons and the transfer integral t of the tight-binding approximation of 3d electrons between neighboring atoms. Including an additional z term, which represents the number of nearest neighbor atoms, the band gap can be written as [52]:

$$E_{gap} = U - 2zt \tag{2.9}$$

The inadequacy of the band model in describing these systems has led to the formulation of alternative models. One strategy to resolve the underestimation of the gap involves introducing an adjustment term to the potential when the contribution to self-interaction (j = i), which causes the bias, is involved. This corresponds to DFT+U, where the U parameter is used to adjust the weight of the mechanism. We will explain this in more detail in the next section.

Another more fundamental alternative is known as the exact exchange method. This method, as seen in Equation, where self-interaction cancellation was achieved with V(HF), involves evaluating the non-local integrals of V(X) in earnest to achieve self-interaction cancellation. It is a method of evaluating the integral of Equation instead of using "V(XC) represented by n(r)" like in the LDA. In this case, the exchange part is not represented by n(r), and is explicitly represented by the orbital function, so it is also called the orbital-dependent exchange method.

The exact exchange method has a high cost of integral evaluation and is not very practical, giving the impression that it doesn't go beyond the realm of basic research.

This Hamiltonian accounts for the two essential terms, t and U, with ⟨i,j⟩ representing nearest-neighbor atomic sites and ci†, cj, and ni being the electronic creation, annihilation, and number operators for electrons of spin on site i, respectively. The hopping amplitude t is proportional to the bandwidth (dispersion) of the valence electrons, while the on-site Coulomb repulsion term U is proportional to the product of the occupation numbers of atomic states on the same site. The system develops insulating characteristics when the electrons do not possess sufficient energy to overcome the repulsion potential of other

electrons on neighboring sites, i.e., when t « U. While DFT is fairly accurate in predicting electronic properties when t » U, it fails significantly for large U values. The DFT+U method provides an improvement by explicitly including the on-site Coulomb interactions in the Hamiltonian.

The Density Functional Theory plus Hubbard U (DFT+U) method, inspired by the Hubbard model, enhances the characterization of the ground state of correlated systems. Retaining its basis in DFT, it requires minimal additional effort for implementation and brings a slight computational cost increase. It can be combined with local and semilocal density functionals, offering Local Density Approximation plus U (LDA+U) and Generalized Gradient Approximation plus U (GGA+U) approaches. [53]

The additional Hubbard-like term in DFT+U is crucial for handling the strong on-site Coulomb interaction of localized electrons, especially for the d and f orbitals. The method introduces parameters U and J to quantify the strength of on-site interactions. While these parameters can be obtained from ab initio calculations, they are often determined semiempirically.

LDA+U is commonly employed to correct the approximate DFT exchange-correlation (xc) functional. The Hubbard model is applied to the strongly correlated electronic states (d and f orbitals), while the rest of the valence electrons are treated using the standard LDA approach.

Thus, the total energy of the system (E_{LDA+U}) under LDA+U becomes [53]:

$$E_{LDA+U}[\rho(r)] = E_{LDA}[\rho(r)] + E_{Hub}[n_{I\sigma mm}] - E_{dc}[n_{I\sigma}] \tag{2.10}$$

The total energy is a sum of the standard LDA energy functional (E_{LDA}), the Hubbard functional that describes the correlated states (E_{Hub}), and a "double-counting" term (E_{dc}). This term is introduced to correct for the double counting of electronic interactions already considered in the approximate xc functional.

In essence, the LDA+U method substitutes the mean-field electronic interaction in the xc functional. The exact form of the double-counting term E_{dc} can depend on the specific

implementation and approximation used in the DFT+U method. However, a common choice for the E_{dc} term, especially within the context of the Fully Localized Limit (fully localized limit) approximation [54], can be represented as:

$$E_{dc} = U \sum_{m\sigma} n_{m\sigma}^2 - J \sum_{m \neq m'} n_{m\uparrow} n_{m'\downarrow} \tag{2.11}$$

Although the FLL formulation captures Mott localization, it is not invariant under rotation of the atomic orbital basis set, creating dependency on the unitary transformation of the chosen localized basis set. Therefore, a rotationally invariant formulation has been introduced, offering full orbital dependency in the LDA+U method. [55] It often uses an effective U parameter (U_{eff} = U - J), where J is the exchange interaction term accounting for Hund's rule coupling. The U_{eff} is preferred as J has proved crucial in describing the electronic structure of certain classes of materials, typically those with strong spin-orbit coupling.

Determination of Hubbard U Parameter by linear response method

The linear response method, as proposed in the referenced paper by Cococcioni and de Gironcoli (2005), provides a first-principles approach for calculating the effective interaction parameter (Hubbard U) within the DFT+U scheme. [56] The basic principle lies in the system's response to a small perturbation in the occupation of the localized states. This is quantified by the static electronic susceptibility (χ). The Hubbard U parameter corresponds to the inverse of this quantity.

Suppose the occupation matrix n is perturbed slightly, inducing a δn change. The perturbation results in a modification in the effective potential within the DFT+U method, denoted as δV. The system's response to this perturbation is an induced change in the occupation matrix, $\delta' n$. This linear relationship can be expressed as:

$$\delta' n = \chi \delta n \tag{2.12}$$

The static electronic susceptibility, χ, quantifies the system's response to the per-

turbation. The Hubbard U parameter is the inverse of this susceptibility and is given by:

$$U = (\chi^{-1})_{mm'} \tag{2.13}$$

Here, m and m' run over the localized states. χ^{-1} is computed from the change in the effective potential and the change in the occupation number:

$$\chi^{-1} = \frac{\delta V}{\delta' n} \tag{2.14}$$

The change in the effective potential δV is obtained by taking the second derivative of the total energy with respect to the occupation number:

$$\delta V = \frac{\partial^2 E_{total}}{\partial n^2} \tag{2.15}$$

The Hubbard U parameter is determined by the system's response to a small perturbation in the occupation of the localized states. The static electronic susceptibility χ, computed from first principles, quantifies this response. The U parameter is then given by the inverse of χ. By employing this linear response approach, the U parameter can be accurately and effectively obtained for the LDA+U method, enhancing the predictability of the electronic properties of strongly correlated materials.

Spin-Orbit Coupling (SOC)

The spin-orbit interaction arises due to the coupling of the electron's spin angular momentum $\vec{S}$ with its orbital angular momentum $\vec{L}$. This interaction is represented by the following Hamiltonian in atomic units:

$$H_{SOC} = \xi(r)\vec{L} \cdot \vec{S} \tag{2.16}$$

where $\xi(r)$ is the spin-orbit coupling parameter, dependent on the electron's radial distance from the nucleus r. For atoms with high atomic numbers, the term $\xi(r)$ is no

longer negligible.

The total angular momentum $\vec{J}$ of an electron in an atom is given by the vector sum of its spin and orbital angular momenta:

$$\vec{J} = \vec{L} + \vec{S} \tag{2.17}$$

Using these definitions, we can rewrite the spin-orbit coupling Hamiltonian as:

$$H_{SOC} = \frac{1}{2}\xi(r)[\vec{J}^2 - \vec{L}^2 - \vec{S}^2] \tag{2.18}$$

The term $\xi(r)$ can be approximated as:

$$\xi(r) = \frac{1}{2m^2c^2}\frac{1}{r}\frac{dV(r)}{dr} \tag{2.19}$$

where m is the electron mass, c is the speed of light, and $V(r)$ is the central potential due to the nucleus.

In electronic structure calculations, including the SOC leads to the split of degenerate energy states and lifting of the degeneracy, which has profound impacts on the predicted physical properties of the system.

For heavy elements such as La and Ce, the SOC is strong due to their high atomic numbers, leading to a strong central potential $V(r)$ and thereby significant changes in electronic structure and physical properties when SOC is considered. The 4f electrons in these elements are strongly localized and the SOC can have significant effects on the electronic structure and consequently on the physical properties. Despite the filled 4f shell in La contributing less to the SOC, the inclusion of SOC is still necessary for a complete and accurate description of its electronic structure. For Ce, which has an active 4f electron, the SOC plays an even more substantial role in shaping the electronic structure and related properties.

How DFT+U and SOC Outperform SIC and Exact Exchange in Cerium Simulations

When dealing with strongly correlated systems like cerium, both the DFT+U and spin-orbit coupling (SOC) methods offer substantial advantages, which make them preferable choices over self-interaction correction (SIC) and exact exchange methods.

1. **DFT+U**: DFT+U is an efficient way to deal with the localized 4f electrons in cerium, as the Hubbard U parameter provides an empirical correction to account for the strong on-site Coulomb correlation. This method is computationally efficient compared to more advanced many-body techniques while still providing significant improvements over standard DFT for such systems. Moreover, the parameter U can be tuned to reproduce experimental observations, enhancing the predictive power of the method.

2. **SOC**: The inclusion of SOC is crucial for materials like cerium, where the spin and orbital motions of the electrons are strongly entangled. The SOC improves the description of the near-degenerate 4f and 5d states, an important feature in cerium, and helps to capture the correct ground state properties.

On the other hand, SIC and exact exchange methods are less commonly applied to cerium for a few reasons:

1. **SIC**: While SIC can correct the self-interaction error inherent in standard DFT, it often leads to a spatially localized description of the electronic structure, which is less appropriate for metallic cerium. Additionally, SIC usually requires much more computational effort than DFT+U or standard DFT, making it less attractive for complex systems or large-scale simulations.

2. **Exact exchange**: The exact exchange method improves the description of exchange interactions but does not treat the correlation effects adequately, which are important in cerium due to the strong electron-electron interactions. The exact exchange method also increases the computational cost significantly compared to DFT or DFT+U.

A number of studies have successfully used DFT+U and SOC for cerium and similar systems, underscoring their reliability and efficiency. For instance, Amadon et al. reported

that DFT+U combined with SOC gives a good description of the electronic structure and magnetic properties of cerium. Similarly, a study by Lanata et al. showed that the DFT+U+SOC approach can accurately capture the complex phase behavior of cerium.

Peterson et al. (2022) employed the HSE06 hybrid functional to investigate the bulk and surface properties of CeO2. [57] They concluded that this method could adequately capture the localization and delocalization of Ce's f-electrons. Haule et al. (2020) studied the electronic structures and magnetic ordering of cerium compounds using DFT+DMFT calculations. [58] Shim et al. (2021) investigated the charge-density waves and superconducting states of CeAg2Ge2 using MBPT. [59] From these studies, it can be concluded that each method has its advantages and disadvantages. Hybrid DFT excels in dealing with localized f-electrons but is computationally demanding. DMFT, on the other hand, is great for handling strongly correlated systems, but calculating the self-energy is challenging, and extending to linear response theory is not straightforward. MBPT can accurately handle electron correlations but struggles with the convergence of the perturbation series in strongly correlated systems.

In the study of cerium-hydrogen related systems, DFT+U remains the primary approach. Its effectiveness has been convincingly demonstrated by matching well with experimental results. For instance, Huang et al. used the DFT+U method to investigate CeH_2. [60] They reported that DFT+U captured the correct ground state and explained the complex magnetic properties, consistent with experimental measurements. Similarly, Chen and coworkers applied DFT+U to study the high-pressure behavior of CeH_3, showing remarkable agreement with experimental results. [61]

Despite the relative success of DFT+U in the aforementioned studies, it's worth noting that this method isn't without its limitations. The U parameter in DFT+U is not universal, necessitating case-by-case determination, which can be a tedious process. Furthermore, DFT+U can struggle with more complex cerium compounds due to limitations in capturing dynamic correlation effects.

However, for the majority of Ce-H compounds, DFT+U has demonstrated its utility and effectiveness, thus making it a reliable choice for these systems. With the contin-

ued advancement of computational techniques, we look forward to the development and application of more refined and efficient methods for studying cerium-based systems.

2.1.3 Evolutionary Crystal Structure Prediction

Evolutionary crystal structure prediction is a powerful approach for predicting the most stable crystal structures of materials under given conditions, such as temperature and pressure. [62, 63] This method relies on the principles of evolutionary algorithms, which mimic the process of natural selection and evolution in nature. In this section, we will introduce the fundamental concepts behind evolutionary crystal structure prediction, discuss the essential components of a typical algorithm, and explore some of the most widely used software packages for performing these calculations.

Fundamentals of Evolutionary Crystal Structure Prediction

The primary objective of evolutionary crystal structure prediction is to find the global minimum on the potential energy surface of a material, which corresponds to its most stable crystal structure. To achieve this goal, the algorithm generates a population of candidate structures, evaluates their fitness (usually based on their energy or enthalpy), and iteratively refines the population through a series of evolutionary operations, such as selection, crossover (mating), and mutation.

Components of Evolutionary Algorithms

A typical evolutionary algorithm for crystal structure prediction consists of the following components (Fig. 2.3):

1. **Population Initialization:** The algorithm begins by generating an initial population of candidate structures. These structures can be created randomly, based on known crystal structures, or by other heuristic methods.

2. **Fitness Evaluation:** The fitness of each candidate structure in the population is evaluated, typically by calculating its energy or enthalpy using density functional

theory or another quantum mechanical method.

3. **Selection:** A subset of the population is selected for reproduction, with a higher probability given to structures with better fitness values. This mimics the process of natural selection in which fitter individuals have a higher chance of passing their genes to the next generation.

4. **Crossover (Mating):** Pairs of selected structures undergo crossover, which combines their features to produce new offspring structures. This process is analogous to genetic recombination in nature and helps to explore the search space more efficiently.

5. **Mutation:** Random perturbations are introduced to the offspring structures to maintain diversity in the population and prevent premature convergence to local minima.

6. **Replacement:** The offspring structures replace some or all of the original population, and the process of fitness evaluation, selection, crossover, and mutation is repeated for several generations until convergence is reached.

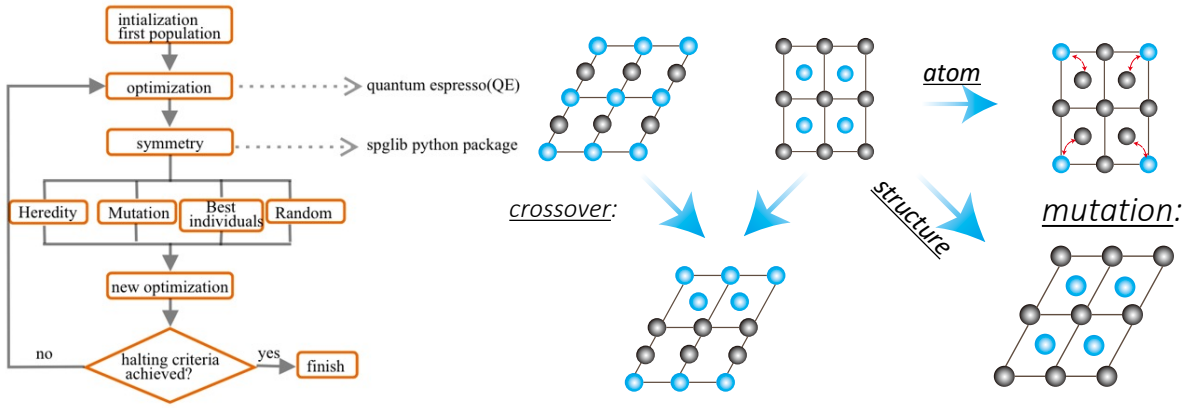

Figure 2.3: Left panel: Flowchart of the evolutionary algorithm for crystal structure prediction. Right panel: Schematic representation of specific crossover and mutation operations in the structures.

Software Packages for Evolutionary Crystal Structure Prediction

Several software packages have been developed to perform evolutionary crystal structure prediction, including:

- **USPEX (Universal Structure Predictor: Evolutionary Xtallography): [36]** USPEX is a widely used software package for predicting crystal structures and global optimization. It offers a range of features, such as variable-composition predictions, multi-objective optimization, and support for various types of chemical systems.
- **CALYPSO (Crystal Structure Analysis by Particle Swarm Optimization): [64]** CALYPSO is another popular software package for crystal structure prediction. It utilizes particle swarm optimization algorithms and can handle a variety of systems, including bulk materials, surfaces, and low-dimensional structures.
- **XTALOPT (Evolutionary Algorithms for Crystal Structure Prediction): [65]** XTALOPT is an open-source software package that implements evolutionary algorithms for predicting crystal structures. It supports various types of calculations, such as fixed-composition and variable-composition searches, and can interface with multiple quantum chemistry codes.

Evolutionary crystal structure prediction is a powerful technique for identifying stable crystal structures of materials under various conditions. It combines the principles of evolutionary algorithms with quantum mechanical calculations to explore the potential energy surface of materials effectively and efficiently. By employing this approach, researchers can gain insights into the crystal structures of novel materials, understand their properties, and potentially discover new materials with desirable characteristics for various applications. In this thesis, we primarily employ the USPEX software for crystal structure prediction. Therefore, in the following sections, we will focus on introducing the USPEX software and its practical aspects in performing evolutionary crystal structure prediction calculations. Additionally, we will discuss some case studies that highlight the utility of this method in the field of materials science.

Introduction to USPEX

USPEX (Universal Structure Predictor: Evolutionary Xtallography) is a versatile and efficient software package designed for predicting stable crystal structures of materials using evolutionary algorithms. Developed by Prof. Artem R. Oganov and his team, USPEX has become one of the most widely used tools for crystal structure prediction and has been successfully applied to various materials systems, including inorganic compounds, organic materials, and complex intermetallics.

Some notable successful examples of USPEX applications include:

1. Prediction of novel high-pressure phases of elemental boron: USPEX was used to predict a new superhard phase of boron, the γ-B28 structure, which was later experimentally confirmed using diamond anvil cell techniques. [66]

2. Discovery of superconducting hydrogen sulfide: USPEX played a crucial role in predicting the high-pressure crystal structure of H_3S, which was found to exhibit superconductivity at 203 K under high pressure, setting a new record for the highest known superconducting transition temperature at that time. [3]

3. Sodium Pentazolate: a Nitrogen Rich High Energy Density Material - USPEX was utilized to discover sodium pentazolate, a new high energy density material. In the condensed phase, the pentazole anion is stabilized by sodium cations at pressures exceeding 20 GPa, and it becomes metastable upon pressure release. [67]

4. Computational Clues into the Structure of a Promising Energy Conversion Catalyst: USPEX was applied to gain insights into the structure of an active component of iron-doped nickel oxide, which is a highly active catalyst for water oxidation. By combining USPEX search results with DFT calculations, Li and Selloni identified stable tunnel structures of nickel oxide that explain the observed mosaic texture formed during the reaction. With a better understanding of the material's structure, the researchers aim to further investigate its activity in the reaction. [68]

The core algorithm of USPEX employs a global optimization strategy based on genetic algorithms, which efficiently explores the configurational space of crystal structures. Some

key features of the USPEX software include:

1. Various search strategies: USPEX offers a range of search strategies tailored to different types of materials systems, such as fixed-composition searches, variable-composition searches, and searches for layered structures.

2. Flexibility in defining the system: Users can define the system using a combination of atoms, chemical formulas, or even partial occupancy, allowing for a wide range of materials to be investigated.

3. Advanced operators for mutation and crossover: USPEX employs sophisticated mutation and crossover operators, which help in generating diverse offspring structures and accelerating the convergence of the search process.

4. Adaptive optimization: USPEX is capable of adapting its search parameters during the course of the optimization, which helps improve the efficiency of the search process.

5. Integration with various electronic structure codes: USPEX can be interfaced with several popular electronic structure codes, such as VASP, Quantum ESPRESSO, and SIESTA, enabling users to leverage their preferred codes for energy calculations.

2.1.4 Convex Hull and Thermodynamic Stability

The concept of the convex hull is essential for evaluating the thermodynamic stability of a given crystal structure. The convex hull is a geometric representation of the lowest energy structures for a given composition, which serves as a reference for assessing the stability of other structures. In this section, we will discuss how to perform convex hull optimization, calculate the formation enthalpy, determine the energy above the hull, and assess thermodynamic stability.

The formation enthalpy (ΔH_f) of a compound is defined as the difference between the total energy of the compound and the sum of the energies of its constituent elements in their most stable form. It can be mathematically expressed as:

$$\Delta H_f = E_{compound} - \sum_i n_i E_i \tag{2.20}$$

where $E_{compound}$ is the total energy of the compound, n_i is the number of atoms of element i, and E_i is the energy of element i in its most stable form.

A negative formation enthalpy indicates that the compound is thermodynamically stable with respect to its constituent elements. However, to determine the thermodynamic stability of a compound with respect to other compounds in a given phase diagram, it is necessary to calculate the energy above the hull, denoted as E_{hull}. The energy above the hull is the vertical distance between a given compound and the convex hull.

$$E_{hull} = E_{compound} - E_{hull,reference} \tag{2.21}$$

where $E_{hull,reference}$ is the energy of the convex hull reference structure at the same composition.

A compound is considered thermodynamically stable if its energy above the hull is zero or very close to zero. In contrast, if the energy above the hull is positive, the compound is considered metastable or unstable, depending on the magnitude of E_{hull}. Typically, a smaller energy above the hull indicates a higher likelihood of experimental realization for metastable compounds. By constructing the convex hull diagram for a given system, one can readily assess the thermodynamic stability of various compounds and identify the most stable phases at different compositions.

2.1.5 The finite displacement and lattice dynamical stability

Determining the lattice dynamical stability of a crystal structure is crucial for assessing its feasibility as a material. One approach to achieve this is by employing the finite displacement method to construct the force constant matrix and calculate the phonon spectra. In this section, we will discuss how to use the finite displacement method for determining the lattice dynamical stability of a crystal structure.

The finite displacement method involves displacing atoms from their equilibrium positions by a small amount and calculating the forces that arise due to these displacements. This information is used to construct the force constant matrix, which can be mathemat-

ically represented as:

$$\Phi_{\alpha\beta}(\mathbf{R}_i - \mathbf{R}_j) = -\frac{\partial^2 E}{\partial u_{i,\alpha} \partial u_{j,\beta}}, \tag{2.22}$$

where $\Phi_{\alpha\beta}$ are the elements of the force constant matrix, E is the total energy of the crystal, $u_{i,\alpha}$ and $u_{j,\beta}$ are the displacements of atoms i and j along the α and β Cartesian directions, respectively, and $\mathbf{R}_i$ and $\mathbf{R}_j$ are the equilibrium positions of the atoms.

The force constant matrix can then be used to calculate the dynamical matrix, $D_{\alpha\beta}(\mathbf{q})$, which is a function of the wave vector, $\mathbf{q}$. The dynamical matrix can be obtained by performing a Fourier transform of the force constant matrix:

$$D_{\alpha\beta}(\mathbf{q}) = \sum_{\mathbf{R}} e^{i\mathbf{q}\cdot\mathbf{R}} \Phi_{\alpha\beta}(\mathbf{R}), \tag{2.23}$$

where $\mathbf{R}$ is the lattice vector connecting unit cells in the crystal.

Diagonalizing the dynamical matrix yields the phonon frequencies, $\omega(\mathbf{q})$, which can be used to construct the phonon dispersion relation. The lattice dynamical stability of the crystal structure can be determined by examining the phonon dispersion relation. If there are no imaginary frequencies (i.e., all frequencies are real and positive), the crystal structure is considered to be dynamically stable. However, if imaginary frequencies are present, the crystal is dynamically unstable, indicating that it is prone to undergoing a structural transformation or decomposition.

In addition to the phonon dispersion relation, the phonon density of states (DOS) is another important quantity that provides insight into the vibrational properties of a material. The phonon DOS, denoted by $g(\omega)$, describes the distribution of vibrational modes (phonons) as a function of their frequency, ω.

To calculate the phonon DOS, one can first obtain the phonon frequencies, $\omega(\mathbf{q})$, for a set of wave vectors, $\mathbf{q}$, in the first Brillouin zone. Then, the phonon DOS can be computed using the following equation:

$$g(\omega) = \frac{1}{N} \sum_{\mathbf{q},\nu} \delta(\omega - \omega_\nu(\mathbf{q})), \tag{2.24}$$

where N is the total number of wave vectors, ν is the phonon mode index, and $\delta(\cdot)$ is the Dirac delta function.

In practice, the Dirac delta function is replaced with a broadened function, such as a Gaussian or Lorentzian function, to account for the discrete sampling of the wave vectors:

$$g(\omega) = \frac{1}{N} \sum_{\mathbf{q},\nu} f(\omega - \omega_\nu(\mathbf{q})), \tag{2.25}$$

The phonon DOS provides valuable information about the vibrational properties of a material, such as the distribution of vibrational modes and their contributions to the heat capacity and thermal conductivity. By calculating the phonon DOS, researchers can gain a deeper understanding of a material's properties and predict its potential applications.

By using the finite displacement method to calculate the phonon spectra and assess the lattice dynamical stability, researchers can identify promising crystal structures and guide experimental efforts toward the synthesis of new materials.

Phonopy: A Phonon Calculation Tool

Phonopy is a widely used open-source software package for performing phonon calculations and analysis in solid-state materials. [69] It provides a user-friendly interface for computing phonon properties based on density functional perturbation theory (DFPT) and finite displacement approaches. Phonopy can be interfaced with various *ab initio* electronic structure codes, such as VASP, Quantum ESPRESSO, and ABINIT, to obtain the necessary force constants.

The main features of Phonopy include:

1. Calculation of the phonon dispersion relation and density of states (DOS). 2. Analysis of the atomic displacements in normal modes. 3. Calculation of the thermal properties, such as heat capacity, entropy, and free energy, using the quasi-harmonic approximation. 4. Determination of the group velocities and evaluation of the thermal

conductivity using the Boltzmann transport equation.

Phonopy's versatility and compatibility with popular electronic structure codes have made it an indispensable tool for researchers studying lattice dynamics and thermal properties of materials. By combining ab initio calculations with Phonopy's capabilities, researchers can gain comprehensive insights into the vibrational properties of materials and assess their stability and potential applications.

2.2 Electron-Phonon Coupling and Superconductivity

Electron-phonon coupling is a fundamental interaction in solid-state materials that plays a crucial role in various phenomena, including electrical resistivity, thermal conductivity, and most notably, superconductivity. Superconductivity arises when electrons in a material pair up to form Cooper pairs, which can move through the lattice without resistance. The electron-phonon interaction is the primary mechanism responsible for the formation of these Cooper pairs in conventional superconductors.

2.2.1 Electron-Phonon Interaction

The electron-phonon interaction is the key mechanism responsible for various phenomena in solid-state materials, including electrical resistivity, thermal conductivity, and most importantly, superconductivity. This interaction can be understood as the exchange of energy and momentum between the electrons and the vibrational motion of the crystal lattice, or phonons. [70] The strength of this coupling can be quantified by the electron-phonon coupling constant, λ, which is a critical parameter in determining the superconducting properties of a material.

In a crystal lattice, phonons are quantized vibrational modes that represent the collective motion of atoms. The interaction between electrons and phonons can be described by the electron-phonon coupling matrix element, $g_{\mathbf{k}\nu,\mathbf{k}'\nu'}$, which measures the strength of the coupling between an initial electron state $\mathbf{k}\nu$ and a final electron state $\mathbf{k}'\nu'$, mediated by a phonon with wavevector $\mathbf{q}$ and branch index j:

$$g_{\mathbf{k}\nu,\mathbf{k}'\nu'} = \langle \psi_{\mathbf{k}'\nu'} | \delta V_{\mathbf{q}j} | \psi_{\mathbf{k}\nu} \rangle, \tag{2.26}$$

where $\psi_{\mathbf{k}\nu}$ and $\psi_{\mathbf{k}'\nu'}$ are the Bloch wavefunctions of the initial and final electron states, and $\delta V_{\mathbf{q}j}$ is the change in the crystal potential due to the lattice vibration with wavevector $\mathbf{q}$ and branch index j.

The electron-phonon coupling constant, λ, can be computed from the electron-phonon coupling matrix elements and the phonon density of states, $F(\omega)$:

$$\lambda = \int_0^\infty \frac{\alpha^2 F(\omega)}{\omega} d\omega, \tag{2.27}$$

where $\alpha^2 F(\omega)$ is the Eliashberg spectral function, which represents the probability of an electron scattering by a phonon of frequency ω and is defined as:

$$\alpha^2 F(\omega) = \frac{1}{N(\epsilon_F)} \sum_{\mathbf{k}\nu,\mathbf{k}'\nu',j} |g_{\mathbf{k}\nu,\mathbf{k}'\nu'}|^2 \delta(\epsilon_{\mathbf{k}\nu} - \epsilon_F) \delta(\epsilon_{\mathbf{k}'\nu'} - \epsilon_F) \delta(\omega - \omega_{\mathbf{q}j}), \tag{2.28}$$

where $N(\epsilon_F)$ is the density of states at the Fermi level, ϵ_F, and $\omega_{\mathbf{q}j}$ is the frequency of the phonon with wavevector $\mathbf{q}$ and branch index j.

Calculating the electron-phonon coupling constant and the Eliashberg spectral function requires knowledge of both the electronic and vibrational properties of the material, which can be obtained from first-principles calculations based on density functional theory (DFT).

2.2.2 Eliashberg Theory and McMillan's Equation

Eliashberg theory is a generalization of the Bardeen-Cooper-Schrieffer (BCS) theory of superconductivity that accounts for the strong electron-phonon coupling in certain materials. The Eliashberg equations describe the behavior of the superconducting gap function, $\Delta(\omega)$, and the quasiparticle renormalization function, $Z(\omega)$, in terms of the Eliashberg spectral function, $\alpha^2 F(\omega)$. [70] However, solving the full Eliashberg equations is compu-

tationally expensive and not always necessary for predicting the critical temperature, T_c, of superconductors.

A more practical approach for estimating T_c is McMillan's formula, which is derived within the framework of the Eliashberg theory and simplifies the calculation by incorporating the electron-phonon coupling constant, λ, and the logarithmically averaged phonon frequency, ω_{log}. McMillan's formula for the critical temperature is given by:

$$T_c = \frac{\omega_{log}}{1.20} \exp\left(-\frac{1.04(1+\lambda)}{\lambda - \mu^*(1+0.62\lambda)}\right), \tag{2.29}$$

where μ^* is the Coulomb pseudopotential, which represents the effective strength of the electron-electron repulsion in the material. In superconductivity theory, the Coulomb pseudopotential (μ*) serves as an effective parameter representing the electron-electron Coulomb interaction that counteracts the phonon-mediated attraction between electrons. This parameter typically ranges from 0.1 to 0.15 for most superconductors. In the framework of Migdal-Eliashberg theory, μ^* can be computed using the following equation:

$$\mu^* = \mu \frac{1 + \ln(\varepsilon_F/\omega_D)}{1 + \ln(\varepsilon_F/\omega_{log})} \tag{2.30}$$

Here, μ^* is the Coulomb interaction, ε_F is the Fermi level, ω_D is the Debye frequency of the phonons, and ω_{log} is the logarithmically averaged phonon frequency, which can be calculated from the Eliashberg spectral function as:

$$\omega_{log} = \exp\left(\frac{2}{\lambda}\int_0^\infty \frac{\alpha^2F(\omega)}{\omega}\log\omega\, d\omega\right). \tag{2.31}$$

McMillan's formula provides a convenient way to estimate the critical temperature of superconductors from first-principles calculations, as it requires only the calculation of the electron-phonon coupling constant, λ, and the Eliashberg spectral function, $\alpha^2F(\omega)$. Despite its simplicity, McMillan's formula has proven to be remarkably accurate for many conventional superconductors and is widely used to predict the superconducting properties of novel materials.

2.2.3 Allen-Dynes-modified McMillan Formula

The Allen-Dynes-modified McMillan formula is an extension of the original McMillan formula for predicting the superconducting critical temperature (T_c) of materials, considering additional factors that can affect the superconducting properties. [71] It incorporates an enhancement factor ($f_1 f_2$), which depends on the strength of the electron-phonon coupling and other parameters, to provide a more accurate prediction of T_c.

The Allen-Dynes-modified McMillan formula is given by:

$$T_{\mathrm{c}} = \frac{\omega_{\log} f_1 f_2}{1.2} \exp\left(\frac{-1.04(1+\lambda)}{\lambda(1-0.62\mu^*)-\mu^*}\right), \tag{2.32}$$

where the enhancement factor $f_1 f_2$ is defined by:

$$\begin{aligned} f_1 f_2 &= \sqrt[3]{1+\left[\frac{\lambda}{2.46(1+3.8\mu^*))}\right]^{\frac{3}{2}}} \\ &\quad \times \left[1-\frac{\lambda^2(1-\omega_2/\omega_{\log})}{\lambda^2+3.312(1+6.3\mu^*)^2}\right]. \end{aligned} \tag{2.33}$$

The Coulomb pseudopotential μ^* is used to account for the instantaneous repulsion between electrons. The widely accepted value of 0.1 for μ^* was used in this study. The electron-phonon coupling constant (λ), logarithmic average phonon frequency ($\omega_{\log}$), and mean square frequency (ω_2) are key parameters in the calculation of T_c. These parameters are obtained from the Eliashberg function, which characterizes the strength of the electron-phonon interaction, and are used to predict the superconducting properties of materials based on the modified McMillan formula.

2.2.4 Computational Software Packages for Electron-Phonon Coupling

Several computational software packages have been developed to calculate the electron-phonon coupling strength and the superconducting critical temperature using first-principles

calculations, such as density functional theory (DFT). These packages require information about the electronic and vibrational properties of the material to accurately predict the electron-phonon interaction and its effect on superconductivity.

Quantum ESPRESSO: [72] Quantum ESPRESSO is an open-source software package for electronic-structure calculations and materials modeling at the nanoscale. It is based on DFT and plane-wave pseudopotentials and is widely used for the study of electron-phonon coupling. Quantum ESPRESSO includes modules for calculating phonon frequencies, electron-phonon coupling constants, and the superconducting critical temperature using the Allen-Dynes-modified McMillan formula.

VASP: [73] The Vienna Ab initio Simulation Package (VASP) is a popular software package for performing first-principles calculations based on DFT. VASP can be used to study the electronic and vibrational properties of materials, including electron-phonon coupling. It provides accurate information on the phonon dispersion relations, density of states, and other properties relevant to the electron-phonon interaction. In combination with other tools, such as the EPW (Electron-phonon Wannier) code [74], VASP can be employed to calculate the superconducting critical temperature.

ABINIT: [75] ABINIT is another open-source software package for materials modeling based on DFT. It is designed to study the electronic, vibrational, and structural properties of materials and can be used to investigate electron-phonon coupling. ABINIT offers functionalities for calculating phonon frequencies, electron-phonon coupling constants, and the Eliashberg function, which are essential for predicting the superconducting critical temperature.

Various computational software packages can be employed to calculate the electron-phonon coupling strength and the superconducting critical temperature using first-principles calculations. These tools provide essential information on the electronic and vibrational properties of materials, enabling the prediction of electron-phonon interaction and its effect on superconductivity.

2.3 Parallelism and Computational Cost

The USPEX program performs crystal structure predictions via an evolutionary algorithm. Notably, this method does not generate random structures by itself. Instead, it uses Density Functional Theory (DFT) to calculate the energies of these structures. Creating the random structures, which is facilitated by a MATLAB program, incurs almost no computational cost. However, the computation-intensive DFT calculations, particularly those involved in determining the enthalpy of the system, tend to dominate the total computational time. Therefore, any method that can speed up these DFT calculations will significantly enhance the overall efficiency of the computation.

This study was conducted on the JAIST Kagayaki server, which boasts impressive specifications: Theoretical computational performance: 1.48 PFlops
Number of nodes: 280 nodes
Number of CPUs: 560 CPUs/ 35840 Cores
Main memory capacity: 143.3TB
Interconnect: Infiniband HDR
Topology: Fat-Tree Topology

These resources are more than sufficient for the structural predictions carried out by USPEX. The key challenge lies in utilizing these resources efficiently. We know that parallel computing in DFT calculations can be significantly improved by the usage of 'mpirun', which greatly enhances computational efficiency. However, for the structure prediction tasks carried out by USPEX, this improvement is insufficient.

Because structure generation is random, certain high-symmetry structures may finish computations faster than others. Therefore, if many computational nodes are used for these tasks, resources may be wasted because computational efficiency doesn't increase linearly with an increase in computational resources. As such, a system that could adaptively allocate computational resources based on the specific requirements of each structure would significantly enhance the overall efficiency.

Moreover, the factors to be considered here extend beyond the symmetry of the struc-

tures generated by USPEX. The complexity of the pseudopotential and the computational requirements also significantly influence the computation time. The pseudopotential complexity is related to the intricacy of the atomic structure that it represents. A more complex pseudopotential often necessitates a larger basis set for an accurate solution, leading to an increase in computation time.

In addition, the computational requirements, which encompass the precision required, the number of electronic states, and other factors, are crucial in determining the time required for computation. A higher precision requirement generally leads to a longer computation time. Similarly, a system with a larger number of electronic states would require more time to achieve a solution.

Therefore, an efficient resource allocation system should also take into account the complexity of the pseudopotential and the specific computational requirements of each task. This would allow for more precise tuning of resource allocation, thus maximizing computational efficiency. It is essential to develop algorithms that can intelligently distribute computational resources based on these factors, ultimately improving the overall speed and efficiency of the USPEX program.

Going forward, it's crucial to develop new strategies and tools to manage the allocation of computational resources. This will ensure that the available nodes and cores are used optimally, thus minimizing computational costs and maximizing the speed and efficiency of the USPEX program. It would be valuable to explore automated resource allocation techniques that can adapt to the specific requirements of each task, thereby preventing resource wastage and enhancing computational efficiency. Additionally, the investigation of novel algorithms or computational techniques that can speed up DFT calculations would also greatly improve the overall performance of the USPEX program.

In addressing the differences in computational requirements caused by different pseudopotentials, we can categorize elements based on regions of the periodic table. For instance, transition metals and actinides and lanthanides demand far more computational resources than other groups of elements. A rudimentary classification of elements can aid in estimating the necessary computational resources for a given task.

Taking the structure prediction of La-Ce-H as an example, the system includes Ce, which inherently involves heavy computations. Therefore, a minimum of 32 computational cores is needed. The prediction involves the entire ternary system, which includes La-H, Ce-H, La-Ce-H, and Ce-La. Thus, optimizing computation requires enhancing the computational core count for systems containing Ce and reducing the count for the other parts.

The current system on the Kagayaki server categorizes tasks based on the number of nodes into TINY, DEFAULT, SINGLE, LONG, SMALL, LARGE, and XLARGE, with DEFAULT, SINGLE, and SMALL being the most commonly used.

Estimating a need for roughly 10,000 structure optimizations for a complex ternary system, certain potential structures can be ruled out based on algorithms or valence considerations, but the overall number change remains significant.

Without adopting an adaptive approach for structure prediction, two issues emerge: 1. Some unfavorable structures would continually occupy computational resources, and the USPEX structure prediction would need to wait for all to be completed before proceeding to the next generation. 2. For many structures, the k-points in mpirun parallel computation cannot be adequately distributed on computational resources.

Therefore, the total computation time to complete the prediction for La-Ce-H approximately takes over a week on 15 * 128 cores. By utilizing an adaptive method, certain anomalous structures can be effectively ruled out, and all available resources, including TINY, SINGLE, SMALL task classes, can be utilized. If there's a vacancy, the structure and pseudopotential can select an appropriate computational resource based on its characteristics. This approach can potentially shorten the computation time to around three days. However, due to the inherent randomness in structure prediction, precise figures cannot be provided.

Even with such adaptive computing methods, predicting systems with more than 30 atoms seems quite challenging on the Kagayaki server. The graph below illustrates the relationship between the maximum atomic number and the potential combinations. As we can see, there's a combinatorial explosion as the maximum atomic number increases.

Estimating the computational resources needed for these larger systems is near impossible. A single system would require at least around four random structures, hence to complete the prediction after optimizing 10,000 structures, the current system needs to be controlled with a maximum atoms of 24. At this point, there are only 1771 possible combinations, which should allow for the completion of computations within finite computational resources.

For the computation of larger systems, the incorporation of advanced machine learning algorithms or partial databases would be necessary to yield satisfactory results within the limited resources. These methods could facilitate more efficient predictions and help in better utilization of the available computational resources.

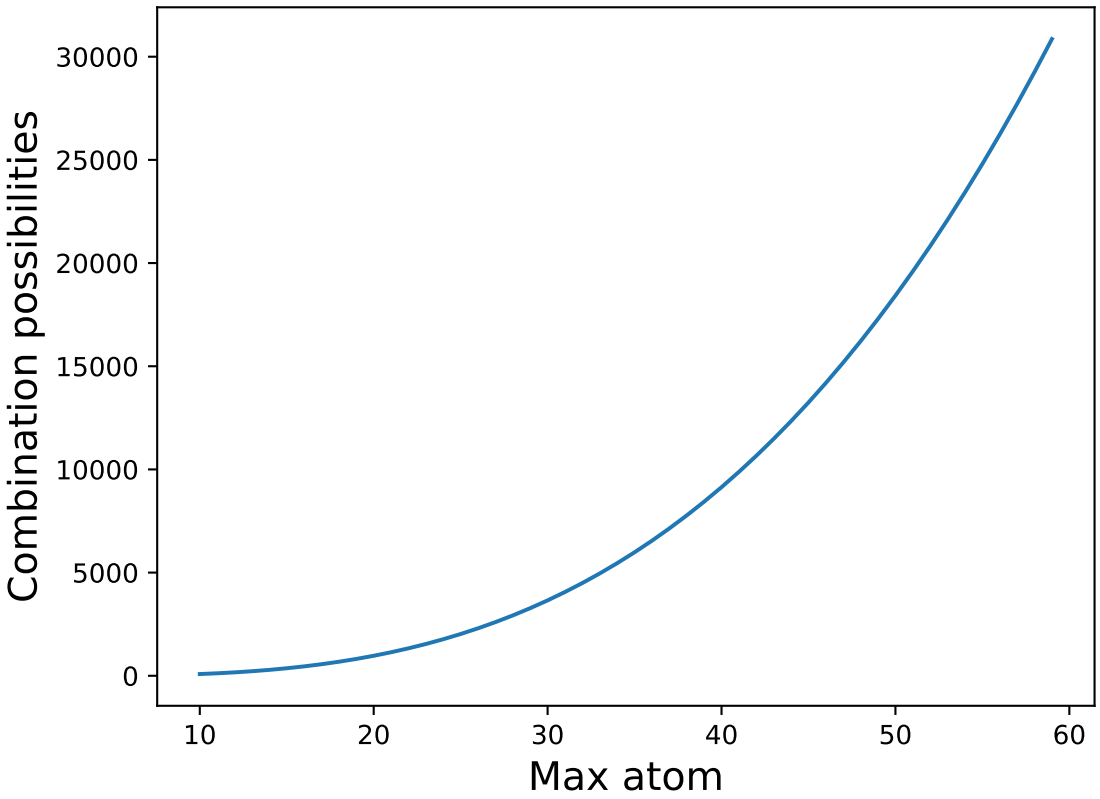

Figure 2.4: The relationships of the maximum atoms of the system and the possible of the combinations.

Chapter 3

High-T_C superconducting hydrides formed by LaH_{24} and YH_{24} cage structures as basic blocks

3.1 Motivation and Research Background

Metal hydrides have consistently been viewed as prime candidates for high-temperature (high-T_c) superconductors, attributed to their extraordinarily high phonon vibration frequency. [13, 76] Nevertheless, eliciting superconductivity in these materials, while maintaining their metallicity gradient, often necessitates extraordinarily high pressures. [2, 13, 76–79] Hence, theoretical simulations have become vital tools in the exploration of novel hydride superconductors. [36, 64, 65] Leveraging these simulations, a substantial number of predictions for binary hydrides have been concluded, including the successful prediction of YH_{10}'s room-temperature superconductivity. [4, 80] Further achievements such as the predicted room-temperature superconductivity in ternary Li_2MgH_{16} [34] and the experimentally discovered superconductivity in the C–S–H system at room temperature [81], have propelled the study of superconducting ternary hydrides to an unprecedented level.

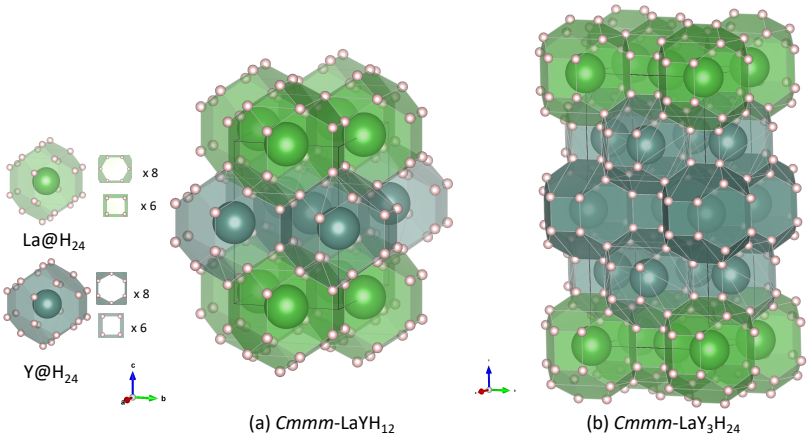

Figure 3.1: Clathrate structure of $LaYH_{12}$ (left panel, at 200 GPa) and LaY_3H_{24} (right panel, at 180 GPa) with $Cmmm$, consisting of La-centered H_{24} cages and Y-centered H_{24} cages. Each H_{24} cage is surrounded by six squares and eight hexagons. These structural models were drawn by using VESTA. [8]

Nonetheless, due to the vast diversity among ternary hydrides, the progression in identifying new high-T_c superconductors seems to be moving at a snail's pace, with only approximately 10 to 20 promising superconducting hydrides discovered thus far. [34, 81–99] Drawing from insights on binary superconductors, we know that the crystal structure profoundly impacts T_c. For instance, a handful of ultrahigh-T_c superconductors commonly present in cubic systems like $Fm\bar{3}m$-YH_{10}, $Fm\bar{3}m$-LaH_{10}, and $Im\bar{3}m$-H_3S, to name a few. [4, 17, 18] However, in the realm of ternary hydrides, the cubic structure tends to be unstable, and numerous ternary systems might undergo phase decomposition compared to their binary counterparts. Take CSH_7, for example, which is stable concerning C, S, and H, but not in comparison to binary hydrides CH_4 [100] and H_3S [18], making phase decomposition a probable occurrence. Given this decomposition, these compounds' experimental synthesis seems unlikely. Thus, ensuring their stability concerning the constituent elements and binary materials is crucial when predicting ternary hydrides.

Two significant strategies exist when seeking out ternary hydrides with the goal of obtaining high T_c: one concentrates on SH_x doped with elements like La, Se, Te, and Cl, among others, [85, 101–103] and the other revolves around La- or Y-hydrides doped with metallic elements such as $CaYH_{12}$, $CaMgH_{12}$, $KScH_{12}$, and $LaKH_{12}$. [85, 104–106] While

the latter approach has yet to yield significant improvement in T_c, the required pressure for inducing superconductivity in these materials has notably decreased, presenting the potential for experimental synthesis. In fact, the experiments involving the La–Y–H system reported high-T_c superconductivity in (La,Y)H_{10}. [107]

Building on these experiments, theoretical predictions for superconductivity in $LaYH_{12}$, La_2YH_{18}, La_4YH_{30}, and the likes have also been made. [107] These are commonly regarded as composites of $(LaH_6)_x$ + YH_6. Their predicted structures are predominantly of low symmetry, with the highest typically being $Pm\bar{3}m$ for $LaYH_{12}$. Analysis of their decomposition enthalpy indicates that these structures might undergo phase decomposition under high pressure, moving towards $R\bar{3}c$-LaH_6 + $Im\bar{3}m$-YH_6, making them less likely candidates for experimental synthesis. [4, 80] We further investigated if $LaYH_{12}$ has other structures resistant to decomposition using the USPEX fixed composition method. [36] Composition $LaYH_{12}$ was also identified in our machine learning search using a gradient boosting tree [106], showing promising T_c.

When we broadened our search to more generic forms such as $(LaH_6)_x(YH_6)_y$, we limited the scope by fixing $x = 1$ as previous studies have reported instability along the x-axis. However, along the y-axis, we discovered $Cmmm$-$LaYH_{12}$ ($y = 1$) and $Cmmm$-LaY_3H_{24} ($y = 3$), both of which exhibit a high $T_c \sim$ of 140 K. These compounds form via the stacking of LaH_{24} and YH_{24} cages, as demonstrated in Fig. 3.1. We observed a marginally higher T_c for $Cmmm$-LaY_3H_{24} compared to $LaYH_{12}$, likely due to the enhanced chemical pressure on Y through further stacking.

3.2 Computational Details

In terms of structural predictions, we employed the USPEX code [36] in conjunction with the *ab initio* kernel of the Vienna *ab initio* simulation package (VASP) [73, 108–110]. For instance, for the $LaYH_{12}$ composition, we generated 400 randomly structured entities, from single units to four-unit combinations using a $LaYH_{12}$ unit as the "base generation". We developed 100 structures for each generation with a 40% inheritance,

40% randomness, 10% soft mutation, and 10% transmutation. The evolution halted when no further advancement was observed for over ten generations, and the final structure was determined as the probable crystal structure of the composition.For the obtained candidates, we implemented *ab initio* geometrical optimizations using the Perdew–Burke–Ernzerhof (GGA–PBE) functional for the exchange-correlation functional [111].

For the most stable candidates, like $R\bar{3}c$ (100-140 GPa) and $Cmmm$ (140-300 GPa) of $LaYH_{12}$, we executed *ab initio* phonon calculations to assess their structural stabilities and T_c utilizing the Allen–Dynes formalism [72, 112, 113], which is implemented in Quantum Espresso [72]. Various computational conditions, including the cutoff energy of the plane wave basis set, the dimensions of the grid-mesh over the Brillouin zone, and others, were determined to ensure the energies were sufficiently convergent in their dependences. We utilized an $8 \times 8 \times 5$ k-mesh for the self-consistent field convergence, facilitated by the Marzari–Vanderbilt smearing scheme [114]. The final energy values were estimated via extrapolation of the smearing parameter towards zero. For the phonon calculations, mesh sizes were $16 \times 16 \times 10$ for the k- and $4 \times 4 \times 2$ for the q-mesh.

3.3 Results

The convex hull of our search for $LaH_6(YH_6)_x$ (x = 1-4) structures at 100, 200, and 300 GPa is portrayed in Fig. 5.1. $LaYH_{12}$ and LaY_3H_{24} emerge as stable phases, whereas other structures like LaY_2H_{18} and LaY_4H_{30} are prone to decomposition under these pressures.

The relative enthalpies of stable compositions $LaYH_{12}$ and LaY_3H_{24} are compared with those of candidate structures over the pressure range, as depicted in Fig. 3.3. For $LaYH_{12}$, the $Pm\bar{3}m$ structure suggested recently [107] shows a tendency to decompose into binary compounds, i.e., $YH_6(Im\bar{3}m)$ and $LaH_6(R\bar{3}c)$.

Across the entire pressure range, structures with increased stability are anticipated, transitioning from $R\bar{3}c \rightarrow Cmmm$ around $P = 140$ GPa, without a tendency towards decomposition. In the case of LaY_3H_{24}, stable formations appear as $R\bar{3} \rightarrow Cmmm$,

precluding its decomposition into $LaYH_{12}$ + 2(YH_6) or 3(YH_6) + LaH_6.

The extremely low density of states (DOS) at the Fermi level, $D(\varepsilon_F)$, is displayed by $R\bar{3}c$-$LaYH_{12}$ and $R\bar{3}$-LaY_3H_{24}, resulting in a substantially low T_c. Contrarily, $Cmmm$ compounds showcase a higher T_c with their structures depicted in Fig. 3.1. Detailed geometric descriptions of each structure are available in Table S-I in the Supplemental Information (S.I.).

As seen in Fig. 1, the structures predominantly constitute clathrate structures formed by La@H_{24} and Y@H_{24} cage units. This structure's propensity towards superconductivity seems plausible considering several other identified clathrate superconductors [4, 34, 80, 89, 115–117]. Distinct periodicities of La- and Y-layers along the c-direction correspond to $LaYH_{12}$ [(La/Y)(La/Y)$\cdots$] and LaY_3H_{24} [(La/Y/Y/Y)(La/Y/Y/Y)$\cdots$], respectively.

The evaluated phonon dispersions for the clathrate $Cmmm$ $LaYH_{12}$ are displayed in Fig. 3.4, where no imaginary modes are observed, confirming its structural stability. The phonon dispersions for other structures are provided in the S.I., confirming the absence of imaginary modes in all candidates predicted from Fig. 3.3, namely $Cmmm$-$LaYH_{12}$, $Cmmm$-LaY_3H_{24}, $R\bar{3}c$-$LaYH_{12}$, and $R\bar{3}$-LaY_3H_{24}. In contrast, the recently proposed $Pm\bar{3}m$-$LaYH_{12}$ [107] displays imaginary modes, aligning with Fig. 3.3's indications of instability.

Using the Allen–Dynes formalism [72, 112, 113], we estimated T_c, summarized in Table 6.1. For $LaYH_{12}$, T_c falls within the 130.6 $\sim$ 140.55 K range, contingent on the choice of parameter $\mu = 0.10 \sim 0.13$ for the Coulomb interaction. A slightly higher T_c for LaY_3H_{24} is attributed to the higher $D(\varepsilon_F)$ due to the condensed chemical pressure for the Y-site in the (La/Y/Y/Y) stacking structure, compared to the (La/Y)(La/Y) periodicity.

3.4 Discussion

Like the room-temperature superconductor $Fd\bar{3}m$-Li_2MgH_{16} [34], the crucial elements for high T_c are high DOS and high phonon frequency, quantifiable by λ and $\omega_{\log}$ respectively.

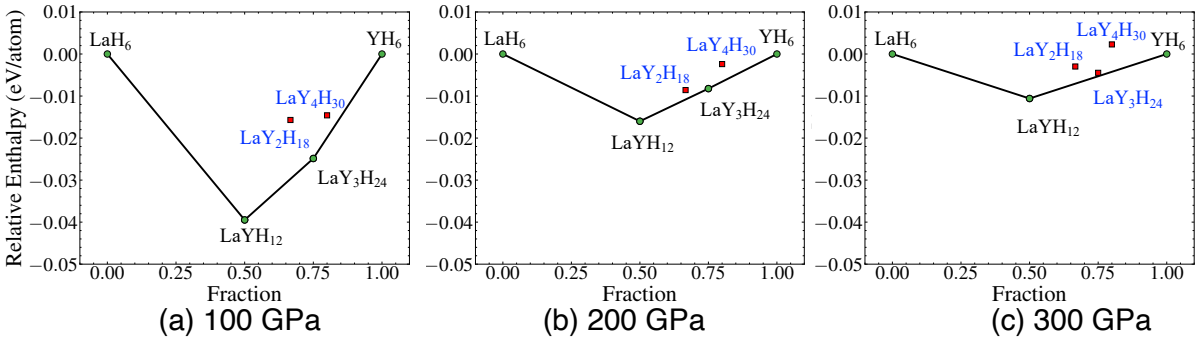

Figure 3.2: Convex hull of La–Y–H at pressures of 100 GPa, 200 GPa, and 300 GPa.

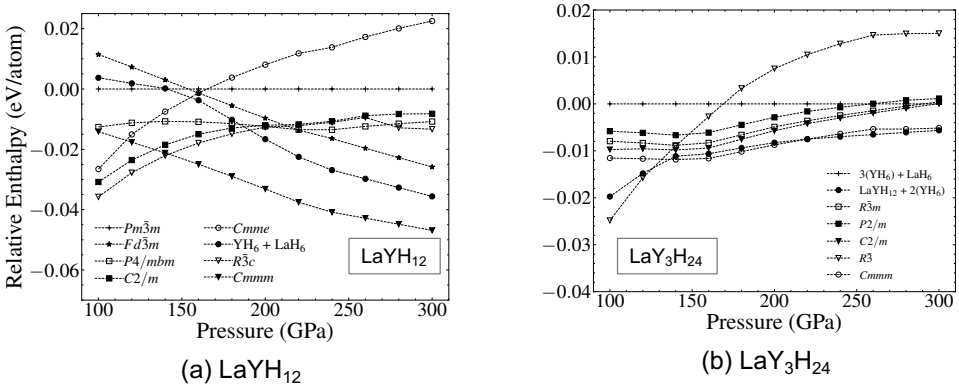

Figure 3.3: Comparisons of candidate structure enthalpies for $LaYH_{12}$ [panel (a)] and LaY_3H_{24} [panel (b)]. Such structures giving higher values than those of 'YH_6 + LaH_6' (for the left panel), '3(YH_6) + LaH_6' (for the right), and '$LaYH_{12}$ + 2(YH_6)' (for the right), are predicted to exhibit instability toward decomposition into these binary compounds.

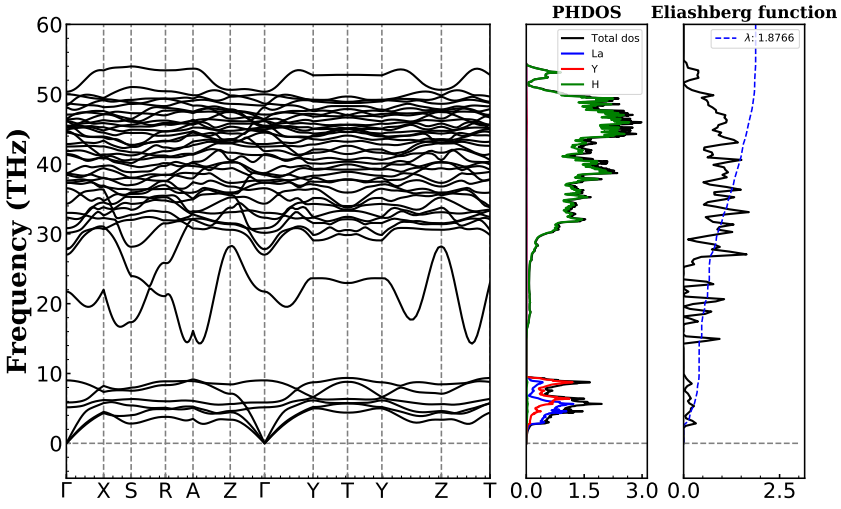

Figure 3.4: Phonon dispersions, projected phonon densities of states, and Eliashberg spectral function for *Cmmm*-$LaYH_{12}$ clathrate at 200 GPa.

Table 3.1: T_c (expressed in K) estimated using the Allen–Dynes formula through *ab initio* phonon calculations for $LaYH_{12}$ and LaY_3H_{24} at each pressure. λ and $\omega_{\log}$ (expressed in K) are the parameters appearing in the formula. The values of $D(\varepsilon_F)$ are expressed in [states/eV/atom].

	P [GPa]	λ	$\omega_{\log}$	$D(\varepsilon_F)$	T_c (μ = 0.1 - 0.13)
$LaYH_{12}$	200	1.876	1022.54	0.097	140.55 - 130.61
$LaYH_{12}$	250	1.618	1051.56	0.093	128.42 - 117.96
LaY_3H_{24}	180	2.452	891.49	0.100	145.31 - 137.11

A typical benchmark for superconductivity is $\lambda = 2$ (λ for $Fd\bar{3}m$-Li_2MgH_{16} is 3.35). [34]

The band structures and Fermi surfaces of $R\bar{3}c$-$LaYH_{12}$ and $R\bar{3}$-LaY_3H_{24} are provided in the S.I. (Figs. S-4 and S-5). These surfaces and the DOS on them are too minuscule to allow superconductivity.

Conversely, the $Cmmm$ structure has sizeable Fermi surfaces and high DOS, promoting higher λ and thus enabling superconductivity. The phonon dispersions and Eliashberg spectral functions (Figs. 3.4, S-2 and S-3) reveal that high λ values primarily result from phonon branches at higher ranges (> 10 THz), contributing to 96.2

Increasing pressures on $Cmmm$-LaY_3H_{24} (200→250 GPa) raises the phonon frequencies for branches at higher ranges, as seen in Figs. 3.4 and S-2. This is mirrored in the increased $\omega_{\log}$ (Table 6.1), contributing to a higher T_c. However, the trend vanishes when the DOS decreases (around 4.2

The marginally higher T_c for LaY_3H_{24} is due to the higher λ, as noted in Table 6.1. In this case, $\omega_{\log}$ and λ changes offset each other, causing only a minor increase in T_c. To achieve a higher T_c, more pressure would need to be applied to further increase λ, but according to our analysis, $Cmmm$-LaY_3H_{24} becomes unstable toward phase decomposition above 220 GPa.

$Pm\bar{3}m$-$LaYH_{12}$ displays a higher T_c (203 K at 180 GPa) [107], but this structure presents imaginary phonon modes as shown in Fig. 3.5, indicating structural instability. Fig. 3.3 suggests another structure, $Fd\bar{3}m$-$LaYH_{12}$, is more stable than $Pm\bar{3}m$. However, for both these structures, the imaginary modes persist, not disappearing even with the

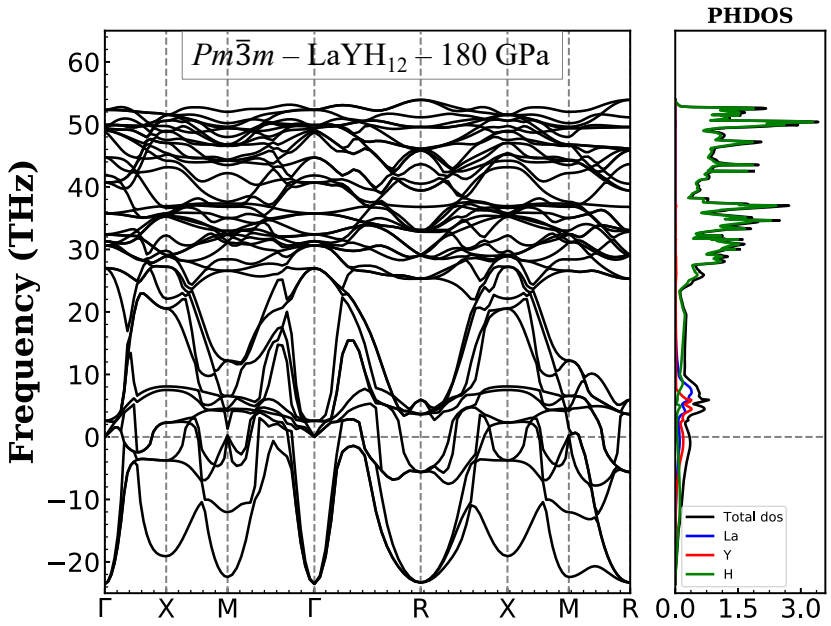

Figure 3.5: Phonon dispersions and projected phonon densities of states for $Pm\bar{3}m$-$LaYH_{12}$ at 180 GPa.

application of additional pressure.

$Pm\bar{3}m$-$LaYH_{12}$ can be considered as a derivative of the $Im\bar{3}m$-YH_6 dimer, where one Y atom is replaced by La, as illustrated in Fig. 3.6. The $Im\bar{3}m$-YH_6 formation emerges as a stable configuration in the convex-hull examination presented in Fig. 5.1. Our anticipated structure, $Cmmm$-$LaYH_{12}$, as indicated by the X-ray diffraction (XRD) peak pattern in Fig. 3.6, bears a resemblance to $Pm\bar{3}m$-$LaYH_{12}$. This suggests a close structural relationship between the two, with $Cmmm$-$LaYH_{12}$ being a slight distortion along the c-axis from $Pm\bar{3}m$-$LaYH_{12}$.

Let's take a look at some prior experimental works on Y-La-H systems [5, 22]. These studies prepared La-Y-H samples in a manner similar to YH_6 and LaH_{10}, involving laser-heating La-Y alloys with NH_3BH_3 to temperatures beyond 2,000K. Surprisingly, the La-Y-H samples demonstrated two superconducting transition phases at 183 GPa. One of these phases showed a transition temperature of 253 K at 183 GPa, which is remarkably close to the transition temperature of LaH_{10} (249 K at 151 GPa). The second phase gradually diminished with an increasing La to Y ratio (up to La_4Y).

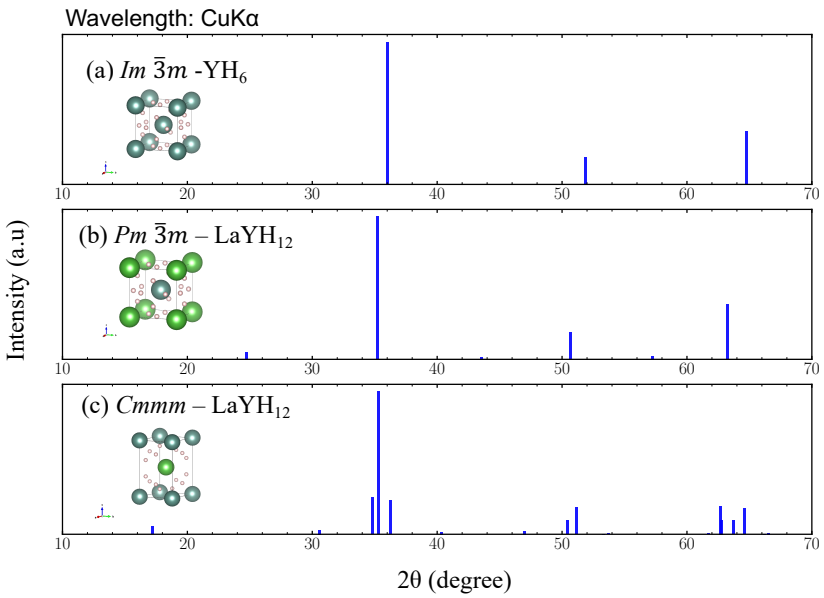

Figure 3.6: Structures and the XRD patterns of (a) $Im\bar{3}m$-YH_6, (b) $Pm\bar{3}m$-$LaYH_{12}$, and (c) $Cmmm$-$LaYH_{12}$.

Given that no binary phase in La-Y alloys remains stable under normal conditions, it seems these alloys feature phase segregation, dependent on their composition [118]. This signifies the difficulties of solely using XRD to verify the presence of La-H and/or Y-H binary components in high-pressure synthesized La-Y-H alloys or to scrutinize the stoichiometry of the La-Y mixture. More advanced characterization methods are needed for these purposes.

A promising tool is energy-dispersive X-ray spectroscopy (EDX), commonly used for elemental analysis and chemical characterization of samples [119]. However, its application to high-pressure experiments, such as those using diamond anvil cell systems, presents challenges.

3.5 Conclusions

In conclusion, our research focused on the potential crystal structures of $(LaH_6)(YH_6)_y$ compounds, which we considered as possible ternary hydrides for achieving a high T_c. We utilized a general algorithm available in USPEX for this purpose. Our study allowed

us to establish the thermal stability of these structures at $y = 1$ ($LaYH_{12}$) and $y = 3$ (LaY_3H_{24}).

We noted that a recently reported $Pm\bar{3}m$ structure exhibited instability, with a tendency towards decomposition, as illustrated by the reaction $LaYH_{12}$ ($Pm\bar{3}m$) $\rightarrow$ $LaH_6(R\bar{3}c)$ + $YH_6(Im\bar{3}m)$. However, our research led us to discover new stable structures such as $Cmmm$-$LaYH_{12}$, $R\bar{3}c$-$LaYH_{12}$, $Cmmm$-LaY_3H_{24}, and $R\bar{3}$-LaY_3H_{24}, which did not show signs of decomposition.

Of these, the $Cmmm$ clathrate structures demonstrated promise with an approximate T_c value of 130 K at around $P = 200$ GPa, based on our estimations using the Allen-Dynes formulation.

Chapter 4

The systematic study on the stability and superconductivity of Y-Mg-H compounds under high pressure

4.1 Motivation

The research into the La-Y-H ternary system provides us with rich insights into the behavior and properties of hydrogen-rich superconductors. Yet, the realm of potential high-temperature superconductors is vast, and it is critical to continue broadening our investigations to unveil new possibilities and further extend our understanding of superconductivity.

The decision to transition from the La-Y-H system to the Y-Mg-H system stems from multiple compelling reasons. One of the critical motivations lies in the promising superconducting properties of magnesium diboride (MgB_2), one of the well-known conventional superconductors that exhibits a surprisingly high Tc around 39K, the highest among all known binary intermetallic compounds. Given the already established superconducting capabilities of Mg-based compounds, the Y-Mg-H system becomes a natural candidate for exploration.

Secondly, yttrium (Y), similar to lanthanum (La), is a rare earth element with unique

electronic properties that can significantly influence superconductivity. The substitution of La by Y in the ternary system with hydrogen and magnesium offers a novel avenue to investigate how these modifications impact the superconducting properties and whether they can lead to the discovery of new high-temperature superconductors.

Finally, studying the Y-Mg-H system complements and enhances our understanding gained from the La-Y-H system. Hydrogen is a common component in both systems, and insights derived from one system could be relevant and applied to the other. Additionally, comparing the behavior of these different hydrogen-rich systems could lead to generalizable insights that could guide the search for novel superconductors in other systems as well.

In this context, our primary objectives for studying the Y-Mg-H system include discovering potential new superconductors with high Tc values, understanding the role of yttrium and magnesium in the emergence of superconductivity in this hydrogen-rich system, and drawing comparisons with the La-Y-H system to generate broader insights into high-temperature superconductivity.

As we proceed with this exploration, we are excited about the potential discoveries that the Y-Mg-H system holds, and we are committed to pushing the frontiers of knowledge in the fascinating field of superconductivity.

4.2 Research Background

In light of recent experiments confirming room temperature superconductivity in C-S-H compounds ($T_c \sim 288$K at ~ 267GPa), ternary hydrides are garnering increasing attention in the hunt for innovative high-temperature superconductors. However, the vast variety of ternary hydrides presents an escalating challenge in the exploration for novel superconducting hydrides, with only around 20 potential candidates thus far predicted. In contrast to their binary counterparts, ternary superconducting hydrides offer superior potential in achieving room temperature superconductivity. This is exemplified by the successful prediction of room temperature superconductor Li_2MgH_{16}, which has an estimated $T_c \sim 473$K at 250GPa.

Ternary hydrides, specifically those within the A-B-H system, can primarily be classified into three categories: (1) A is a metal, B is a non-metal, (2) both A and B are non-metals, and (3) both A and B are metals.

For the first category, superconductivity has been theoretically predicted in compounds like YSH_6, $MgGeH_6$, $FeSeH_6$, $CaBH_6$, $LiBH_2$, among others. Interestingly, incorporating a non-metal element can reduce the pressure needed for stability to a certain extent. For example, $LaBH_8$ is predicted to have a superconducting transition temperature (T_c) of 126 K at 50 GPa, making these compounds a promising area of exploration for potential low-pressure-stabilized high-temperature superconductors.

In the second category, predicted superconducting hydrides include H_6SSe, CSH_7, etc. These compounds lack distinct structural characteristics and exhibit phase instabilities depending on the applied pressures. For such compounds, chemical doping may offer a more viable approach. For instance, in the recently reported C-S-H compound, the highest T_c value (270 K) can be achieved by introducing approximately 0.0555 carbon into H_3S, as predicted by the virtual crystal approximation (VCA) method.

For the third category, potential superconducting compounds with T_c above 200 K primarily fall into this grouping, such as $CaYH_{12}$, $CaMgH_{12}$, Li_2MgH_{16}, etc. These compounds are energetically favorable to form clathrate structures and are likely to possess robust electronic density of states (DOS) at the Fermi level. Robust DOS structures generally exhibit a large electron-phonon coupling (EPC) constant (λ), leading to high T_c.

Our study focuses on identifying compounds with extremely high-T_c, thus we have placed greater emphasis on the third category of ternary hydrides. Given that among the binary hydrides discovered, YH_{10} has the highest T_c value (T_c = 310K at 300GPa), we initially consider the introduction of a second metal element into YH_x. Potential superconducting hydrides such as $ScYH_6$, $CaYH_{12}$, $LaYH_{12}$, and YKH_{12} have been reported, with factors such as atomic number, atomic mass, atomic radius, and number of electrons having a significant impact on the final T_c value. Lightweight elements, which usually exhibit higher vibration frequencies, could assist in achieving a higher T_c value.

The superconductivity of hydrides tends to decrease significantly as the number of d and f electrons increase, a trend most observable in metal hydrides of the actinides and lanthanides.

Given these considerations, alkali and alkaline earth metals (Li, Na, Be, Mg, etc.) — considering their atomic mass and the absence of d and f electrons — are ideal candidate elements for incorporation into YH_x. Furthermore, among the binary hydrides of these candidate elements, MgH_6 has a T_c value (271 K) closest to room temperature. Motivated by these factors, we proceeded to investigate Y-Mg-H systems for high-T_c candidates, first by exploring the crystal structures of $YMgH_x$ compounds, which are still largely unknown.

In our current study, we implemented an evolutionary-algorithm-based structural search for $YMgH_x$ compounds ($x = 2 \sim 10, 12, 14$, and 16) at 100, 200, and 300 GPa. This led to several polymorphs being obtained for each x, from which the most stable polymorphs were selected, depending on the pressures, to construct the convex hulls, thus identifying the thermodynamically stable phases. We confirmed their dynamical stabilities through phonon simulations and constructed a pressure-dependent phase diagram of the Y-Mg-H system. According to this phase diagram, we predicted T_c values for the most stable $YMgH_x$ compounds. Our findings highlight a strong interplay between phase stability and superconductivity of $YMgH_6$, with the superconductivity of $YMgH_x$ being strongly reliant on the hydrogen content and applied high pressure. Additionally, we discovered a metastable phase $Fd\bar{3}m$-$YMgH_{12}$, whose superconducting transition temperature could reach up to 190 K at 200 GPa.

4.3 Method

We initiated the exploration of $YMgH_x$ ($x = 2\sim10$, 12, 14, and 16) crystal structures at pressures of 100, 200, 300 GPa, employing the USPEX (Universal Structure Predictor: Evolutionary Xtallography) code [36]. We employed a multi-step relaxation approach for each structure, optimizing the force on each atom and the stress tensor via the VASP code [108–110, 120], following the principles of density functional theory (DFT) with the

GGA-PBE functional [111]. All DFT calculations were conducted with a cutoff energy of 60 Ry, maintaining a minimum spacing of 0.25 $^{-1}$ between the k-points in the Brillouin zone.

The initial generation consisted of 400 randomly created compositions, and each subsequent generation added 100 new structures. The structures were derived from 40% heredity, 40% random, 10% mutation, and 10% soft mutation.

Predicted polymorphs' relative formation enthalpies determined the stable phases at varied pressures, displayed in the convex hull diagram. The energy of the structures produced was globally minimized through three DFT computations, using GGA-PBE functionals [111]. For each chemical composition, approximately ten structures with the lowest energy underwent two high-precision optimizations to ensure their optimal convergence under 1 meV. The structure possessing the lowest energy was selected as the final contender.

Phonon simulations were conducted to validate the dynamic stability of the thermodynamically stable phases, ensuring they didn't exhibit imaginary modes. For the $YMgH_x$ structures with a small number of atoms, we utilized the Quantum-ESPRESSO code for phonon calculations, while the Phonopy [69] code was employed for the others. $YMgH_4$, $YMgH_7$, and $YMgH_9$ phonons were calculated using the supercell method in the Phonopy code, [69], while Quantum ESPRESSO handled the phonons of $YMgH_2$, $YMgH_3$, $YMgH_5$, $YMgH_6$, $YMgH_8$, and $YMgH_{12}$.

In order to ascertain the superconducting transition temperature (T_c) of the stable/metastable $YMgH_x$ compounds, we performed both phonon and electron-phonon coupling (EPC) calculations. The EPC was calculated using quantum ESPRESSO with a plane wave basis set, a cutoff energy of 60 Ry, and the Marzari-Vanderbilt method within the linear response theory framework. The EPC calculation matrix was evaluated using the parameters shown in Table 4.1. Therefore, the T_c values were computed using the McMillan formula [70]. All these calculations were completed with k/q-point meshes as specified in Table 4.1.

Table 4.1: Setting of k-point meshes in the self-consistent field (SCF) calculations and that of q-point meshes in the phonon calculations for stable/metastable $YMgH_x$ phases.

Compound	Space group	SCF dense k-point	Phonon q-point
$YMgH_2$	$I4_1/amd$	$12 \times 12 \times 12$	$3 \times 3 \times 3$
$YMgH_3$	$P6_3/mmc$	$16 \times 16 \times 8$	$4 \times 4 \times 2$
$YMgH_5$	$Imma$	$12 \times 12 \times 12$	$3 \times 3 \times 3$
$YMgH_5$	$Pmma$	$12 \times 12 \times 12$	$3 \times 3 \times 3$
$YMgH_6$	$Fmm2$	$12 \times 12 \times 12$	$3 \times 3 \times 3$
$YMgH_6$	$P4/mmm$	$16 \times 16 \times 12$	$4 \times 4 \times 3$
$YMgH_8$	$P4/mmm$	$16 \times 16 \times 12$	$4 \times 4 \times 3$
$YMgH_{12}$	$Cmmm$	$16 \times 16 \times 12$	$4 \times 4 \times 3$
$YMgH_{12}$	$Fd\bar{3}m$	$16 \times 16 \times 8$	$4 \times 4 \times 4$

In our subsequent analysis, we delve into the contributions of the crystal and electronic structures (specifically, the nature of chemical bonding) of stable/metastable $YMgH_x$ compounds to the T_c values. Notably, the configurations at Fermi levels are of considerable importance. Insights into these factors can be derived from the crystal orbital Hamiltonian population (COHP) and its integrated version (ICOHP). These calculations are conducted using the LOBSTER code, leveraging VASP outputs. [108–110, 120, 121]

4.4 Results and discussion

4.4.1 Pressure-dependent phase diagram

In Figure 5.3, we depict the pressure-dependent Y-Mg-H phase diagram within the 100 $\sim$ 300 GPa range. We predict seven stable $YMgH_x$ phases with different GPa ranges and structures (see Fig. S2 for the structure of each phase). Interestingly, we observe that higher pressures favor hydrogen-rich compounds. In addition to these stable phases, we investigated two metastable phases: $P4/mmm$-$YMgH_6$ and $Fd\bar{3}m$-$YMgH_{12}$.

The stability of these phases was confirmed by examining both their thermodynamic and dynamic properties.

For thermodynamic stability, we proposed numerous candidate polymorphs at each selected pressure ($P = 100, 150, 200, 250, 300$ GPa) for every x ($x = 2 \sim 10, 12, 14, 16$). Us-

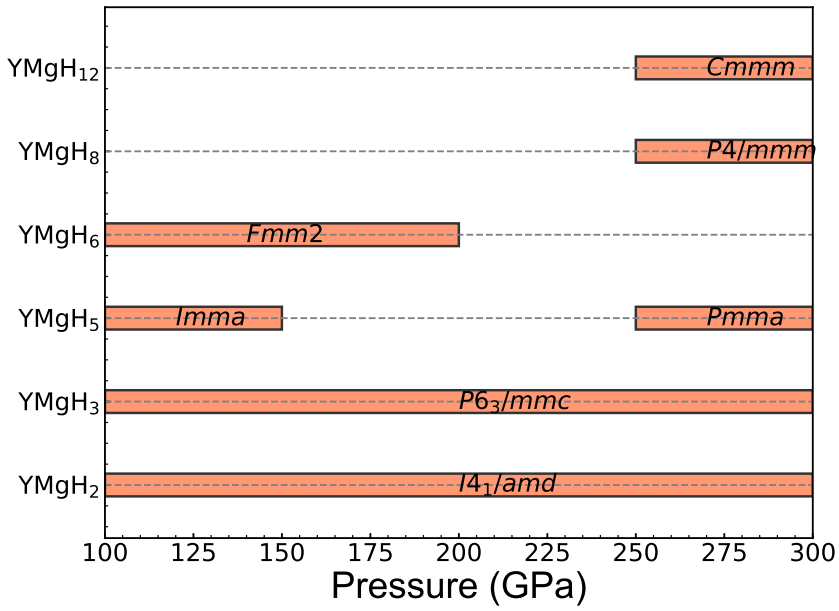

Figure 4.1: Pressure-dependent phase diagram of the Y-Mg-H system. The phases shown here are both thermodynamically and dynamically stable, while metastable phases do not appear.

ing these candidates, we drew the convex hull diagrams for each pressure using ($I4_1/amd$-$YMgH_2$ + $C2/c$-H_2 [9]) as a reference (see Figures 4.2 (a)-(e)). Our analysis indicates that $YMgH_x$ compounds for $x = 10, 14$, and 16 are thermodynamically unstable at all searched pressures. Consequently, we focused on $YMgH_x$ with $x = 2 \sim 9$ and 12, evaluating their thermodynamic stabilities against decomposition counterparts (See Supplemental Material, Figure S1).

We found that $I4_1/amd$-$YMgH_2$, $P6_3/mmc$-$YMgH_3$, and $P2/m$-$YMgH_7$ remain stable within the 100 to 300 GPa pressure range. However, $Pnm2_1$-$YMgH_4$ becomes unstable at pressures exceeding 190 GPa. $YMgH_5$ transitions from $Imma$ to $Pmma$ around 175 GPa, and $YMgH_6$ has the $Fmm2$ structure as the most stable within the $100 \sim 200$ GPa range. $P4/mmm$-$YMgH_8$ becomes thermodynamically stable above 250 GPa. $P2_1/m$-$YMgH_9$ exhibits thermodynamic stability at $100 \sim 200$ GPa. For $x = 12$, thermodynamic stability is seen over 200 GPa, but decomposition occurs at less than 250 GPa.

In terms of dynamic stability, we evaluated whether the thermodynamically stable phases for $x = 2 \sim 9$ and 12 were also dynamically stable at each pressure. From these

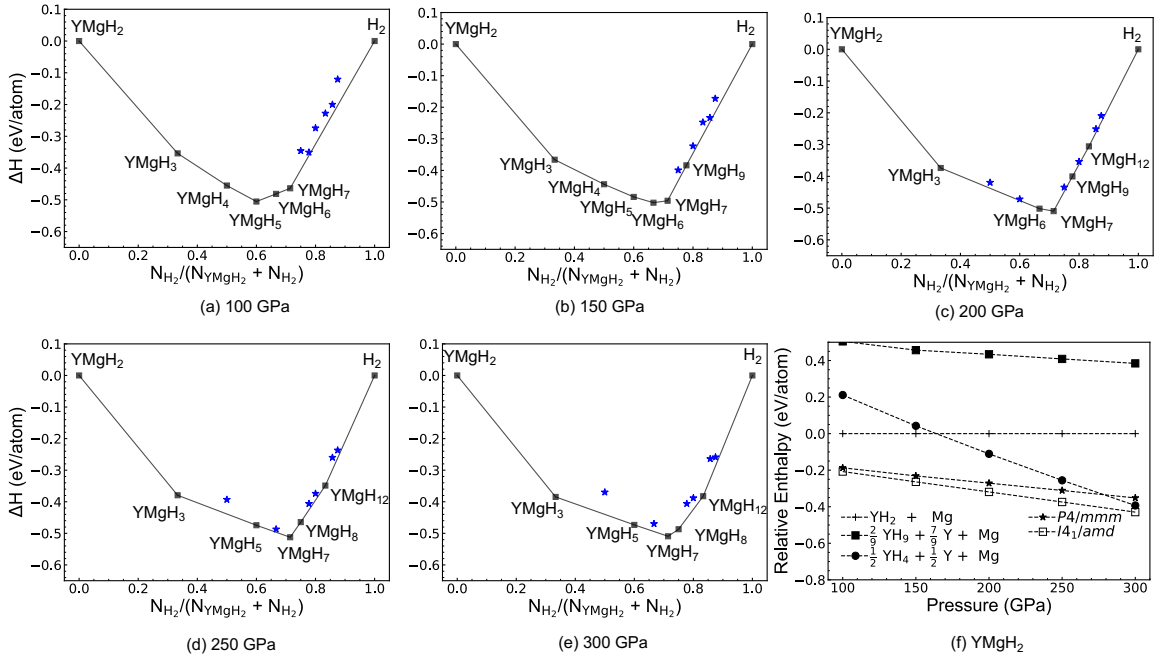

Figure 4.2: Convex hull diagrams of $YMgH_x$ relative to $YMgH_2$ and H-$C2/c$ [9] at the pressure of (a) 100 GPa, (b) 150 GPa, (c) 200GPa, (d) 250 GPa, and (e) 300 GPa. To ensure the relative stabilities of $YMgH_x$ compounds, the relative stability of $YMgH_2$ against several decomposition possibilities is also given in (f).

results, we plotted the pressure-dependent phase diagram (Figure 5.3). Our findings show that $Pnm2_1$-$YMgH_4$, $P2/m$-$YMgH_7$, and $P2_1m$-$YMgH_9$ are dynamically unstable in the pressure range where they are considered thermodynamically stable. $YMgH_5$ shows dynamical instabilities between 150 and 250. After excluding these dynamically unstable phases, we identified the seven stable phases (Figure 5.3) and two additional metastable phases.

In conclusion, our study has predicted unique crystal structures for several $YMgH_x$ compounds. We have identified highly symmetric clathrate structures in both stable phases ($P4/mmm$-$YMgH_8$ and $Cmmm$-$YMgH_{12}$), and metastable phases ($P4/mmm$-$YMgH_6$ and $Fd\bar{3}m$-$YMgH_{12}$), as depicted in Figure 4.3.

Among these, the hydrogen-rich $Cmmm$-$YMgH_{12}$ and $Fd\bar{3}m$-$YMgH_{12}$ compounds are characterized by H_{24} cages with six quadrilaterals and eight hexagons, respectively. Meanwhile, $P4/mmm$-$YMgH_6$ and $P4/mmm$-$YMgH_8$ exhibit H_{14} and H_{18} cages, respectively.

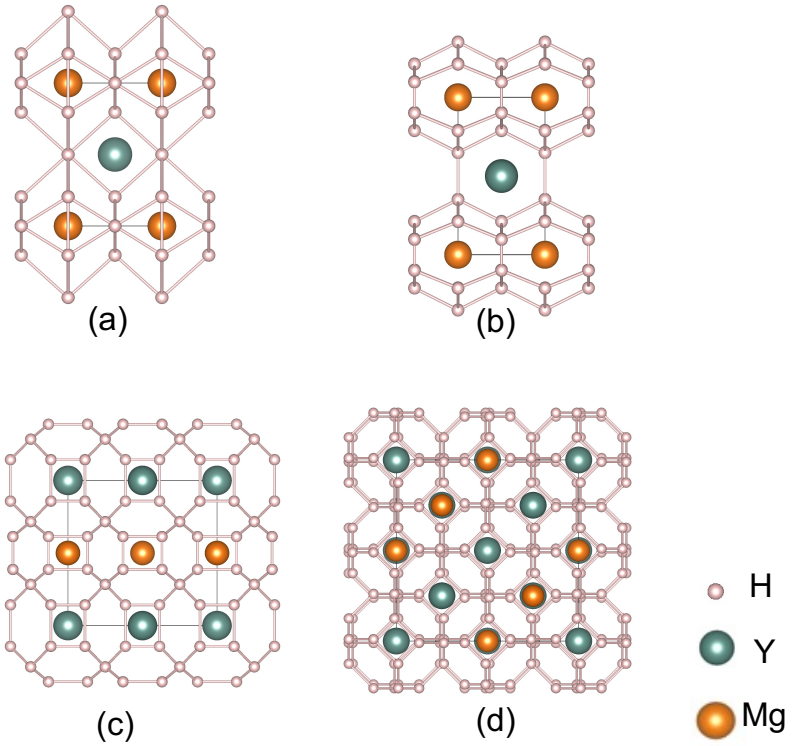

Figure 4.3: The clathrate structure of (a) $P4/mmm$-$YMgH_6$, (b) $P4/mmm$-$YMgH_8$, (c) $Cmmm$-$YMgH_{12}$, (d) $Fd\bar{3}m$-$YMgH_{12}$.

Remarkably, they share the same space group as $ScCaH_8$, a compound with a clathrate structure that shows a T_c of 212 K at 200 GPa.

Based on these findings, it's reasonable to anticipate that clathrate structures could prove promising in the search for high-T_c compounds.

4.4.2 Superconducting transition temperatures

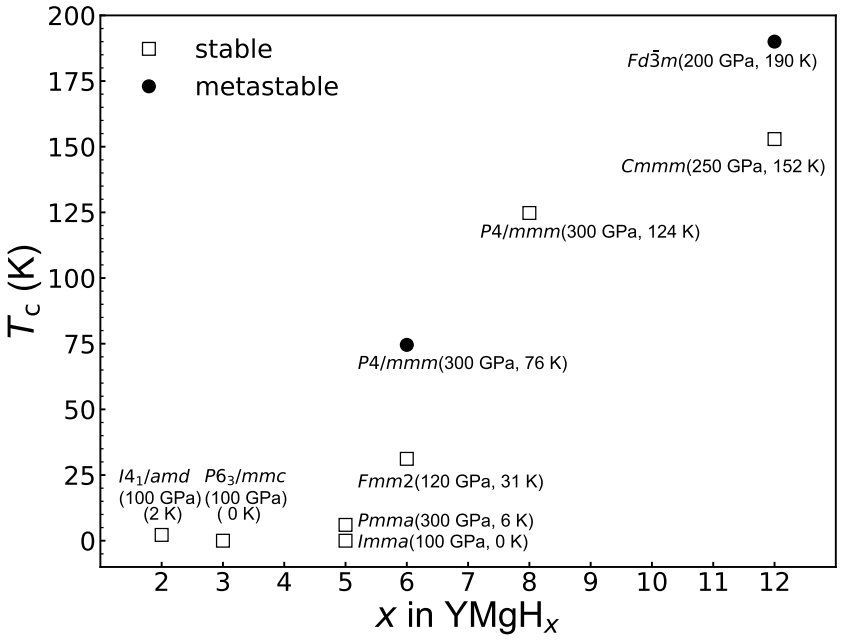

Figure 4.4: Predicted superconducting transition temperatures (T_c) of the stable and metastable phases at certain pressures ($\mu^* = 0.1$).

In our pursuit to identify superconducting $YMgH_x$ compounds for $x = 2, 3, 5, 6, 8$, and 12, we've forecasted T_c values under specific pressures applying the McMillan formula [70] (equation **??**). Within this formula, μ^* is a measure of effective Coulomb repulsion, typically ranging between 0.10 and 0.13; λ represents the electron-phonon coupling constant, and ω_{log} denotes the logarithmic average phonon frequency.

The Eliashberg spectral functions $\alpha^2F(\omega)$ provide us with λ and ω_{log} values, as shown in Figure 4.5. Another important factor influencing $\alpha^2F(\omega)$ is the electronic density of states at the Fermi level, $N(E_F)$, presented in Figure 4.6. We've evaluated these factors for stable/metastable $YMgH_x$ phases, as listed in Table 6.1. The anticipated T_c values

Table 4.2: Calculated electron-phonon coupling parameters (λ), the logarithmic average phonon frequency $\omega_{\log}$ (K), electronic density of states at the Fermi level $N(E_F)$ (in states/eV/^{3}), and superconducting critical temperatures T_c (K) with $\mu^* = 0.10$ and 0.13 for stabel/metastable $YMgH_x$ compounds at selected pressures.

Compound	Space group	P [GPa]	λ	$\omega_{\log}$ [K]	$N(E_F)$ [states/eV/ ^{3}]	T_c [K]
$YMgH_2$	$I4_1/amd$	100	0.41	451	0.029	2 – 1
$YMgH_3$	$P6_3/mmc$	100	0.17	470	0.020	$\ll 0.001$
$YMgH_5$	$Imma$	100	0.13	761	0.005	$\ll 0.001$
$YMgH_5$	$Pmma$	200	0.42	1037	0.012	6 – 3
		300	0.39	1219	0.014	4 – 2
$YMgH_6$	$Fmm2$	120	0.73	800	0.009	31 – 24
$YMgH_6$	$P4/mmm$	300	1.07	963	0.021	75 – 65
$YMgH_8$	$P4/mmm$	300	1.63	1013	0.025	125 – 115
$YMgH_{12}$	$Cmmm$	250	1.66	1224	0.021	153 – 141
		300	1.31	1449	0.021	143 – 129
$YMgH_{12}$	$Fd\bar{3}m$	200	2.18	1250	0.025	190 – 178
		300	1.81	1409	0.027	189 – 175

for $YMgH_x$ are summarized in Fig. 4.4 and Table 6.1.

Fig. 4.4 clearly demonstrates that the expected T_c values generally increase with the augmentation of the hydrogen content x. The clathrate-structured $P4/mmm$-$YMgH_6$, presented in Fig. 4.3, displays a T_c of 76 K, akin to the boiling point of liquid nitrogen (77 K). Notably, $P4/mmm$-$YMgH_8$, $Cmmm$-$YMgH_{12}$, and $Fd\bar{3}m$-$YMgH_{12}$, also adopting clathrate structures, exhibit higher T_c values of 124, 152, and 190 K, respectively. Hence, these hydrogen-rich phases are deemed as high-T_c materials.

With a critical hydrogen content of $x = 6$, clathrate structures emerge as vital keys to discovering high-T_c materials. We'll offer a detailed analysis of these structures in the following subsection. However, hydrogen-poor materials ($x \leq 5$) either show no superconductivity or significantly lower T_c values. For instance, $P6_3/mmc$-$YMgH_3$ and $Imma$-$YMgH_5$ lack superconductivity, while $I4_1/amd$-$YMgH_2$ does exhibit superconductivity, but with a mere T_c of 2 K.

In the case of $YMgH_5$, the $Pmma$ phase becomes stable by increasing pressure (above 250 GPa) and accordingly, the associated T_c value also slightly increases (approximately 6 K).

Shifting focus to the correlation between T_c and its constituent quantities (as per equation **??**), we notice that the higher-T_c in hydrogen-rich compounds ($x \geq 6$) generally arises from greater EPC constants (higher-λ). For these compounds, ω_{log} increases in line with the H content x. Yet, the same does not hold true for hydrogen-poor compounds. Take $YMgH_3$ and $YMgH_2$ as examples: despite $YMgH_3$ having a higher ω_{log} than $YMgH_2$, the former shows no superconductivity, while the latter does.

Regarding $N(E_F)$, it's challenging to directly interpret its influence on T_c. However, we observe that $N(E_F)$ values for hydrogen-rich compounds typically range from 0.021 to 0.027. On the contrary, hydrogen-poor compounds exhibit a greater variation in $N(E_F)$ values (from 0.005 to 0.029), depending on the specific system.

In order to better understand the contribution of ω_{log}, $N(E_F)$, and λ to T_c, we will further examine their phonon and electronic band structures. These are displayed in Figures 4.5 and 4.6 respectively.

The phonon partial density of states as illustrated in Fig. 4.5 gives us insight into the atomic influence on the phonon modes: Vibrations from H atoms largely contribute to high-frequency phonon modes (approximately above 25 THz), while Mg and Y atoms account for the lower frequency phonon modes (approximately below 25 THz). The Eliashberg spectral functions' distributions and peak locations bear a resemblance to those of phonon band structures, suggesting the correlation between the Eliashberg spectrum and low/high-frequency-phonon modes, brought about by Y or Mg/H atomic vibrations interacting with electrons near E_F. In the case of H-rich $YMgH_x$ compounds (where $x = 8$ and 12), their Eliashbarg functions show a marked increase at higher frequencies. This hints at a greater role played by hydrogen vibrations in the electron-phonon coupling (EPC) for H-rich substances.

As for Fig. 4.6, it presents band structures and corresponding density of states for certain $YMgH_x$ compounds, highlighting the atomic roles in the electronic states around E_F. For $YMgH_3$ (a) and $YMgH_5$ (b), Y atoms are the main contributors to the electronic states near E_F, despite the negligible $N(E_F)$ value of the latter. This means that even

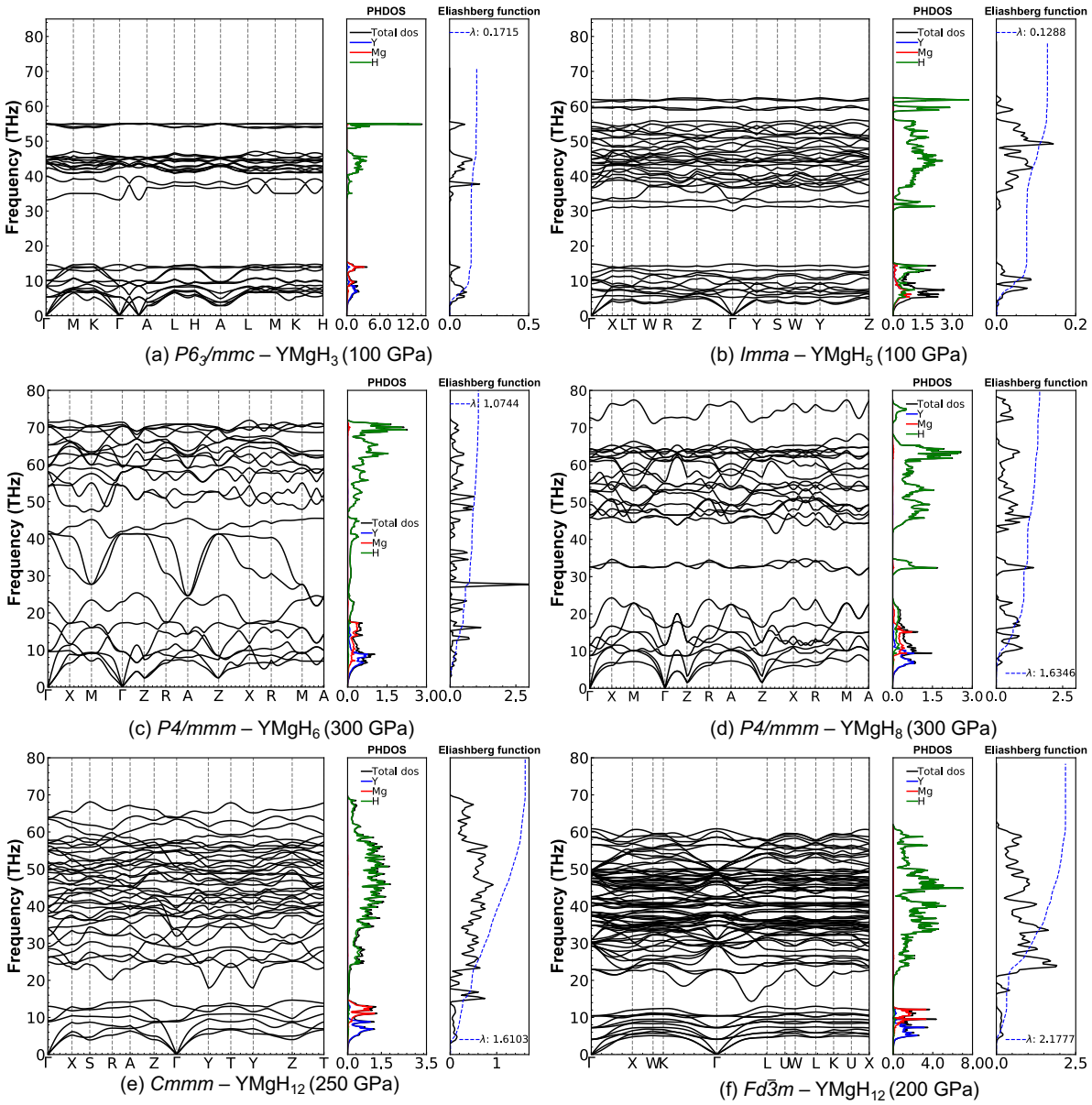

Figure 4.5: Phonon band structures and Eliashberg spectral functions for (a) $P6_3/mmc$-$YMgH_3$, (b) $Imma$-$YMgH_5$, (c) $P4/mmm$-$YMgH_6$, (d)$P4/mmm$-$YMgH_8$, (e) $Cmmm$-$YMgH_{12}$, and (f) $Fd\bar{3}m$-$YMgH_{12}$.

under a high pressure of 100 GPa, the $Imma$-$YMgH_5$ phase is not sufficiently metalized. However, in the case of H-rich compounds (from d to f), a blend of H and Y atomic orbitals form the electronic states near E_F, with the contribution of H slightly exceeding that of Y. Keeping in mind that T_c ascends as H content rises, it is clear that the input from H atoms to $N(E_F)$ is crucial to reach high T_c. This will be further elucidated through structural and chemical bonding analyses.

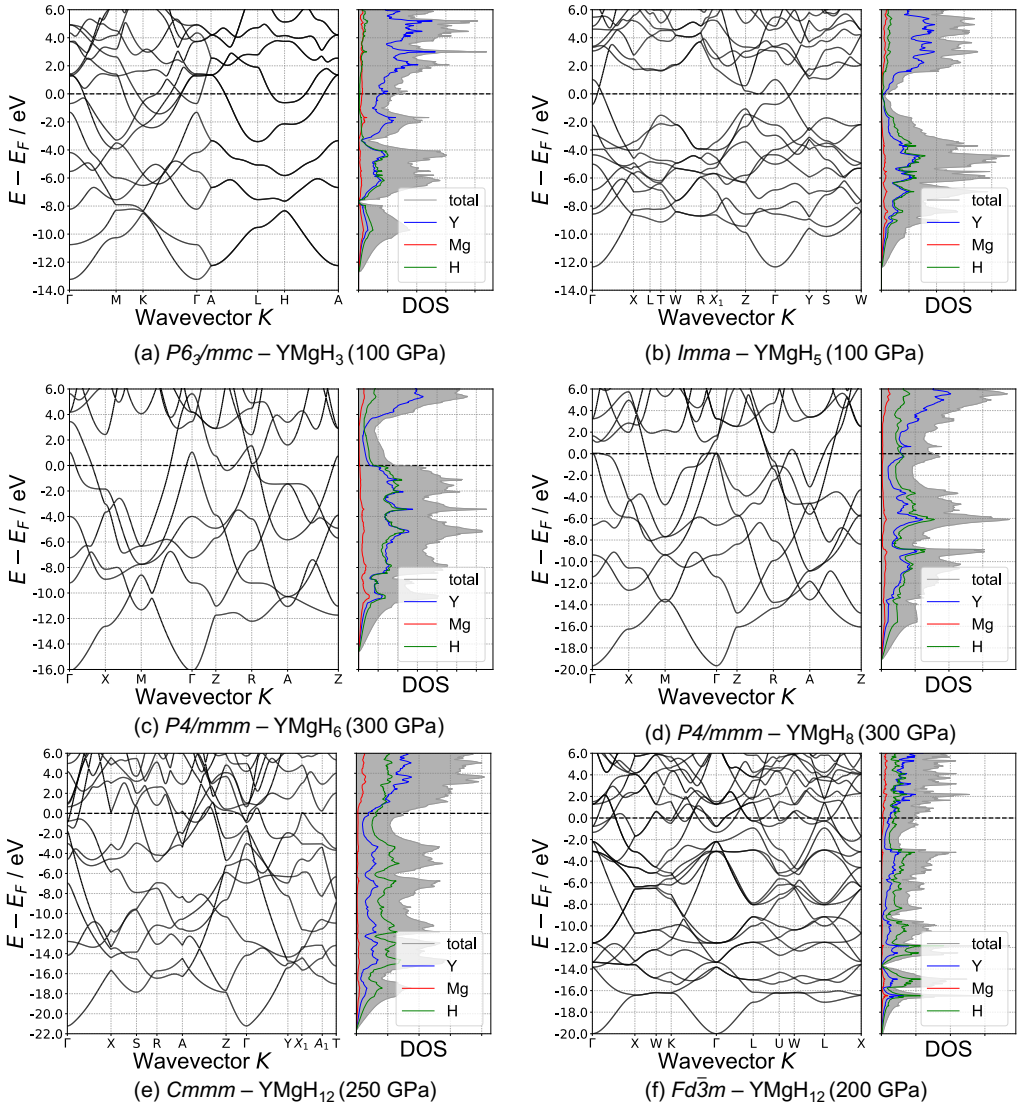

Figure 4.6: Electronic band structures for (a) $P6_3/mmc$-$YMgH_3$, (b) $Imma$-$YMgH_5$, (c) $P4/mmm$-$YMgH_6$, (d)$P4/mmm$-$YMgH_8$, (e) $Cmmm$-$YMgH_{12}$, and (f) $Fd\bar{3}m$-$YMgH_{12}$.

4.4.3 Structural and chemical bonding analyses

We will now proceed to illustrate the relationships between the structures and the electronic states/chemical bonding for H-rich $YMgH_x$ compounds. As shown earlier, the coexistence of different hydrogenic motifs in hydrogen lattices (such as H^-, H_2^- dimer, square H_4^{2-}, etc.) is recognized as a significant trigger of high-T_c for other metal hydrides [64]. Given this, we can broadly categorize the nature of chemical bonding into two types: one where hydrogen atoms weakly bond with other hydrogen or metal atoms, and another featuring H_{2n}-like covalent bonding. We'll subsequently delve into a more detailed analysis of the dimerized hydrogens.

Table 6.1 enumerates the first nearest neighbor distances between atomic pairs, namely Y–H, Mg–H, and H–H lengths (see Fig. S2 for the radial distribution functions of H–H atomic pairs). Notably, for H-rich materials exhibiting high-T_c, the H–H length consistently proves shorter than Mg–H and Y–H lengths. Generally, this shorter H–H length suggests the potential for forming a stronger chemical bond between the H–H atomic pair. Our focus is on high-T_c compounds, but for the sake of comparison, we also consider the case of H-poor materials where the H–H lengths are longer than the Mg–H lengths, though no obvious trend can be observed between the H–H and Y–H lengths. When comparing H-rich and H-poor materials, the former exhibits significantly shorter H–H lengths than the latter, while no distinct trend emerges for Y–H and Mg–H lengths. We will explore individual hydrogenic motifs in the H-rich materials in the following section.

Figure 4.7 displays the electron localization function (ELF) of $YMgH_x$ compounds ($x = 6, 8$, and 12), with arrows indicating the first nearest neighbor H–H distances. For $P4/mmm$-$YMgH_8$, the H–H distance of 0.86 Åapproximates the bond length of the H_2 molecule (0.74 Å), likely due to charge transfer from Y and/or Mg atoms to the H–H pair. This transfer populates the antibonding state of the H_2 molecule, leading to a longer H–H distance, as shown in Figure 4.7 (b).

The $Cmmm$-$YMgH_{12}$ compound features an even longer H–H distance of 1.04 Å, exceeding both the H_2 bond length and the H–H distance in $P4/mmm$-$YMgH_8$. The H–

Table 4.3: Distances of the first nearest neighboring atomic pairs, Y–H, Mg–H, and H–H for stable/metastable $YMgH_x$ compounds at selected pressures. The units are given in Å.

Compound	Space group	P [GPa]	Distance [Å] Y–H	Mg–H	H–H
$YMgH_2$	$I4_1/amd$	100	1.93	1.92	2.68
$YMgH_3$	$P6_3/mmc$	100	2.03	1.70	1.97
$YMgH_5$	$Imma$	100	1.94	1.65	1.78
$YMgH_5$	$Pmma$	300	1.73	1.56	1.52
$YMgH_6$	$Fmm2$	120	1.90	1.68	1.73
$YMgH_6$	$P4/mmm$	300	1.76	1.54	1.54
$YMgH_8$	$P4/mmm$	300	1.82	1.58	0.86
$YMgH_{12}$	$Cmmm$	250	1.88	1.73	1.04
$YMgH_{12}$	$Fd\bar{3}m$	200	1.97	1.83	1.10

H distances in $YMgH_{12}$ approximate those in YH_6 (1.19 Å) and MgH_6 (1.10 Å) [122, 123], likely due to the clathrate structure formed in $Cmmm$-$YMgH_{12}$ [Figure 4.7 (c)], which mirrors those in MgH_6 and YH_6, all composed of H_{24} cages.

$Fd\bar{3}m$-$YMgH_{12}$, featuring the shortest bond length of 1.10 Å[Figure 4.7 (d)], contains slightly distorted square H_4 units, similar to a solid-state-like CaH_6 structure [64]. On the other hand, the H–H distance in $P4/mmm$-$YMgH_6$ (1.54 Å) [Figure 4.7 (a)] notably exceeds the H_2 bond length.

To summarize, the H–H distances in $P4/mmm$-$YMgH_8$, $Cmmm$-$YMgH_{12}$, and $Fd\bar{3}m$-$YMgH_{12}$ all surpass the H_2 molecule's bond length, with the first two likely owing to the metals' charge transfer to the forming anion (H_2^-). As seen in Figures 4.7 (a)-(c), the quantity of H_2^- units seems to grow with increasing x.

Diverging from these motifs, slightly distorted square H_4^{2-} units emerge in $Fd\bar{3}m$-$YMgH_{12}$ [Figure 4.7 (d)], exhibiting the highest-T_c value among the Y-Mg-H compounds explored in this study. These (slightly distorted) square H_4 units possess nearly degenerate orbitals that are partially occupied, enabling them to accommodate two more electrons and consequently forming H_4^{2-}.

Beyond the prior qualitative elucidation, we can validate the occupation of bonding/antibonding orbitals via the (orbital-decomposed) partial density of states (pDOS) and the projected crystal orbital Hamilton population (pCOHP), as presented in Fig. 4.8.

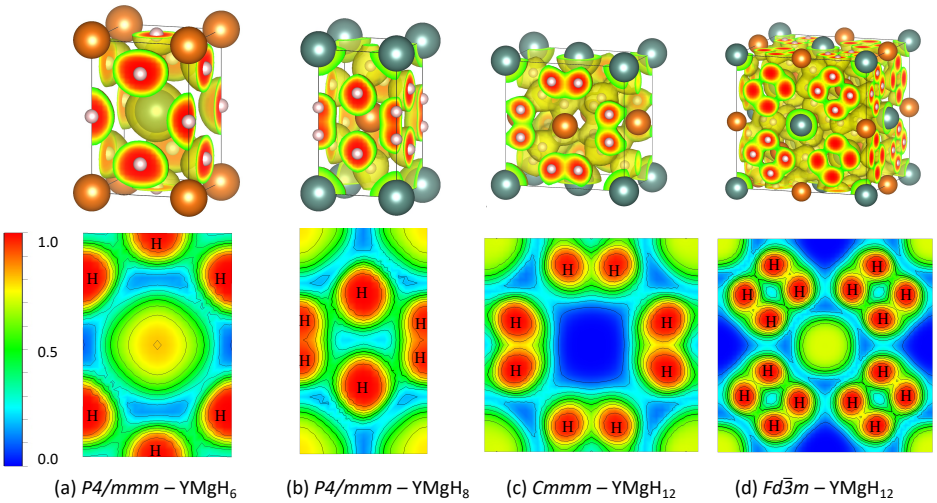

Figure 4.7: The contour plots of electron localization function (ELF) on (a) (200) plane of $P4/mmm$-$YMgH_6$, (b) (100) plane of $P4/mmm$-$YMgH_8$, (c) (100) plane of $Cmmm$-$YMgH_8$, and (d) (100) plane of $Fd\bar{3}m$-$YMgH_{12}$ with an isosurface value of 0.5.

Remember that positive/negative pCOHP values denote bonding/antibonding characteristics. Within the H-rich materials, we initially identify electronic states near the Fermi level composed of H-1s and Y-4d orbitals, by examining the pDOS. Upon inspecting the pCOHP, we find negative values around E_F for H–H bonding, correlating with the shortest H–H distance. We will analyze individual high-T_c compounds shortly.

The integration of the H-1s orbital and the Y-4d orbitals in $P4/mmm$-$YMgH_8$ (Fig. 4.8 (b)) is more pronounced compared to $P4/mmm$-$YMgH_6$ (Fig. 4.8 (a)); H–Y bonding states span an energy range from E_F to -15 eV. Simultaneously, the hybridization between the H–H pair in $P4/mmm$-$YMgH_8$ also intensifies compared to $P4/mmm$-$YMgH_6$; these related states deepen and center around -15 eV. The H–H antibonding states in $P4/mmm$-$YMgH_8$ emerge around E_F. In $Cmmm$-$YMgH_{12}$ and $Fd\bar{3}m$-$YMgH_{12}$, the H–H antibonding states surface just below E_F (see Figs. 4.8 (c) and (d)). As a result, H–H atomic pairs form covalent bonds. This observation aligns with the ELF depicted in Fig. 4.7 (c) and (d).

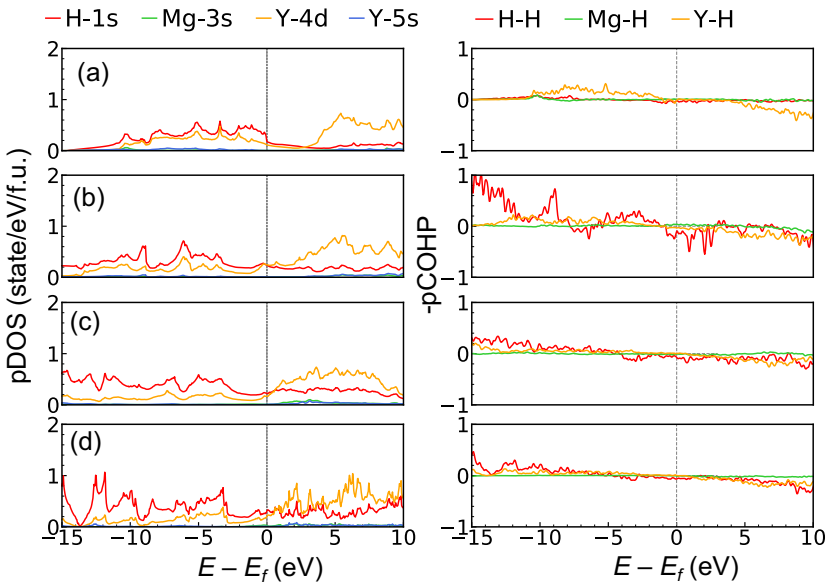

Figure 4.8: Partial (electronic) density of states (pDOS) and projected crystal orbital Hamilton population (pCOHP) for (a) $P4/mmm$-$YMgH_6$, (b) $P4/mmm$-$YMgH_8$, (c) $Cmmm$-$YMgH_{12}$, and (d) $Fd\bar{3}m$-$YMgH_{12}$.

4.5 Conclusion

We've undertaken a comprehensive exploration of the stability and superconductivity of the ternary hydride $YMgH_x$ under high pressures. Seven phases were discerned as the most stable and two as metastable, considering both thermodynamic and dynamic stabilities. Our study indicates that $YMgH_x$, for $x = 6, 8$, and 12 under high pressure, adopts clathrate structures composed of H_{14}, H_{18}, and H_{24} cages, respectively.

Our calculations of T_c using the McMillan formula in conjunction with electron-phonon coupling simulations point to high-T_c superconductivity across all the $YMgH_x$ clathrate structures. Interestingly, the T_c value ascends as the H content x grows. The stable $Cmmm$-$YMgH_{12}$ and metastable $Fd\bar{3}m$-$YMgH_{12}$ sodalite structures present T_c values of 153 K at 250 GPa and 190 K at 200 GPa, respectively.

The analysis of electronic and phonon band structures reveals that the contributions from hydrogen to electronic states near the Fermi level, alongside a dense phonon density of states at high frequencies, are critical to invoking high-T_c. Further dissection of structural and chemical bonding offers valuable understanding of high-T_c origin within

the Y-Mg-H system: In the cage structures, there is a coexistence of H atoms with weak bonds to other atoms, as well as square H_4 units manifesting weaker covalent bonding with extended bond lengths compared to the H_2 molecule, akin to CaH_6.

Chapter 5

High-Pressure Mg-Sc-H Phase Diagram and Its Superconductivity from First-Principles Calculations

5.1 Motivation

In the domain of high-pressure superconductivity, the investigations into La-Y-H and Y-Mg-H ternary hydrides have unveiled rich structural complexities and superconducting behaviors. From stable clathrate structures in $(LaH_6)x(YH_6)y$ compounds to the strong correlation of hydrogen content with superconducting properties in Y-Mg-H system, these explorations have opened new frontiers in our understanding of high-temperature superconductivity in ternary hydrides.

While these breakthroughs have advanced our knowledge, the pursuit for further understanding motivates us to explore a new ternary hydride system: Mg-Sc-H under high-pressure conditions. Our interest in this system stems from several reasons:

First, Scandium (Sc) presents a compelling case for investigation due to its outer electronic configuration resembling that of yttrium (Y), an element already proven to have fascinating interactions with hydrogen and magnesium in the Y-Mg-H system. This similarity in electronic structure leads us to hypothesize that Sc may exhibit comparable

or even more interesting behaviors when paired with magnesium and hysdrogen under high-pressure conditions.

Second, the nature of the bonding and structural arrangements that Mg and Sc might form with hydrogen could shed light on the fundamental understanding of how different elements interact with hydrogen under extreme conditions, further contributing to the development of a more comprehensive and predictive model of superconducting hydrides.

Thus, our objective in this investigation is to delineate the phase diagram of the high-pressure Mg-Sc-H system, identify potential superconducting phases, and estimate their Tc using first-principles calculations. Through this, we aim to uncover the behaviors of Sc in the presence of Mg and H, its potential superconducting characteristics, and contribute to the broader understanding of high-temperature superconductivity in hydride materials.

5.2 Research Background

Hydrides abundant in hydrogen, particularly those of rare earth and alkaline earth metals, have emerged as promising candidates for realizing room-temperature superconductivity under high pressure. These hydrides often stabilize in clathrate structures comprising H atoms, which substantially reduce the pressure-volume (PV) enthalpy term, thereby enabling stability at lower pressures. In these configurations, H atoms notably contribute to both the electronic density of states around the Fermi level and the phonon density of states, thus holding potential for high-temperature superconductivity. For instance, recent theoretical work suggests the potential for room-temperature superconductivity in YH_{10} with an H_{32} cage structure.

For binary hydrides of alkaline earth and rare earth elements, most of the systematic investigation into their crystal structures and superconductivity has been theoretically driven, apart from a few magnetic rare earth hydrides. There's been significant interest in experimentally validating binary hydrides predicted to exhibit high-temperature superconductivity. Prior theoretical simulations suggest that the T_c values of ScH_6, ScH_7, ScH_9, ScH_{10}, ScH_{12}, and MgH_6 could range between 120 and 270 K above 250 GPa. However,

with an increase in H content, the predicted T_c of ScH_{14}, MgH_{12}, MgH_{16}, and MgH_{22} decreases significantly, with hydrogen predominantly appearing in a molecular form. These findings suggest that the hydrogen content and the corresponding structures formed by hydrogen atoms are key determinants of T_c values. Superconducting clathrate structures such as LaH_{10}, CaH_6, YH_6, BaH_{12}, and CeH_9 have been experimentally verified. The consistency between theoretical prediction and experimental findings in the superconductivity of these binary hydrides has spurred broader explorations of metal hydrides, including ternary systems.

Recent experimental investigations into the ternary La-Y-H system have reported that the synthesized $(La,Y)H_{10}$ at 180 GPa displays a T_c of 253 K. Notably, the pressure necessary for $(La,Y)H_{10}$ to achieve superconductivity is lower than that required for LaH_{10}, suggesting greater potential in ternary hydrides for achieving room-temperature superconductivity at lower pressures.

Ternary metal hydrides such as La-Y-H, Ca-Y-H, Sc-Ca-H, Sc-Y-H, Y-Mg-H, and Ca-Mg-H have been recently examined for stability and superconductivity predictions through theoretical calculations. Predominantly, the high-T_c superconducting compounds in these systems favor cage-like formations. For instance, $Fd\bar{3}m$-$CaYH_{12}$, with a cubic structure, retains a clathrate structure of H_{24} cages akin to CaH_6 and YH_6. Furthermore, $Fd\bar{3}m$-$CaYH_{12}$ exhibits stability above 170 GPa with a T_c of 254 K. Theoretical insights suggest that the pronounced electron-phonon coupling (EPC) in the clathrate structures of these ternary metal hydrides relates to the phonon mode of the H-H bond in the cage. Additionally, these materials share several characteristics, such as atomic radius, electron number (spd valence electrons), electron negativity, atomic mass of constituent elements, among others. Such similarities might prevent the H cage from collapsing, maintaining the cage structure and superconductivity in the ternary hydride with clathrate structure. In the Sc-Ca-H system, $ScCaH_8$ and $ScCaH_{12}$ are potential high-T_c superconductors, with their T_c values approximating 212 K and 182 K at 200 GPa, respectively.

In this context, we focus our study on the Mg-Sc-H system, seeking to decipher the phase diagram and superconductivity of the associated ternary compounds under high

pressure. Utilizing the evolutionary algorithm for crystal structure prediction, we have identified the stable structures of $MgScH_6$, Mg_2ScH_{10}, $MgSc_2H_9$, and $Mg(ScH_4)_3$ under high pressure. These are projected to have the highest hydrogen content in the ternary Mg-Sc-H compounds. No stable compounds with higher hydrogen content were found in the hydrogen-rich cases of the Mg-Sc-H system within the studied pressure range (100-200 GPa), unlike in other ternary systems such as La-Y-H and Ca-Y-H. Some of the stable structures of ternary Mg-Sc-H compounds are expected to exhibit superconductivity; however, their superconducting transition temperatures peak only at 41 K at 100 GPa, attributed to their relatively low Fermi level density of states and comparatively weak electron-phonon coupling (EPC).

5.3 Computational Methods

We scrutinized the stable compositions of ternary Mg-Sc-H compounds ($MgSc_3H_x$, $MgSc_2H_x$, $MgScH_x$, Mg_2ScH_x, and Mg_3ScH_x, where x varies from 2 to 12, 14, 16, and 18) within the ternary convex hull at a constant pressure of 100 and 200 GPa. The search for crystal structures within the Mg-Sc-H systems was conducted using the USPEX (Universal Structure Predictor: Evolutionary Xtallography) software's evolutionary algorithm in conjunction with the first-principles structural optimization calculations based on density functional theory (DFT). Initial structures were randomly generated and subsequent structures were derived from 40% heredity, 40% randomness, 10% mutation, and 10% soft mutation.

The DFT structural optimization and enthalpies at specified pressures were computed using the VASP (Vienna ab initio simulation package) code. The interaction between electron-ion was characterized by the projector augmented wave (PAW) method with the plane-wave basis sets' cutoff energy set to 600 eV. The exchange-correlation functional was handled by the Perdew-Burke-Ernzerhof (PBE) implementation within the generalized gradient approximation (GGA). All structural models were visualized using VESTA.

The ternary convex hulls of $Mg_xSc_yH_z$ were built by evaluating their formation en-

thalpies concerning the enthalpies of Mg, Sc, and H single phases. The thermodynamic stability of the anticipated phase was gauged by comparing the formation enthalpies with the convex hull energy.

For $\Delta\mathcal{H}$, the enthalpy per formula unit (f.u.) of the Mg-Sc-H compound; the reference enthalpies of Mg, Sc, and H single phases are represented by $\mathcal{H}$(Mg), $\mathcal{H}$(Sc), and $\mathcal{H}$(H) respectively. The convex hull energy, denoted as $\Delta\mathcal{H}_f$, is attained by constraining the minimum value of the total enthalpies of a linear combination of stable phases, computable via the ConvexHull module in scipy. The energy above the convex hull, $E_{\text{above\_hull}}$, signifies that a corresponding ternary phase is stable if it equals zero, meaning the phase wouldn't decompose into any combination of elementary, binary, or other ternary phases. The stabilities of the predicted phases at a finite temperature can be examined using a similar approach, with computational details provided in the Supporting Information (SI).

We conducted predictions for the EPC and phonons of stable ternary Mg-Sc-H phases with the QE suite of programs [72, 124, 125], employing the PAW method and the PBE exchange-correlation functional [111]. The QE calculations featured a plane-wave basis sets cutoff energy set at 80 Ry. The chosen q-point mesh (k-point mesh for the EPC constant integral and T_c) in the Brillouin zone were as follows: $4 \times 4 \times 4$ ($16 \times 16 \times 16$) for MgScH6, $5 \times 5 \times 2$ ($20 \times 20 \times 8$) for Mg2ScH10, $3 \times 4 \times 4$ ($12 \times 16 \times 16$) for MgSc2H9, and $5 \times 5 \times 5$ ($20 \times 20 \times 20$) for $Mg(ScH4)_3$, respectively. The superconducting critical temperature was predicted using the McMillan formula [70] and the Eliashberg function derived from the EPC calculation.

5.4 Results and discussion

5.4.1 First-principles phase diagram of Mg-Sc-H system

In our quest to ascertain the high-pressure ternary phase diagram of the Mg-Sc-H system, we used the Mg-H and Sc-H binary systems [4, 123, 126–128] and the simple substances of the constituent elements (Mg, Sc, and H) [9, 129, 130] as reference points for thermo-

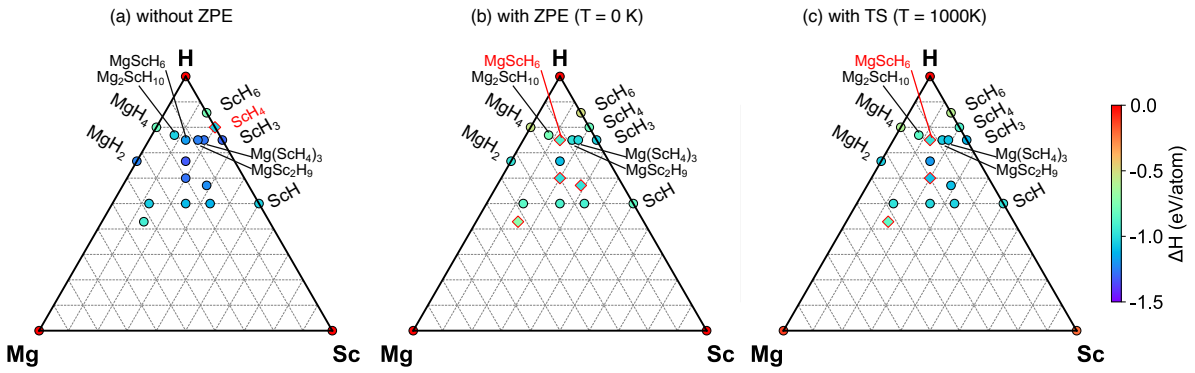

Figure 5.1: (a) Ternary convex hulls of the Mg-Sc-H system at a pressure of 200 GPa. (b) and (c) are the convex hulls of Gibbs free energy at 0K and a finite temperature (1000 K), respectively. The stable and metastable phases are shown by circles and diamond, respectively.

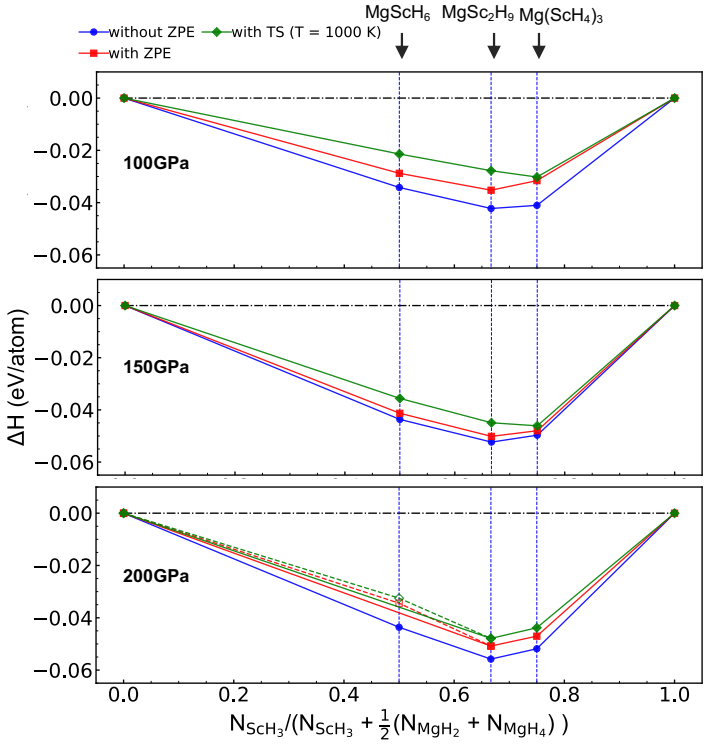

Figure 5.2: The enthalpy per atom of $(ScH_3)_{1-x}$ $\frac{1}{2}(MgH_2 + MgH_4)_x$ as a function of x at the pressure of 100, 150, and 200 GPa, where x is defined as $N_{ScH_3}/\left(N_{ScH_3} + \frac{1}{2}\left(N_{MgH_2} + N_{MgH_4}\right)\right)$. The stable phase and the metastable phase are connected by solid and dashed lines, respectively.

dynamic stability evaluation. It should be noted that the superconducting architectures of Mg-H and Sc-H binary hydride systems have only recently been identified. Specifically, MgH_6 and ScH_7 are predicted to display the highest T_c values in their respective binary systems, with values around 260 K and 169 K, respectively [4, 123, 126–128]. However, pressures exceeding 300 GPa are required to stabilize these two superconducting compounds, which is considerably beyond the typical high-pressure range (around 200 GPa) of most metal hydrides currently under investigation [4, 64, 85, 131].

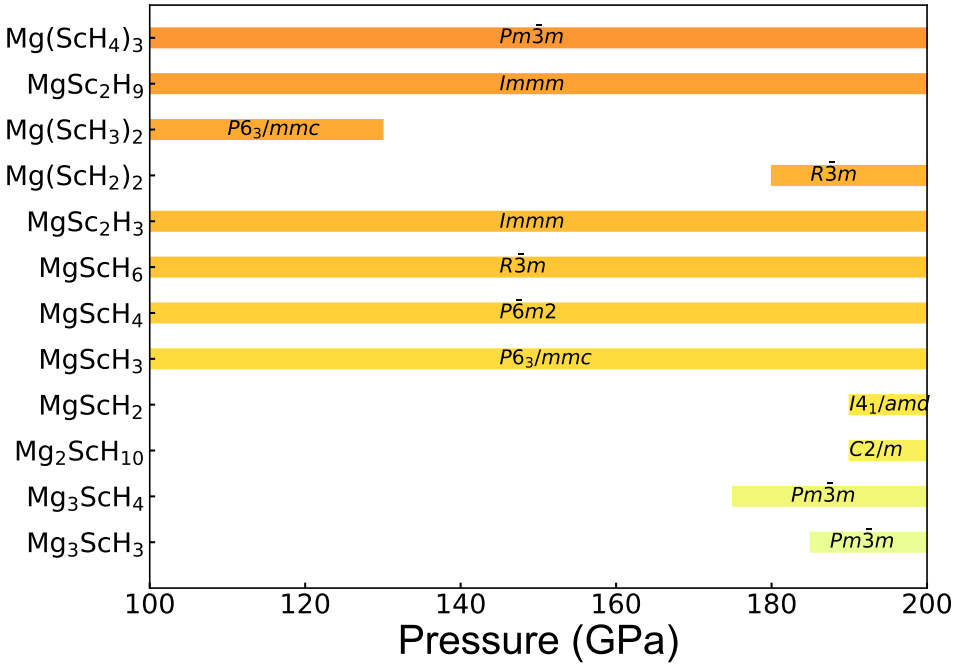

Figure 5.3: Phase diagram of Mg-Sc-H in the pressure range of 100–200 GPa.

In our quest to identify the most promising composition for subsequent experimental synthesis, we undertook a comprehensive sampling of the ternary Mg-Sc-H system's phase space, maintaining fixed pressures (100, 150, and 200 GPa). The ternary phase diagram for the Mg-Sc-H system at 200 GPa is presented in Figure 5.1, with findings at pressures of 100 and 150 GPa, alongside corresponding formation energies, being provided in the SI. Given the prevalence of high-pressure studies conducted under laser heating (1000-2000 K), certain metastable phases at 0 K might become stable at higher temperatures [107, 132]. Thus, we calculated the Mg-Sc-H system's ternary phase diagram at 200 GPa under three different scenarios: i) formation enthalpy without Zero Point Energy (ZPE), ii)

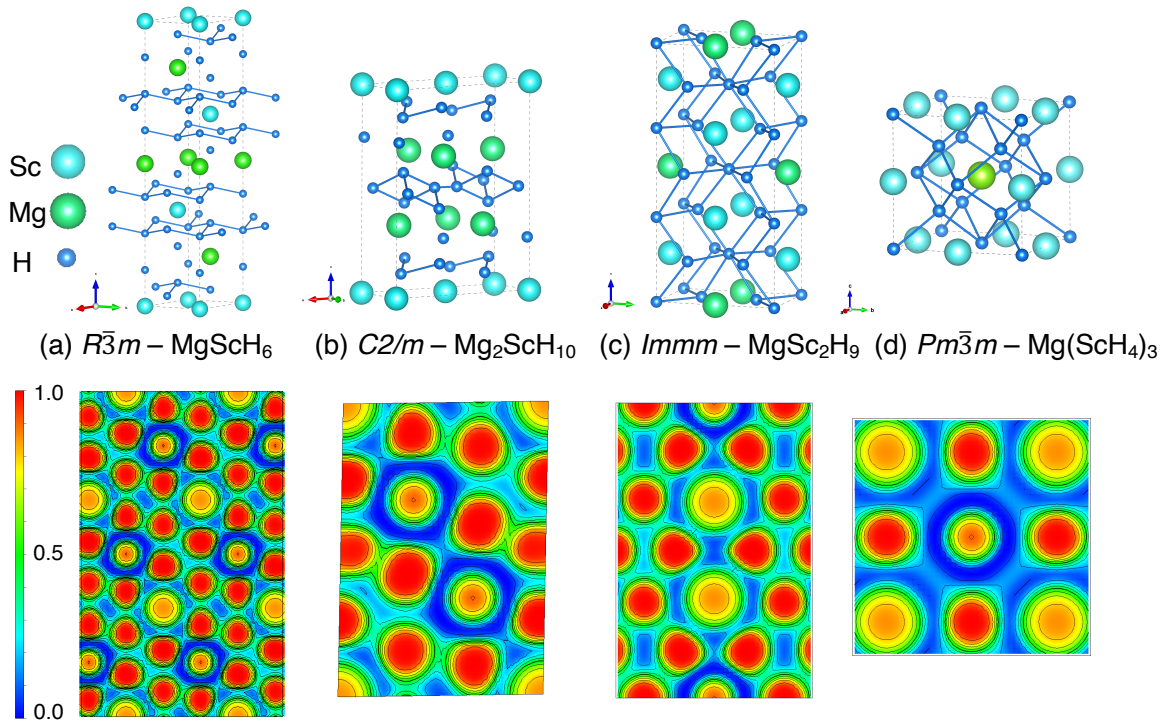

Figure 5.4: Predicted crystal structures of (a) $R\bar{3}m$-$MgScH_6$, (b) $C2/m$-Mg_2ScH_{10}, (c) $Immm$-$MgSc_2H_9$, (d) $Pm\bar{3}m$-$MgSc_3H_{12}$ at 200 GPa. Bottom panels show the corresponding contour plots of electron localization function (ELF) in these structures.

formation enthalpy accounting for ZPE but without entropy, and iii) Gibbs free energy accounting for the corresponding entropy contribution at 1000 K.

Turning our attention to Figure 5.1, we discovered the stable compounds within the Mg-Sc-H system's ternary convex hull at 200 GPa without ZPE. These include $Pm\bar{3}m$-Mg_3ScH_3, $Pm\bar{3}m$-Mg_3ScH_4, $C2/m$-Mg_2ScH_{10}, $I4_1/amd$-$MgScH_2$, $P6_3/mmc$-$MgScH_3$, $P\bar{6}m2$-$MgScH_4$, $R\bar{3}m$-$MgScH_6$, $Immm$-$MgSc_2H_3$, $R\bar{3}m$-$Mg(ScH_2)_2$, $P6_3/mmc$-$Mg(ScH_2)_3$, $Immm$-$MgSc_2H_9$, and $Pm\bar{3}m$-$Mg(ScH_4)_3$. Importantly, incorporating the ZPE contribution resulted in ScH_4 transitioning from a metastable to a stable state, aligning with Ye et al.'s findings [127] for the binary Sc-H system. In contrast, certain ternary hydrides, namely $Pm\bar{3}m$-Mg_3ScH_4, $P6_3/mmc$-$MgScH_3$, $R\bar{3}m$-$MgScH_6$, and $R\bar{3}m$-$Mg(ScH_2)_2$, shifted from a stable to a metastable state due to substantial ZPE contributions. At 1000 K, however, the entropy contribution of lattice vibration can restore the $R\bar{3}m$-$Mg(ScH_2)_2$ to a stable state. Though $Cmcm$-MgH_4 and $Cmcm$-ScH_6 in the binary Mg-H and Sc-H systems are stable compounds with the highest H content in the 100–200 GPa pressure range [123, 127], we haven't identified any stable compounds in the extremely hydrogen-rich cases within the same pressure range. Although high-T_c superconducting hydrides often tend to be hydrogen-rich compounds, our search in the pressure range of 100–200 GPa hasn't yielded any such stable compounds. The four aforementioned ternary compounds are situated on the convex hull planes, with energy differences of 0.003, 0.032, 0.008, and 0.015 eV/atom, respectively. Despite these findings, the quest for identifying hydrogen-rich stable compounds under high-pressure conditions continues.

With our focus on the stability of three ternary compounds, namely, $R\bar{3}m$-$MgScH_6$, $Immm$-$MgSc_2H_9$, and $Pm\bar{3}m$-$Mg(ScH_4)_3$, we have drawn comparisons with their binary counterparts: ScH_3, MgH_2, and MgH_4. The binary convex hulls of these compounds are depicted in Figure 5.2. It's important to highlight that only a handful of high-T_c ternary compounds, such as $(La,Y)H_6$ and $(La,Y)H_{10}$, have been chemically synthesized so far [106, 107]. The synthesis process involves mixing La-Y alloy with NH_3BH_3 under high pressure, followed by heating to over 2000 K using a laser [107].

Previous high-pressure experiments on the Sc-H and Mg-H systems have consistently

indicated the stable existence of only ScH_3 and MgH_2 [133–137]. This finding aligns well with earlier theoretical simulations [123, 126, 127, 138–140]. For ScH_3 chemical synthesis, a mix of Sc and NH_3BH_3 was utilized as the precursor, and then heated by a laser under high pressure to achieve stabilization. As inferred from the binary diagram in Figure 5.2, the ternary compounds $R\bar{3}m$-$MgScH_6$, $Immm$-$MgSc_2H_9$, and $Pm\bar{3}m$-$Mg(ScH_4)_3$ have potential to stabilize at 100 GPa irrespective of the temperature condition. Hence, akin to the approach adopted for $(La,Y)H_6$ and $(La,Y)H_{10}$, it's anticipated that these ternary Mg-Sc-H compounds can be successfully synthesized by combining the Mg-Sc alloy with NH_3BH_3 under high temperature and high pressure conditions.

The pressure-dependent phase stability of the Mg-Sc-H system, derived from the calculated formation of enthalpy without factoring in the ZPE contribution, is summarized in Figure 5.3. Here, it's notable that several phases, including $Pm\bar{3}m$-$Mg(ScH_4)_3$, $Immm$-$MgSc_2H_{10}$, $P\bar{6}m2$-$MgScH_4$, and $P6_3/mmc$-$MgScH_3$, have the potential to stabilize across a broad pressure range of 100 GPa to 200 GPa. The trend is particularly fascinating with Mg-rich ternary Mg-Sc-H phases showing stability closer to 200 GPa, while Sc-rich compounds, apart from $R\bar{3}m$-$Mg(ScH_2)_2$, demonstrating the same around 100 GPa. Notably, the compound $P6_3/mmc$-$Mg(ScH_2)_2$ exhibits stability in a narrower pressure range of 100–130 GPa. This tendency might be linked to the different stable pressure ranges of the Mg-H and Sc-H binary hydride systems. For instance, at lower pressures, the Sc-H system tends to accommodate a greater variety of stable compounds compared to the Mg-H system [123, 127].

5.4.2 Predicted superconductivity of Mg-Sc-H system

Prior investigations on alkali metals and alkaline earth hydrides have indicated a strong correlation between superconducting properties and hydrogen content, with higher T_c typically occurring in hydrogen-rich environments [4, 29]. As such, we are especially interested in $R\bar{3}m$-$MgScH_6$, $C2/m$-Mg_2ScH_{10}, $Immm$-$MgSc_2H_9$, and $Pm\bar{3}m$-$Mg(ScH_4)_3$, considering their high hydrogen composition, as well as their electronic structures and

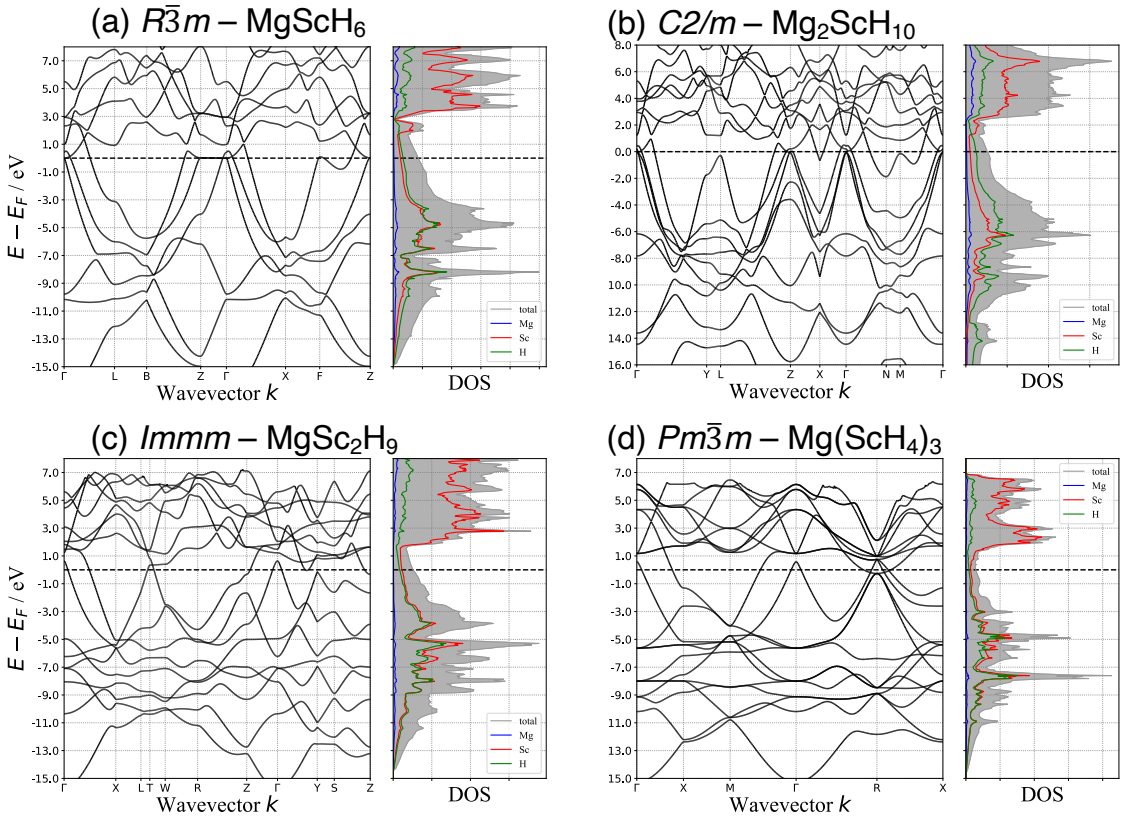

Figure 5.5: Electronic band structures and atom-projected electronic density of states of (a) $R\bar{3}m$-$MgScH_6$, (b) $C2/m$-Mg_2ScH_{10}, (c) $Immm$-$MgSc_2H_9$, (d) $Pm\bar{3}m$-$MgSc_3H_{12}$ at 200 GPa.

superconductivity.

The crystal structures and electron localization function (ELF) of these four compounds are depicted in Figure 5.4. $R\bar{3}m$-$MgScH_6$, which is stable above 100 GPa, exhibits a hexagonal crystal structure where each Mg and Sc atom is enveloped by 14 H atoms. The minimum H-H bond length in this structure is roughly 1.587 Å and the corresponding ELF value at the H-H bond center is around 0.4, suggesting an almost metallic nature. The unusually short interatomic distance in $C2/m$-Mg_2ScH_{10} gives rise to a significant ELF value of 0.7, denoting a potent covalent bond. For $Immm$-$MgSc_2H_9$ and $Pm\bar{3}m$-$Mg(ScH_4)_3$, the minimum H-H bond lengths are 1.628 Å and 1.650 Å, and their respective ELF values at the H-H bond center are 0.3 and 0.1. However, higher ELF values are observed at the H lattice sites. This suggests the chemical bonding in these structures is predominantly ionic. Interestingly, $Pm\bar{3}m$-$Mg(ScH_4)_3$ still forms a clathrate structure, where each Mg and Sc atom is surrounded by H_{14} cages. This structure could be seen as a result of replacing the central Sc in $Fm\bar{3}m$-ScH_3 with Mg. It should be noted that, as previously reported by Ye et al. [127], the $Fm\bar{3}m$-ScH_3 binary is not superconductive. Therefore, the superconductivity in $Pm\bar{3}m$-$Mg(ScH_4)_3$ is induced by the partial substitution of Sc in $Fm\bar{3}m$-ScH_3 by Mg.

Figure 5.5 depicts the computed electronic energy band structure and atom-projected electronic density of states (eDOS) for the four structures we previously mentioned. Each of them exhibits metallic characteristics at 200 GPa. Among these structures, $R\bar{3}m$-$MgScH_6$ presents the most substantial density of states at the Fermi level (E_F), while $Pm\bar{3}m$-$MgSc_3H_{12}$ shows the least. It is noteworthy that Sc and H atoms contribute predominantly to the density of states at E_F, with Mg atoms making a negligible contribution. In all four structures, the valence bands are primarily attributed to the strong hybridization between Sc and H atoms. Interestingly, at the E_F of $R\bar{3}m$-$MgScH_6$, doubly degenerate flat bands appear along the $\Gamma \rightarrow Z$ direction. This flat band phenomenon could potentially enhance the electron-phonon interaction [141], resulting in the highest T_c for $R\bar{3}m$-$MgScH_6$ among these structures.

Figure 5.6 presents the phonon band structure, atom-decomposed phonon density of states (pDOS), and Eliashberg spectra of $R\bar{3}m$-$MgScH_6$, $C2/m$-Mg_2ScH_{10}, $Immm$-$MgSc_2H_9$, and $Pm\bar{3}m$-$Mg(ScH_4)_3$ at 200 GPa. Notably, none of these four structures display imaginary modes, indicating their dynamic stability. Furthermore, their phonons can be distinctly divided into three frequency sectors. The low frequency area (below 20 THz) is chiefly associated with Mg and Sc atom vibrations, given their greater atomic masses. The middle (centered around 40 THz) and high frequency sectors (above 50 THz) are purely associated with the vibrations of H atoms.

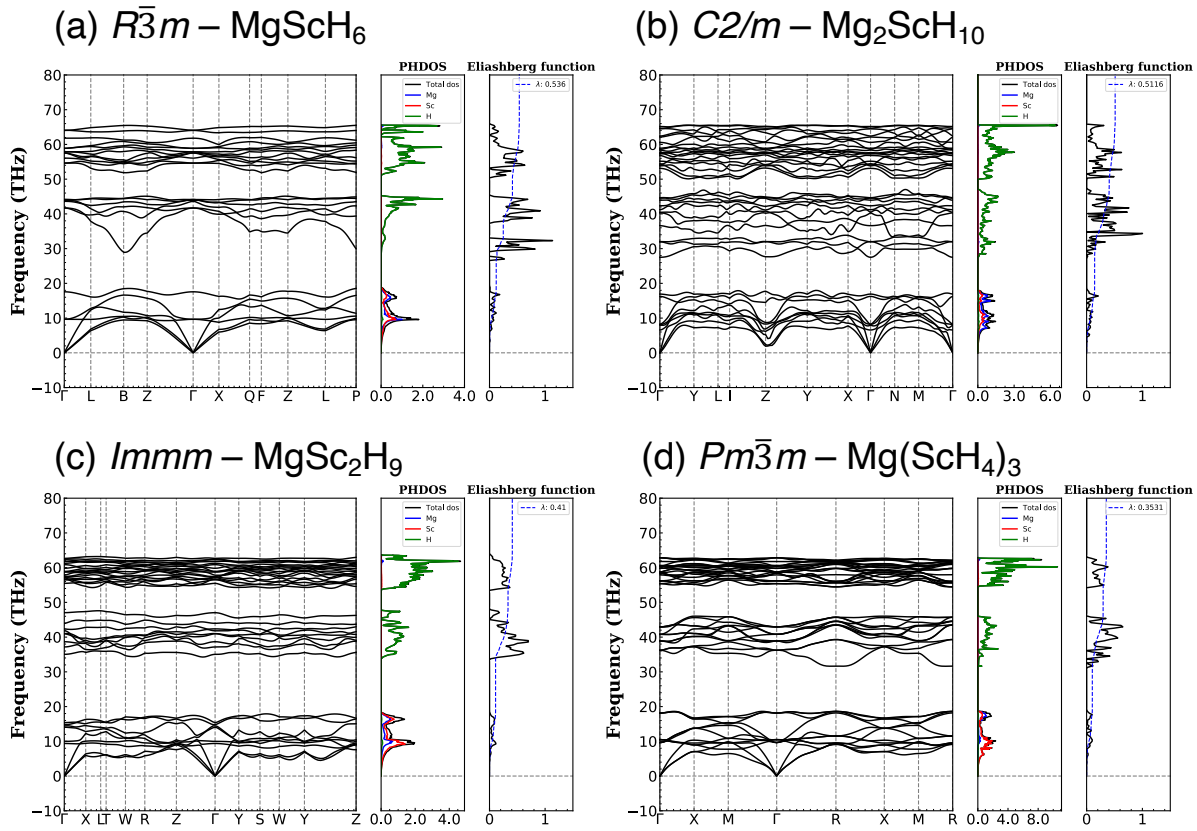

Figure 5.6: Phonon dispersion and atom-projected phonon density of states (pDOS), and Eliashberg spectral of (a) $R\bar{3}m$-$MgScH_6$, (b) $C2/m$-Mg_2ScH_{10}, (c) $Immm$-$MgSc_2H_9$, (d) $Pm\bar{3}m$-$MgSc_3H_{12}$ at 200 GPa.

Table 6.1 provides the computed T_c values along with their associated properties at 200 GPa. The four structures follow the electron-phonon coupling (EPC) constants (λ) sequence as: $R\bar{3}m$-$MgScH_6$ > $C2/m$-Mg_2ScH_{10} > $Immm$-$MgSc_2H_9$ > $Pm\bar{3}m$-$Mg(ScH_4)_3$.

This pattern is also reflected in their T_c values. The highest T_c at 200 GPa (23.3 K) is recorded for $R\bar{3}m$-$MgScH_6$. Yet, this superconducting temperature is significantly lower than those reported for other high-hydrogen-content metal hydrides like LaH_{10} and YH_{10}. [4, 29]

Overall, the superconducting T_c is influenced by the electron-phonon interaction. Despite the similar logarithmic phonon averages ω_{log} of the four Mg-Sc-H compounds, which align with those of LaH_{10} and YH_{10}, their EPC constants are distinctly different. As displayed in Fig. S3 (a), the total DOS at the Fermi level ($N_t(E_F)$) of LaH_{10} and YH_{10} surpasses that of the Mg-Sc-H compounds. More precisely, the difference lies in the H atoms' contributions to $N_t(E_F)$, as illustrated in Fig. S3 (b). According to BCS theory [142], $N_t(E_F)$ positively correlates with superconducting T_c. Hence, the relatively lower contribution of H atoms to $N_t(E_F)$ in these compounds inhibits the achievement of high-T_c superconductivity.

It's worth mentioning that YH_3 and $Fm\bar{3}m$-ScH_3 share the same hydrogen content per metal atom as $R\bar{3}m$-$MgScH_6$, $Immm$-$MgSc_2H_9$, and $Pm\bar{3}m$-$Mg(ScH_4)_3$. However, YH_3 showcases a robust EPC constant of 1.6 and a T_c around 40 K. [143] In contrast, $Fm\bar{3}m$-ScH_3 has an EPC constant of about 0.23, scarcely inducing superconductivity. [127] The Mg-Sc-H structures' EPC constants range from 0.35 to 0.54, leading to T_c values lower than that of YH_3.

Figure 5.7 illustrates the dependence of superconducting T_c and related properties on pressure for $R\bar{3}m$-$MgScH_6$, $C2/m$-Mg_2ScH_{10}, $Immm$-$MgSc_2H_9$, and $Pm\bar{3}m$-$Mg(ScH_4)_3$. Notably, their T_c values consistently decline as pressure increases, whereas the ω_{log} and λ trends oppose this. As demonstrated in Figs. S4 and S5, the $N_t(E_F)$ for all compounds reduces as pressure rises. H atoms, in contrast to Mg and Sc atoms, contribute dominantly to $N_t(E_F)$, leading to its negative pressure-dependence. Hence, the T_c and λ for these compounds show similar trends under pressure. The phonon and EPC spectra at different pressures are depicted in Figs. S6, S7, S8, and S9.

The four compounds' λ values decrease with the rise in pressure, more prominently

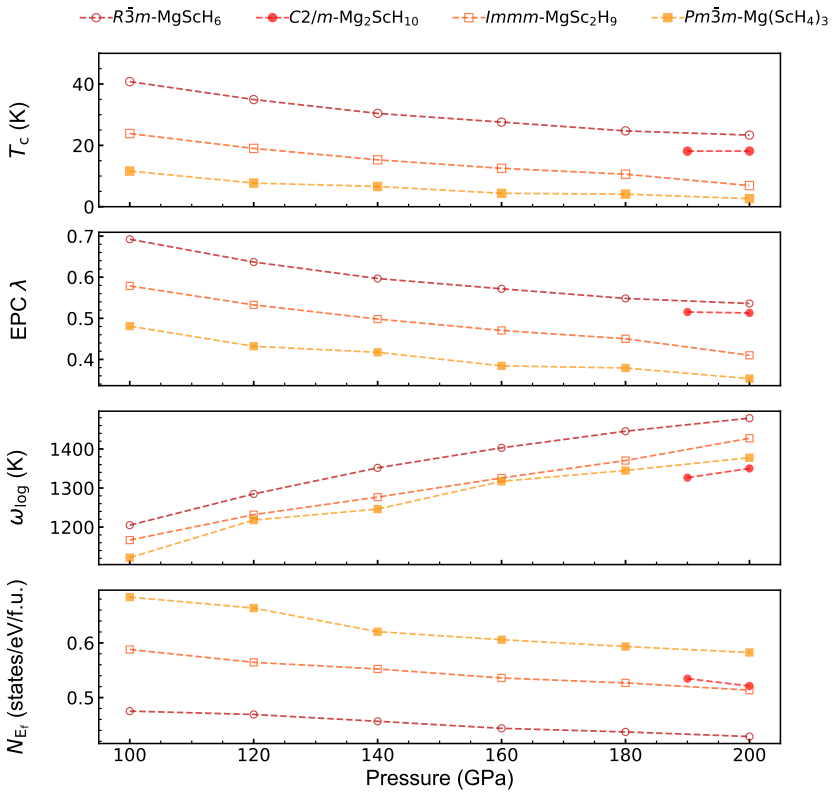

Figure 5.7: Pressure-dependent superconductivity of $R\bar{3}m$-$MgScH_6$, $C2/m$-Mg_2ScH_{10}, $Immm$-$MgSc_2H_9$, $Pm\bar{3}m$-$MgSc_3H_{12}$. (a) T_c from the McM equation, (b) EPC constant λ, (c) logarithmic phonon average ω_{log} and (d)the total DOS at the Fermi level N_{E_f}.

for phonon frequencies above 20 THz (dominated by H atoms). In the Eliashberg spectral function, a positive correlation is seen between T_c, ω_{log}, and λ. Overall, increasing pressure leads to diminishing EPC constants (λ) and consequently lower T_c.

To conclude, the predicted T_c for $R\bar{3}m$-$MgScH_6$ at 100 GPa (41 K) slightly surpasses the McMillan limit (39 K). [70] On the contrary, MgH_4, with a higher hydrogen-to-metal content ratio, can only reach 38 K at the same pressure. [128] Even though $R\bar{3}m$-$MgScH_6$'s EPC constant is slightly below that of MgH_4, its ω_{log} (1204 K) aligns with those of LaH_{10} and YH_{10}. Despite initial calculations suggesting low T_c for ScH_3, [127] recent experiments at high pressure have recorded a T_c around 20 K in the 130-160 GPa pressure range. [135] We theoretically propose that $R\bar{3}m$-$MgScH_6$ is stable at 100 GPa under both room and high temperatures, with its predicted T_c surpassing those of parent compounds (ScH_3, MgH_2, and MgH_4). This presents a promising candidate for superconducting metal hydride experiments under high pressure.

Table 5.1: T_c estimated by McMillan formula using first-principles phonon calculations for Mg-Sc-H at each pressure. λ and ω_{log} are the parameters appearing in the formula.

Phase	Space group	P (GPa)	λ	ω_{log} (K)	N_{E_F} (states/eV/Å^3)	T_c (K) at $\mu = 0.1 - 0.13$
$MgScH_6$	$R\bar{3}m$	200	0.536	1478.84	0.0150	23.34 – 15.08
Mg_2ScH_{10}	$C2/m$	200	0.512	1350.17	0.0125	17.94 – 11.10
$MgSc_2H_9$	$Immm$	200	0.410	1427.39	0.0120	6.88 – 3.14
$Mg(ScH_4)_3$	$Pm\bar{3}m$	200	0.353	1377.73	0.0102	2.61 – 0.83

5.5 Conclusion

To sum up, we've utilized the evolutionary algorithm in the USPEX code and first-principles calculations to investigate the ternary phase diagram of the Mg-Sc-H system under pressures ranging from 100 to 200 GPa. Our research indicates that Sc-rich Mg-Sc-H compounds tend to stabilize around 100 GPa, while Mg-rich counterparts appear to become stable above 180 GPa. Superconductivity is expected in Mg-Sc-H hydrides where the hydrogen/metal ratio is approximately three. Specifically, $R\bar{3}m$-$MgScH_6$ exhibits a

superconducting transition temperature around 41 K at 100 GPa. Despite the relatively low superconducting transition temperature of $Pm\bar{3}m$-$Mg(ScH_4)_3$, it's expected to maintain stability toward 100 GPa in the lower high-pressure range. This study contributes valuable insights towards the identification of new low-pressure superconducting hydrides.

Chapter 6

Potential high-T_{C} superconductivity in $YCeH_x$ and $LaCeH_x$ under pressure

6.1 Motivation

In this chapter, we begins with the investigation of the Y-Ce-H and La-Ce-H ternary systems, sailing from the La-Y-H to the Y-Mg-H ternary systems. Our desire to further lower superconducting transition temperatures and examine a fascinating area of high-pressure physics, the world of strongly correlated systems, has led us to investigate these systems.

In-depth knowledge of the complicated interplay between chemical composition, structural complexity, and pressure on the superconductivity of hydride systems has been gained from analysis of the La-Y-H and Y-Mg-H systems. These s and d block elements showed exceptional high-temperature superconducting properties, although they only touch on a small percentage of the wide range of possible superconductors' characteristics.

Now, our attention is drawn to the f-block element, Cerium (Ce), part of the lanthanide series on the periodic table. Materials based on Ce exhibit distinctive electronic properties, largely due to their categorization as strongly correlated systems. The "strong correlation" represents systems where electron-electron interactions profoundly affect their properties.

Conventional band theory, which treats electrons as almost independent entities, inadequately elucidates these materials, making them an exciting prospect for discovering unique phenomena.

The significant characteristic of Ce-based materials is their extraordinary electronic tunability upon changes in temperature, pressure, or chemical composition, resulting in a plethora of complex and often rival ground states, such as superconductivity, magnetism, and heavy fermion behavior. Therefore, an investigation into the effects of pressure on the superconducting characteristics of the Y-Ce-H and La-Ce-H systems provides an opportunity to understand how strong electronic correlations can be modulated to achieve high-temperature superconductivity.

Furthermore, investigating the influence of strong correlations in the d and f electron systems on the superconductivity of hydrides could provide fundamental insights into the mechanisms driving high-temperature superconductivity. This knowledge could be pivotal in the quest for room-temperature superconductors, revolutionizing numerous technological applications.

Therefore, the research on the Y-Ce-H and La-Ce-H systems under pressure represents a novel and thrilling direction in the field of high-pressure superconductivity. It holds the promise of unveiling new superconducting states and deepening our understanding of the intricate physics of strongly correlated materials.

6.2 Research Background

Superconductivity, due to its distinctive phenomenon and expansive array of industrial applications, has drawn considerable interest and seen significant advancements. [144–150] Nonetheless, the extreme low-temperature conditions necessary for these properties to emerge pose substantial limitations to their applicability. Consequently, the quest for high- or room-temperature superconductivity has remained a top target in the field of superconductivity over time. [1, 151, 152] In accordance with the Bardeen-Cooper-Schrieffer (BCS) theory, there is a notable association between the superconducting tran-

sition temperature (T_c) and the phonon vibration frequency. [142, 153–155] Therefore, metallic hydrogen, due to its ultra-high phonon vibration frequency, has been deemed the ultimate candidate for high-T_c superconductivity. [76] Yet, the Wigner-Huntington transition, also known as hydrogen metallization, often necessitates extraordinarily high pressures, complicating the investigation of its superconductivity-related electrical properties under such conditions. [156–163] To address this, Ashcroft suggested the incorporation of other elements into hydrogen, which can provide the essential pre-compression for the whole system, enabling it to preserve metallicity and superconductivity under less extreme pressures. [13] As such, metal hydrides emerge as prime candidates for high-T_c superconductivity.

As per Ashcroft, almost every binary hydride has undergone theoretical scrutiny through density functional theory (DFT) calculations, with several predictions being confirmed through experimental means. [2, 4, 5, 17, 21, 22, 29, 93, 117, 131, 135, 164–169] However, multi-component superconducting hydrides have received marginally less research attention in comparison to binary ones. Given the greater elemental combinations within multi-component hydrides, they hold more potential for the discovery of high or room-temperature superconductivity. [17, 33, 34, 82, 83, 85, 86, 88, 91, 95, 106, 107, 170–178]

For instance, DFT calculations by Sun *et al.* [34] proposed that magnesium hydride can dissociate an H_2 molecule into atomic H via lithium doping. This process raises the electron concentration at the Fermi level (E_F), allowing for a T_c value of 473 K at 250 GPa to be achieved. [34] Additionally, a recent high-pressure experiment demonstrated that minimal carbon doping in H_3S could induce room-temperature superconductivity (T_c = 287.7 ± 1.2 K at 267 ± 10 GPa), [81] even though the AC susceptibility anomaly in low temperature for the carbonaceous sulfur hydride has been challenged by Hirsch *et al.* [179, 180] Hence, more robust experimental data is required to substantiate the observation of room-temperature superconductivity.

Therefore, elevating the electronic states' density at E_F through electron doping in binary hydride can influence the T_c value; nonetheless, this alteration may also lead to a

decline in T_c under certain circumstances. [103, 181, 182]

Moreover, the majority of high-T_c superconducting hydrides reported to date are found primarily in the "lability belt" of the Mendeleev table. These hydrides often exhibit peculiar structural characteristics, such as hydrogen-enveloped cage-like formations. [29]

Ternary superconducting hydrides like $ScYH_6$, $ScCaH_8$, $CaYH_{12}$, among others, can be readily synthesized by substituting one metal atom in the binary parent compound. [85, 88, 107, 172, 173] The crystalline structure, stability pressure range, unit cell volume, and other traits of the progenitor binary superconducting hydrides closely resemble those of the derived ternary superconducting hydrides. [1, 29]

For example, the combination of two binary hydrides sharing similar structural features could yield a structurally akin but more stable ternary hydride. This hypothesis was put to the test, observing that CeH_9, YH_9, LaH_{10}, and CeH_{10} share similar qualities across several properties, with their structural traits validated via high-pressure experiments. [5, 21, 117, 168]

Correspondingly, the associated ternary superconducting hydride, $(La,Y)H_{10}$, has been successfully synthesized experimentally. The T_c observed under high pressure also closely aligns with the theoretically predicted T_c. [107]

During our work, we noted a recent high-pressure experiment study suggesting that La-Ce-H may possess stable $I4/mmm$-$(La,Ce)H_4$ and $Im\bar{3}m$-$(La,Ce)H_6$ around 100 GPa. [183]

In light of this, our focus will be on the $YCeH_x$ and $LaCeH_x$ systems, which are yet to be extensively explored, to ascertain the presence of stable compounds under high pressure. Leveraging the evolutionary algorithm for crystal structure prediction, we have theoretically identified thermodynamically stable compounds including $YCeH_5$,$YCeH_7$,$YCeH_8$, $YCeH_{18}$, $YCeH_{20}$, $LaCeH_8$, $LaCeH_{18}$, and $LaCeH_{20}$ in the pressure range of 100-400 GPa.

Moreover, we conducted an examination of the dynamic stability and superconductivity of these hydrogen-rich ternary hydrides, adhering to the harmonic approximation. With increasing pressure, all of these compounds proved to be dynamically stable. Of particular significance, $YCeH_{18}$ showcased exceptionally strong electron-phonon coupling,

with superconducting transition temperatures reaching 173 K at 150 GPa.

6.3 Method

We conducted a search for the crystal structure of $YCeH_x$ and $LaCeH_x$ ($x = 2{\sim}10$, 12, 14, 16, 18, and 20) at pressures of 100, 200, and 300 GPa using the USPEX software (Universal Structure Predictor: Evolutionary Xtallography) [36, 184]. During the USPEX run, the initial generation was composed of 200 structures with 1-2 formula units randomly created. Subsequent generations of 100 structures each were produced using a blend of 40

The optimization of the structure was accomplished using density functional theory calculations within the generalized gradient approximation (GGA), featuring the Perdew-Burke-Ernzerhof (PBE) exchange-correlation functional [111], as implemented in the VASP (Vienna *ab initio* simulation package) [73, 185] code. The interaction between electrons and ions was handled using projector-augmented-wave (PAW) potentials [73, 185], with the Ce 4f electrons explicitly taken into account in the valence electrons. We set the cutoff energy for plane waves to 600 eV, and the smallest allowed spacing between the k-points in the irreducible Brillouin zone was fixed at 0.2 $^{-1}$.

For a closer look at the chemical bonding and electronic structures of selected stable $YCeH_x$ and $LaCeH_x$ variants, we carried out static calculations using the VASP code. We then executed Crystal Orbital Hamilton Population (COHP) and Crystal Orbital Bond Index (COBI) analyses using the Lobster 4.1.0 package, along with the pbeVaspFit2015 basis set. We also verified the electronic band structures by considering the spin-orbit coupling (SOC) interaction and the correction of the on-site Coulomb interaction of Ce 4f orbitals, employing the DFT+U method of Dudarev *et al.* [55] in the latter instance. Using the density-functional perturbation theory approach as implemented in the HP package [186], we determined the Hubbard U parameter for Ce 4f orbitals to be 4.2 eV, which is in line with the value (i.e., 4.5 eV) used by Wang *et al.* [116] for their study on CeH_9. We adopted the exchange interaction parameter J for Ce 4f orbitals from Ref. 116, setting it to 0.5 eV.

We calculated the formation enthalpies of the La-Ce-H and Y-Ce-H ternary systems (hereafter referred to as A-Ce-H, where A = La and Y), in relation to the elemental solids Y [187], Ce [188], La [189], and H [9], at each defined pressure as follows:

$$\Delta\mathcal{H} = \frac{1}{x+y+z}\left[\mathcal{H}(A_x\mathrm{Ce}_y\mathrm{H}_z) - x\mathcal{H}(A) - y\mathcal{H}(\mathrm{Ce}) - z\mathcal{H}(\mathrm{H})\right], \tag{6.1}$$

In this equation, $\mathcal{H}(A_x\mathrm{Ce}_y\mathrm{H}_z)$ refers to the enthalpy per formula unit (f.u.) of the A-Ce-H compound; $\mathcal{H}(A)$, $\mathcal{H}(\mathrm{Ce})$, and $\mathcal{H}(\mathrm{H})$ represent the reference enthalpies for A, Ce, and H single phases, respectively. The predicted phase's thermodynamic stability is assessed by comparing its formation enthalpies with the energy of the convex hull:

$$E_{\mathrm{above\_hull}} = \Delta\mathcal{H} - \Delta\mathcal{H}_f, \tag{6.2}$$

The convex hull energy, represented by $\Delta\mathcal{H}_f$, is established by restricting the minimum value of the cumulative enthalpies of a combination of stable phases [190], computed through the ConvexHull module in scipy [191]. The energy above the convex hull is denoted as $E_{\mathrm{above\_hull}}$. If $E_{\mathrm{above\_hull}} = 0$, it suggests that the corresponding ternary phase is stable and wouldn't decompose into any blend of elementary, binary, or other ternary phases. The Gibbs free energies at various temperatures were computed in the quasiharmonic approximation using the PHONOPY code [69]. After incorporating the Gibbs free energies, we can calculate the system's stability at high temperatures by calculating the convex hull.

The stable ternary phases' phonon dispersion and electron-phonon coupling (EPC) were analyzed using the Quantum ESPRESSO (QE) code [72], with the PAW method and the GGA-PBE exchange-correlation functional. Specifically, the Ce PAW potential was created with a valence configuration of $4d^{10}5s^25p^64f^{0.5}5d^{1.5}6s^2$, provided by Dal Corso's PSLibrary [192]. The QE calculations' cutoff energy for plane-wave basis sets was set to 180 Ry. The q-point mesh (and integrated k-points mesh) for EPC calculations in the first Brillouin-zone was determined as follows: $5\times5\times2$ ($20\times20\times8$) for $A\mathrm{CeH}_8$, $5\times5\times3$

(20 × 20 × 12) for ACeH$_{18}$, and 4 × 4 × 4 (20 × 20 × 20) for ACeH$_{20}$ (A being La and Y). The superconducting critical temperature prediction used the Allen-Dynes-modified McMillan formula (AD) and the Eliashberg function obtained from the EPC calculation, expressed as follows [70, 71]:

$$T_c = \frac{\omega_{\log} f_1 f_2}{1.2} \exp\left(\frac{-1.04(1+\lambda)}{\lambda(1-0.62\mu^*)-\mu^*}\right), \tag{6.3}$$

with

$$\begin{aligned} f_1 f_2 &= \sqrt[3]{1+\left[\frac{\lambda}{2.46(1+3.8\mu^*))}\right]^{\frac{3}{2}}} \\ &\times \left[1-\frac{\lambda^2(1-\omega_2/\omega_{\log})}{\lambda^2+3.312(1+6.3\mu^*)^2}\right]. \end{aligned} \tag{6.4}$$

When $f_1 f_2 = 1$, Eq. (6.3) is restored to the original McMillan formula (McM). The μ^* is the Coulomb pseudopotential, which is defined as below [71]

$$\mu^* = \frac{\mu}{1+\mu\log(\omega_{\rm el}/\omega_{\rm ph})}, \tag{6.5}$$

Here, μ signifies instant repulsion, while $\log(\omega_{\rm el}/\omega_{\rm ph})$ represents the time ratio for propagation. Factoring in both previous experimental and calculated data, μ^* for most metal compounds typically falls within the range of 0.1 to 0.16. In this context, a commonly accepted value of 0.1 was utilized for μ^*. The definitions of the electron-phonon coupling constant (λ), logarithmic average phonon frequency ($\omega_{\log}$), and mean square frequency (ω_2) are as follows:

$$\lambda = 2\int \frac{\alpha^2 F(\omega)}{\omega} d\omega, \tag{6.6}$$

$$\omega_{\log} = \exp\left[\frac{2}{\lambda}\int \frac{d\omega}{\omega}\alpha^2 F(\omega)\log\omega\right], \tag{6.7}$$

and

$$\omega_2 = \sqrt{\frac{1}{\lambda}\int\left[\frac{2\alpha^2 F(\omega)}{\omega}\right]\omega^2 d\omega}, \tag{6.8}$$

respectively.

6.4 Results and discussion

6.4.1 Phase stability and crystal structural of $YCeH_x$ and $LaCeH_x$

Due to the computational demands associated with predicting the complete ternary phase diagram, and the main objective of this study being the determination of stability and superconductivity in hydrogen-rich phases, the research emphasizes stable compounds and crystal structures at pressures of 100 GPa, 200 GPa, and 300 GPa. A selective pathway was traced by focusing on $YCeH_x$ and $LaCeH_x$ (x = 2-8, 10, 12, 14, 16, 18, and 20) for a specified composition search. This method has been proven to be effective for alkaline earths and rare earth metal ternary hydrides. [85, 135, 176] In the case of stability analysis for $YCeH_x$ and $LaCeH_x$, the related Y-H, La-H, and Ce-H binary hydrides have been widely studied. [5, 21, 166] Existing theoretical calculations indicate a hydrogen-rich structure MH_9 (M = Y, La, and Ce) that can stabilize below 100 GPa in these three binary systems. Furthermore, YH_{10} has shown potential for room temperature superconductivity. [4] This study, thus, mainly utilizes these stable binary hydrides alongside individual elements as benchmarks for evaluating thermodynamic stability.

In Fig. 6.1, the constructed convex hulls for $YCeH_x$ and $LaCeH_x$ at 200 GPa are illustrated, with the circles and red diamonds representing their stable and metastable phases, respectively. More in-depth findings regarding the stability of $YCeH_x$ and $LaCeH_x$ at various pressures are detailed in Figs. S1-S6 in the Supplementary Material (SM).

At 100 GPa, $YCeH_5$, $YCeH_7$, $YCeH_8$, $LaCeH_8$, and $LaCeH_{18}$ exhibit stability. With an increase in pressure up to 200 GPa, $YCeH_5$, $YCeH_7$, and $LaCeH_{18}$ are no longer part of the ternary convex, while $LaCeH_{20}$ and $YCeH_{18}$ emerge as stable phases within the convex hull. $YCeH_{20}$ doesn't achieve stability within the pressure range of 100-300 GPa, but becomes stable when pressure exceeds 300 GPa, aligning with the stable pressure interval of YH_{10}. [4]

Furthermore, between 300-400 GPa, $LaCeH_8$, $LaCeH_{20}$, and $YCeH_{20}$ transition to the more stable $Pmmn$, $P6_3/mmc$, and $P4/mmm$ phases, respectively. The stability pressure ranges for these newly predicted phases are summarized in Fig. **??**.

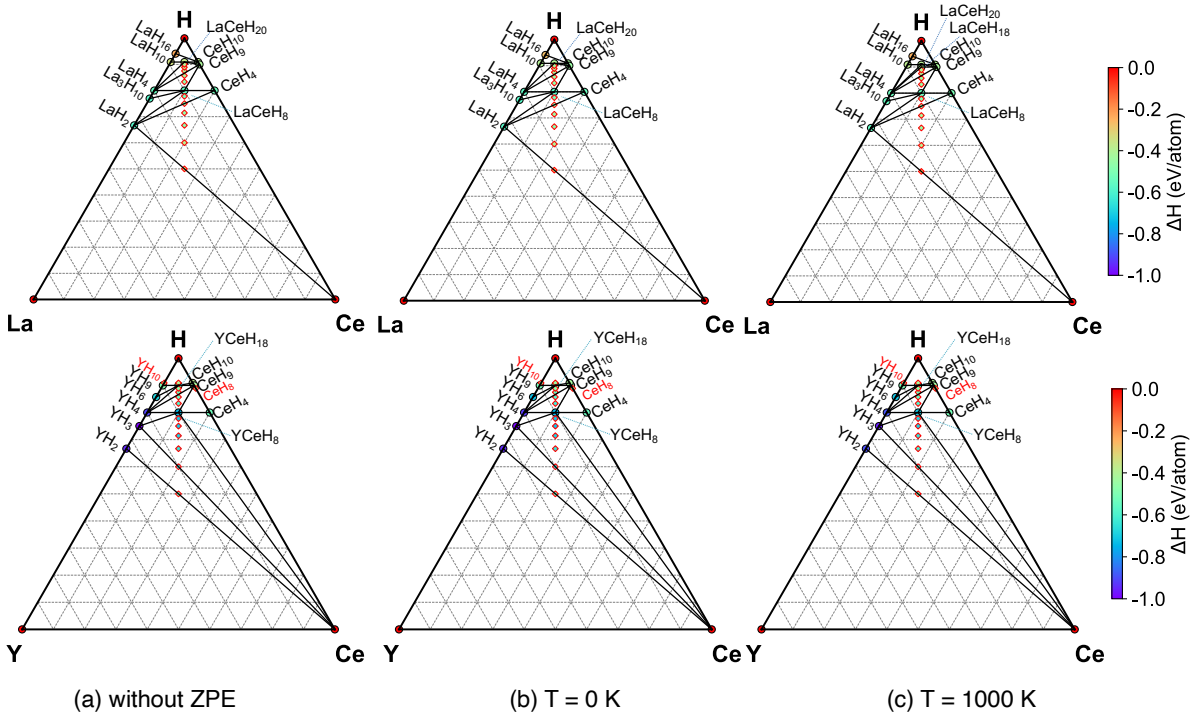

Figure 6.1: Ternary convex hulls of $YCeH_x$ and $LaCeH_x$ at 200 GPa. The stable and metastable phases are highlighted by the symbols of circles and red diamond, respectively. The right panels are the convex hull at 0 K (with the correction of zero-point energy) and 1000 K.

To investigate the thermal decomposition resistance of these phases, we computed the ternary convex hull at a finite temperature of 200 GPa. Stable phases ($YCeH_8$, $YCeH_{18}$, $LaCeH_8$, and $LaCeH_{20}$) at this point maintain stability even at elevated temperatures, with their specific energy values presented in the SM.

Remarkably, most of the predicted stable phases, apart from $YCeH_5$ and $YCeH_7$, comprise clathrate structures encapsulated by H, such as the ones in $YCeH_8$, $LaCeH_8$, $YCeH_{18}$, $LaCeH_{18}$, and $YCeH_{20}$ shown in Fig. 6.2. Since hydrogen-rich compounds are more likely to exhibit high-T_c superconductivity [1], the hydrogen-deficient ones like $YCeH_5$ and $YCeH_7$ are addressed separately. The stable hydrides of $YCeH_x$ and $LaCeH_x$ featuring clathrate structures are broadly categorized into three groups.

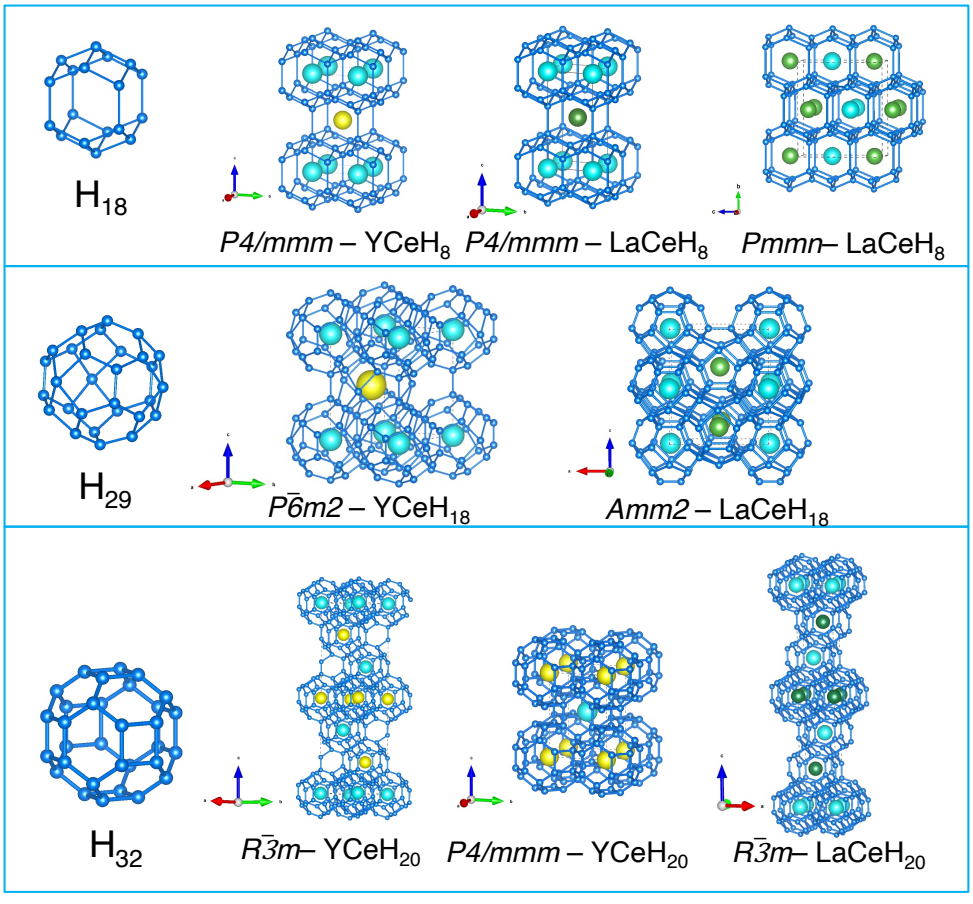

Figure 6.2: The clathrate structures of stable $YCeH_x$ and $LaCeH_x$.

(i) The first group is composed of H_{18} cages, found in $P4/mmm$-$YCeH_8$, $P4/mmm$-$LaCeH_8$, and $Pmmn$-$LaCeH_8$. These are derived from the respective parent compounds

($I4/mmm$-YH_4, $I4/mmm$-CeH_4, and $I4/mmm$-LaH_4) [4] having similar cage structures. The $P4/mmm$ ternary phase results from orderly replacing half of the Ce atoms at the $2a$ site in the $I4/mmm$-CeH_4 phase with either Y or La atoms [4]. Figs. S1 and S4 present the relative enthalpies of these two structures for $LaCeH_4$ and $YCeH_4$. It is observed that the most stable candidate structures favor the H_{18} cages. Furthermore, $LaCeH_8$ transitions into the $Pmmn$ phase when the pressure surpasses 300 GPa.

(ii) The second group is characterized by H_{29} cages, observed in the $P\bar{6}m2$-$YCeH_{18}$ and $Amm2$-$LaCeH_{18}$ phases. The $P\bar{6}m2$-$YCeH_{18}$ phase is obtained by replacing half of the Ce atoms at the $2d$ site of $P6_3/mmc$-CeH_9 with Y atoms. As for the progenitor compounds of $P\bar{6}m2$-$YCeH_{18}$ and $Amm2$-$LaCeH_{18}$, Peng *et al.* [4] have shown that only the stable $P6_3/mmc$-YH_9 and $P6_3/mmc$-CeH_9 phases persist within the 100-400 GPa pressure range, while LaH_9 does not. For the $Amm2$-$LaCeH_{18}$ phase, only its internal energy counteracts its potential decomposition pathway of $1/6\ LaH_4 + 1/6\ LaH_{10} + CeH_9$, preventing its stabilization at higher pressures [4, 122].

(iii) The third group contains the H_{32} cages, as observed in $YCeH_{20}$ and $LaCeH_{20}$. The $R\bar{3}m$-$YCeH_{20}$ and $R\bar{3}m$-$LaCeH_{20}$ phases share the same spatial structure with $LaYH_{20}$, [107] all of which are supercell structures of their parent phases $Fm\bar{3}m$-AH_{10}. Specifically, the equivalent primitive unit cell of $R\bar{3}m$-$YCeH_{20}$ can be derived from the $1 \times 1 \times 2$ extension of the primitive unit cell of $Fm\bar{3}m$-CeH_{10}, replacing half of the Ce atoms with Y atoms. $LaCeH_{20}$ undergoes a phase transition from $R\bar{3}m$ to $P6_3/mmc$ under specific conditions. For $YCeH_{20}$, it too undergoes a phase transition at 370 GPa; the emerging high-pressure phase is derived by replacing half of the Ce atoms at the $4b$ site in the parent phase $Fm\bar{3}m$-CeH_{10} with Y atoms. Given the chemical similarity of elements, using the stable phases of binary hydrides as starting structures could expedite the search for multi-component hydrides.

To further validate the lattice dynamic stability of the projected $YCeH_x$ and $LaCeH_x$ phases, we initially computed their phonon band structures using the Phonopy code [69], with results presented in Fig. S7 of the Supplementary Material. Notably, the $Amm2$-$LaCeH_{18}$ phases fail to maintain dynamic stability within their respective thermodynamic

stability pressure range. For the $R\bar{3}m$-$LaCeH_{20}$ phase to reach dynamic stability, the pressure must exceed 200 GPa. Moreover, the pressure range applied in current prevalent experimental research of metal hydrides typically falls between 100-300 GPa. In terms of phases stabilized beyond 300 GPa, both $R\bar{3}m$-$YCeH_{20}$ and $R\bar{3}m$-$LaCeH_{20}$ display significant similarities. Consequently, our focus is predominantly on the $P4/mmm$-$YCeH_8$, $P\bar{6}m2$-$YCeH_{18}$, $R\bar{3}m$-$YCeH_{20}$, $P4/mmm$-$LaCeH_8$, and $R\bar{3}m$-$LaCeH_{20}$ phases regarding their electronic properties and superconductivity.

6.4.2 Electronic Properties and Superconductivity

The electronic band structure and electronic density of states (eDOS) for $P4/mmm$-$YCeH_8$, $P\bar{6}m2$-$YCeH_{18}$, $R\bar{3}m$-$YCeH_{20}$, $P4/mmm$-$LaCeH_8$, and $R\bar{3}m$-$LaCeH_{20}$ under high pressures are shown in Supplementary Material Figs. S8-S10. Within their thermodynamic stability range, all these compounds exhibit metallic characteristics in their energy band structures. Steep conduction bands crossing the Fermi level (E_F) are noted for $P4/mmm$-$YCeH_8$ and $P4/mmm$-$LaCeH_8$ along the $Z \rightarrow \Gamma$ direction, resulting in electron pockets near the Γ point. For both $R\bar{3}m$-$YCeH_{20}$ and $R\bar{3}m$-$LaCeH_{20}$, band inversion around the Γ point near E_F is observed, attributed primarily to H 1s and Ce 4f orbitals (refer Figs. S8 and S9 in Supplementary Material).

The E_F eDOS (N_{E_F}) for the aforementioned five phases are 1.72, 1.39, 1.10, 1.34, and 1.26 states/eV/f.u., respectively. The disparity in these N_{E_F} values mainly stems from the varying contributions of H and Ce atoms to N_{E_F}. As the hydrogen content rises, the contribution of Ce atoms at E_F diminishes, while that of H exhibits a converse trend. Nevertheless, the Ce decline outweighs the H increment, leading to a consistent total DOS decrease with an increasing H content.

As per Belli et al.'s contention [193], a robust positive correlation persists between the H contribution in the total DOS at E_F (H_{DOS}) and hydrides' superconductivity. The H_{DOS} values for the five phases are 9.5%, 34.4%, 38.2%, 11.2%, and 34.7%, respectively. This suggests that despite a lower total DOS, H-rich phases exhibit higher H-derived DOS

at E_F, implying the potential for high-T_c in H-rich phases to a certain degree [193].

The orbital-weighted electronic band structures of $P\bar{6}m2$-$YCeH_{18}$, $R\bar{3}m$-$YCeH_{20}$, and $R\bar{3}m$-$LaCeH_{20}$ (shown in Fig. S9) reveal that the bands around E_F are primarily the result of hybridization between the Ce 4f and H 1s orbitals, predicted using the GGA-PBE functional. This invites the question of the strength of SOC interaction and correlated effects associated with Ce 4f orbitals in these compounds. To address this, we further scrutinized the electronic band structures with SOC interaction, correction of the on-site Coulomb interaction of Ce 4f orbitals, and their combination (refer to Fig. S10 in the Supplementary Material). Our findings indicate that both the SOC interaction and the on-site Coulomb interaction correction have a negligible impact on bands around E_F.

As the superconducting transition temperature is heavily influenced by electronic properties at E_F, our chosen computational methodology should offer reasonable predictions regarding the superconducting properties of Ce-containing ternary hydrides. This approach, which overlooks SOC interaction and correlated effects, has also been used in previous theoretical studies [4, 116] on the electron-phonon coupling of binary CeH_x. However, the combination of the DFT+U method and the density-functional perturbation theory approach in the QE code's latest version (v7.1) does not support electron-phonon interaction calculations. For these reasons, our superconductivity calculations did not account for SOC interaction and the strongly-correlated effect.

The mode-resolved EPC constant $\lambda_{q\nu}$, atom-projected PHDOS, and EPC spectra for $P4/mmm$-$YCeH_8$, $P\bar{6}m2$-$YCeH_{18}$, $R\bar{3}m$-$YCeH_{20}$, $P4/mmm$-$LaCeH_8$, and $R\bar{3}m$-$LaCeH_{20}$ under high pressures are shown in Fig. 6.3 and Fig. S12 in the supplementary material. In these five phases, hydrogen atoms dominate the phonons with frequencies over 10 THz, making up more than 70% of the total. Phonons with frequencies below 10 THz are mostly attributed to La, Ce, and Y atoms.

Due to the differing atomic masses of Y, La, and Ce, $YCeH_x$'s phonon spectrum has a slightly wider low-frequency range than $LaCeH_x$. The EPC constants of $YCeH_8$, $YCeH_{18}$, $YCeH_{20}$, $LaCeH_8$, and $LaCeH_{20}$ at respective pressures are 0.41, 2.51, 1.02, 0.35, and 0.99.

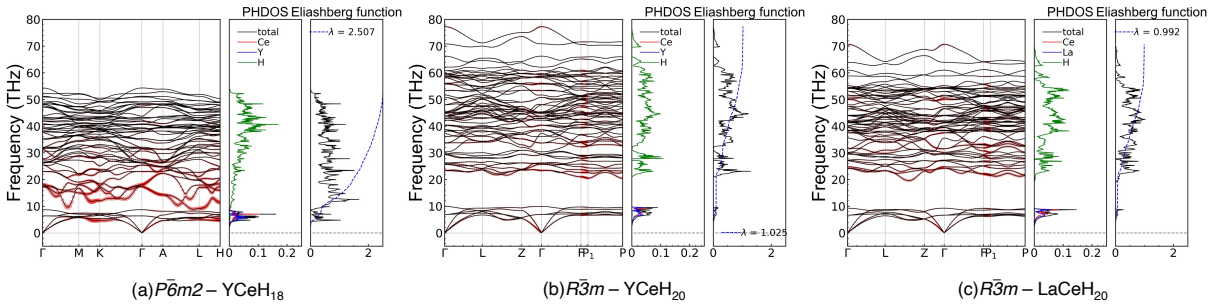

Figure 6.3: The phonon spectra with a projection of mode-resolved EPC constant $\lambda_{q\nu}$ (red circle), atom-projected phonon density of states (PHDOS), and Eliashberg function of (a) $P\bar{6}m2$-$YCeH_{18}$ at 150 GPa, (b) $R\bar{3}m$-$YCeH_{20}$ at 300 GPa, and (c) $R\bar{3}m$-$LaCeH_{20}$ at 250 GPa. The mode-revolved EPC constant $\lambda_{q\nu}$ is defined as $\lambda_{q\nu} = \frac{\gamma_{q\nu}}{\pi\hbar N(E_F)\omega_{q\nu}^2}$, where $\gamma_{q\nu}$ is phonon linewidth, $N(E_F)$ is the DOS at the Fermi level, and $\omega_{q\nu}$ is the mode-resolve phonon frequency.

$YCeH_{18}$'s EPC constant is remarkably high compared to the other four phases.

Analysis of the mode-resolved EPC constant $\lambda_{q\nu}$ reveals that the largest contribution to $YCeH_{18}$'s total EPC constant comes from the optical phonon branch within the 10 to 20 THz frequency range, contributing approximately 0.64 (or 25.7% of the total EPC constant). The rare-earth-atom associated vibrational modes of $YCeH_{18}$, with frequencies under 10 THz, also moderately contribute to the total EPC constant, as compared to the other four phases. In contrast, rare-earth atoms' contribution to $YCeH_{20}$'s EPC, which has a higher H content, is only 0.09.

Increasing pressure from 150 GPa to 300 GPa results in the hardening of phonons dominated by the H-atom-associated vibration in $YCeH_{18}$, as seen in Fig. 6.3(a) and Fig. S11(c). The pressure increase leads to a decrease in $YCeH_{18}$'s EPC constant, such that at 300 GPa, it is very close to that of $LaCeH_{20}$ at the same pressure. The EPC constants of $ACeH_8$ (A = Y and La) are noticeably smaller than those of $ACeH_{18}$ and $ACeH_{20}$ due to the lower maximum phonon frequencies and H-derived electronic density of states in the former compared to the latter.

This suggests that once hydrogen atoms in metal hydrides provide both a sufficient electron density of states at E_F and a sufficient phonon density of states in the high-frequency region, a strong EPC strength can be achieved.

Utilizing the Allen-Dynes-modified McMillan formula [71] with a common value of the Coulomb pseudopotential μ^* (we use $\mu^* = 0.1$), we predict the T_c values of $P4/mmm$-$YCeH_8$, $P\bar{6}m2$-$YCeH_{18}$, $R\bar{3}m$-$YCeH_{20}$, $P4/mmm$-$LaCeH_8$, and $P4/mmm$-$LaCeH_8$ at respective pressures to be 4.8, 173.8, 122.1, 1.8, and 116.1 K.

Three recent high-pressure experiments [183, 194, 195] investigating the La-Ce-H system have been reported. Both Chen *et al.* [183] and Bi *et al.* [194] applied pressures under 130 GPa, finding a T_c of around 180 K. Intriguingly, despite using different initial material ratios for synthesis, the final results from these two groups [183, 194] were highly similar, hinting at a common high-temperature superconducting phase.

Our calculations indicate that the thermodynamically stable phase at this pressure (130 GPa) is $LaCeH_{18}$. We don't discuss this phase in detail due to the anharmonic approximation effects likely involved in its stabilization, which are beyond the scope of this work. Huang *et al.* [195] conducted measurements on La-Ce-H in the pressure range of 140-160 GPa, where we note that $LaCeH_{20}$ can stabilize.

Another recent high-pressure experimental study [196] focused on the Y-Ce-H system, reporting T_c values between 97-140 K. This is in good agreement with the predicted T_c value of $YCeH_{18}$ by either the McM or AD formula.

In this respect, these experimental results lend considerable support to our theoretical predictions. To sum up, the high-pressure phases of $LaCeH_{18}$, $LaCeH_{20}$, and $YCeH_{18}$ revealed computationally in this study have all been confirmed by recent high-pressure experiments, with $LaCeH_{20}$ and $YCeH_{18}$ being theoretically predicted for the first time.

6.4.3 Discussion

As outlined above, $ACeH_8$, $YCeH_{18}$ and $ACeH_{20}$ (A = La and Y) conform to the space groups of $P4/mmm$, $P\bar{6}m2$ and $R\bar{3}m$, with rare earth atoms enclosed within the H_{18}, H_{29} and H_{32} cages, respectively. We utilize COHP and ICOHP analyses to delve further into the chemical bonding within these structures. The key bond lengths of select H-H, Ce-H, and A-H (A - La, Y) atom pairs, along with their corresponding ICOHP values indicative

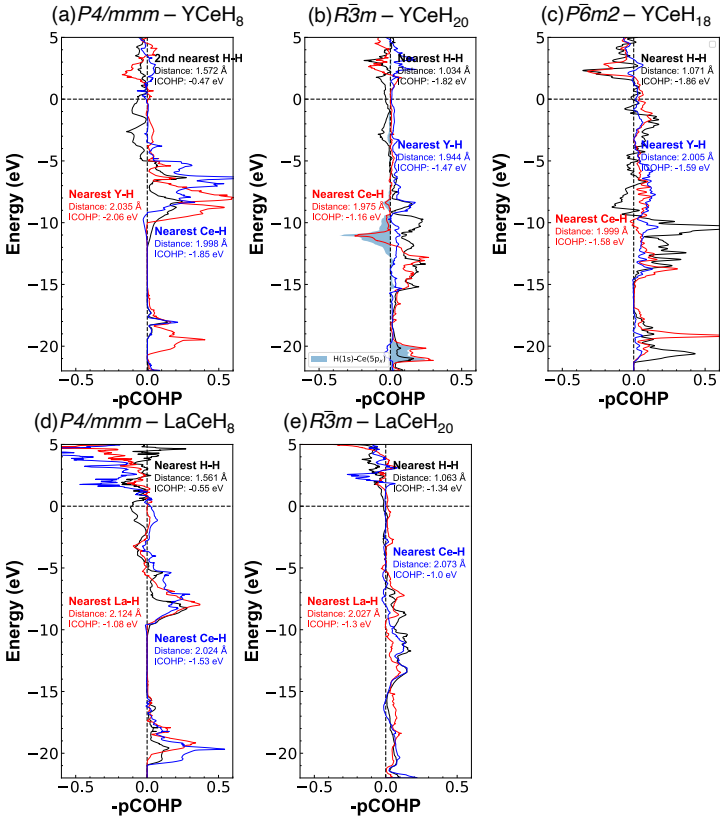

Figure 6.4: The Crystal Orbital Hamilton Population (COHP) of some representative atom pairs (H-H, Y-H, La-H, and Ce-H) in $P4/mmm$-YCeH8, $P\bar{6}m2$-$YCeH_{18}$, $R\bar{3}m$-$YCeH_{20}$, $P4/mmm$-$LaCeH_8$, and $R\bar{3}$m-$LaCeH_{20}$ at the pressure of 100, 150, 300, 100, and 250 GPa, respectively.

of bonding strength, are displayed in Figure 6.4.

COHP analysis conventionally suggests positive and negative values of −COHP represent bonding and anti-bonding traits, respectively. Referring to Fig. 6.2, the H_{18} cage in $YCeH_8$ appears to be comprised of eight quadrangles and four hexagons. Therefore, H-H bonds in the H_{18} cages can be roughly categorized into three groups: i) H-H bonds connecting two adjacent quadrangles, ii) H-H bonds linking two neighboring hexagons, and iii) H-H bonds spanning a quadrangle and a hexagon.

H-H bond lengths within the first and second groups are denoted as D1 and D2, as indicated in Figs. S14(a) and S14(d) in the SM. These distinct bond lengths, D1 and D2, in $YCeH_8$ and $LaCeH_8$ at 100 GPa descend in the following order: D2($LaCeH_8$) > D1($YCeH_8$) $\gtrsim$ D1($LaCeH_8$) > D2($YCeH_8$). Although H-H bonds with D1 in $YCeH_8$ and $LaCeH_8$ share comparable bond lengths, the projected COHPs for them, as shown in Figs. 6.4(a) and 6.4(c), highlight that this H-H bond in $LaCeH_8$ manifests a stronger bonding interaction than in $YCeH_8$. This is attributed to fewer anti-bonding states appearing just below E_F and a slightly greater absolute ICOHP value in $LaCeH_8$. Yet, this H-H bond's interaction appears significantly weaker than that of the A-H and Ce-H bonds, as suggested by their respective ICOHP values.

The H-H bonds in $YCeH_{18}$ and $ACeH_{20}$, which have higher H content, are significantly contracted due to the higher pressure required for stabilizing $YCeH_{18}$ and $ACeH_{20}$. The ICOHP values of the H-H bonds in $YCeH_{18}$ and $ACeH_{20}$ are almost triple those in $ACeH_8$, and far fewer (and even no) anti-bonding states occur below E_F for the H-H bonds in $YCeH_{20}$ (and $LaCeH_{20}$). As we move from the H_{18} cages in $ACeH_8$ to the H_{29} cages in $YCeH_{18}$ and H_{32} cages in $ACeH_{20}$, the cage size expands and the number of quadrangles (hexagons) decreases (increases) due to the incorporation of more H atoms. These findings imply that the H-H bonds exhibiting anti-bonding states in $ACeH_8$ could be greatly stabilized in $YCeH_{18}$ and $ACeH_{20}$, as they seem primed for hybridization with the additional incorporated H atoms.

Moreover, $YCeH_{20}$ exhibits noticeable anti-bonding states around -11 eV for the Ce-H atom pair, as discerned from Fig. 6.4(c). This is primarily attributed to the hybridization

between the H-1s and Ce-5p$_x$ orbitals, suggesting the semi-core states (such as 5p orbitals) of Ce in YCeH$_{20}$ under high pressure may contribute to the Ce-H bonding.

The crystal orbital bond index (COBI) serves as a measure of covalent bond strength in covalently bonded solid materials. In the cage structures of ACeH$_8$, YCeH$_{18}$, and ACeH$_{20}$, the integrated-COBI (ICOBI) values for the H-H bonds are less than 0.15, which points to very weak bonding interactions between H-H pairs. Despite increasing with pressure, the overall trend in ICOBI for H-H bonds shows a change less than 0.02, suggesting that pressure has a limited effect on H-H bonding. A similar pattern is also observed in the ICOHP analysis. Notably, the H-H bond strength in $R\bar{3}m$-YCeH$_{20}$ within the pressure range of 300-400 GPa is marginally stronger than that in $R\bar{3}m$-LaCeH$_{20}$, as per both the electron localization function (ELF) and ICOHP analyses, even though the corresponding ICOBI values in these two structures are quite similar and display a negligible pressure dependence.

The five superconducting compounds covered in this discussion, which exhibit both thermodynamic and dynamic stability, primarily belong to the ACeH$_8$, ACeH$_{18}$, and ACeH$_{20}$ types. Earlier reported compounds like ScCaH$_8$ [172] and YMgH$_8$ [197] also share the same structure as ACeH$_8$. In the case of the ACeH$_8$ type, it contains three distinct H-H bonds as previously noted. Here, the D1 type decreases with increasing pressure, whereas D2 shows a weaker pressure dependence. Furthermore, the H-H bond strength can also be interpreted through the ELF.

Belli *et al.* [193] recently proposed a strong correlation between the T_c value of superconducting hydrides and weak covalent H-H bonds. They introduced a possible networking value ϕ, representing the highest ELF value that forms an isosurface spanning the entire crystal in all three Cartesian directions. This serves to elucidate the nature of H-H bonds in hydrides. They mentioned the challenge in precisely defining the ϕ value. From our examination of the radial distribution function of H atoms in YCeH$_x$ and LaCeH$_x$ phases as a function of pressure (Fig. S14 in the SM), a prominent peak is observed within the radial range of 3 Å, representing the primary distribution of H-H bond lengths. Thus, we determine the ϕ value by averaging all ELF values at the valley points of line plots of

ELF along different H-H bonds corresponding to this peak. Using the model proposed by Belli *et al.* [193], the T_c of a metal hydride can be estimated with a precision within 60 K using the following equation:

$$T_c = 750\phi H_f \sqrt[1/3]{H_{DOS}} - 85, \tag{6.9}$$

In the equation, H_f signifies the hydrogen fraction while H_{DOS} represents the hydrogen fraction of the total DOS at E_F. As highlighted in Table 6.1, the networking values (ϕ) of our analyzed phases are all below 0.5 and are closely aligned. As a result, T_c values derived from Eq. (6.9) are mainly influenced by the H_{DOS} contribution. We also found that T_c values calculated via Eq. (6.9) show slight deviations from those predicted by the AD formula given by Eq. (6.3).

Upon studying $YCeH_{18}$ at 150 and 300 GPa, we observed that increasing pressure results in a reduction in H-H distance, an upward trend in the overall ϕ value, and an enhanced contribution of H to the density of states at E_F. Hence, the ELF-based Eq. (6.9) suggests that T_c for $YCeH_{18}$ escalates as pressure increases, a trend contrasting with the prediction from the AD formula. This discrepancy implies a potential limitation of Eq. (6.9) in predicting pressure-dependent T_c values.

Observing Peng *et al.*'s [4] predictions for all binary rare-earth metal hydrides reveals a trend where elements with a higher number of f electrons seem to suppress the T_c value. Nevertheless, the dataset used by Belli *et al.* [193] to construct Eq. (6.9) included only a limited number of f-electron-containing cases (specifically, CeH_9 and PrH_9).

Therefore, while T_c shows a certain correlation with ϕ and H_{DOS} values, the application of Eq. (6.9) to pressure-dependent and f-electron-containing systems requires further refinement.

Table 6.1: Superconducting transition temperature (T_c) predicted by the original McMillan formula (abbreviated to McM), the Allen-Dynes-modified McMillan (McM) formula (abbreviated to AD), and the model (i.e., Eq. (6.9)) proposed by Belli *et al.*, (abbreviated to ELF) for A-Ce-H (A = Y and La) at some selected pressures. Accordingly, the values of some key parameters contained in these formulas and model are also listed.

Phase	Space group	P (GPa)	N_{atom}	d_{H-H} Å	ϕ	H_{DOS}	λ	ω_{log} (K)	T_c (ELF) (K)	T_c (McM) (K)	T_c (AD) (K)
$YCeH_8$	$P4/mmm$	100	20	1.52	0.40	9.5%	0.41	987.5	24.5	4.7	4.8
$YCeH_{18}$	$P\bar{6}m2$	150	22	1.07	0.43	34.4%	2.51	812.2	118.3	133.8	173.8
$YCeH_{18}$	$P\bar{6}m2$	300	22	1.05	0.46	39.2%	0.97	1547.7	142.2	103	110
$YCeH_{20}$	$R\bar{3}m$	300	66	1.05	0.45	38.2%	1.03	1595.2	137.6	114.2	122.1
$LaCeH_8$	$P4/mmm$	100	20	1.56	0.38	11.2%	0.35	975.8	24.9	1.73	1.76
$LaCeH_{20}$	$R\bar{3}m$	250	66	1.06	0.48	34.7%	1.00	1566.9	145.0	109.1	116.1

6.5 Conclusion

To recap, we utilized an evolutionary algorithm coupled with first-principles computations to explore the ternary phase diagrams of $YCeH_x$ and $LaCeH_x$ systems within the 100-400 GPa pressure spectrum. The clathrate structure encompassed by H_{18}, H_{29}, and H_{32} remained thermodynamically stable within the examined pressure domain. These caged configurations correspond to the $YCeH_8$, $YCeH_{18}$, $YCeH_{20}$, $LaCeH_8$, $LaCeH_{18}$, $LaCeH_{20}$ phases. Yet, $LaCeH_{18}$ failed to demonstrate dynamic stability under the harmonic approximation.

We proceeded to probe the superconductivity of $YCeH_8$, $YCeH_{18}$, $YCeH_{20}$, $LaCeH_8$, and $LaCeH_{20}$. The findings highlight the potential of these four phases to facilitate high-temperature superconductivity, with $P\bar{6}m2$-$YCeH_{18}$ reaching the highest, at 173 K at 150GPa.

Furthermore, as per structural aspects, phases like $P4/mmm$-$YCeH_8$, $P4/mmm$-$LaCeH_8$, $P\bar{6}m2$-$YCeH_{18}$, and $P4/mmm$-$YCeH_{20}$ can be derived through elemental substitution in binary superconducting hydrides. This suggests that the discovery of new superconducting hydrides can be initiated by the amalgamation of binary superconducting hydrides. The combination of two binary superconducting hydrides with similar characteristics might give rise to a unique stable ternary hydride.

Chapter 7

Conclusion and Future Works

7.0.1 Conclusion

In this thesis, we delved into the crystal structures, stability, and superconductivity of diverse ternary hydrides utilizing evolutionary algorithms coupled with first-principles computations. Here are the principal findings:

1. We scrutinized the crystal structures of $(LaH_6)(YH_6)_y$ compounds as potential high-T_c ternary hydrides. While the earlier reported $Pm\bar{3}m$ structure showed instability, we unearthed stable formations such as $Cmmm$-$LaYH_{12}$, $R\bar{3}c$-$LaYH_{12}$, $Cmmm$-LaY_3H_{24}, and $R\bar{3}$-LaY_3H_{24}. The $Cmmm$ clathrate configurations demonstrated a $T_c \sim 130$ K at roughly $P = 200$ GPa.

2. We carried out a comprehensive examination of the stability and superconductivity of the ternary hydride $YMgH_x$ under high pressures. Predictions indicated seven stable and two metastable phases, with $YMgH_x$ forming clathrate structures consisting of H_{14}, H_{18}, and H_{24} cages. Our T_c estimations suggested high-T_c superconductivity for all the $YMgH_x$ clathrate formations, with the T_c value rising with the increment of H content x. The stable $Cmmm$-$YMgH_{12}$ and metastable $Fd\bar{3}m$-$YMgH_{12}$ sodalite configurations displayed T_c values of 153 K at 250 GPa and 190 K at 200 GPa, respectively.

3. Utilizing the USPEX code's evolutionary algorithm and first-principles computations, we navigated the ternary phase diagram of the Mg-Sc-H system under a pressure

range of 100 to 200 GPa. Our computations suggest Sc-rich ternary Mg-Sc-H compounds are likely stable around 100 GPa, while Mg-rich ones are more probable above 180 GPa. We predicted the superconductivity for the ternary Mg-Sc-H hydrides with a hydrogen/metal ratio around three, with $R\bar{3}m$-$MgScH_6$ displaying a T_c around 41 K at 100 GPa.

4. We probed the ternary phase diagrams of $YCeH_x$ and $LaCeH_x$ systems within a pressure range of 100-400 GPa. The clathrate structure surrounded by H_{18}, H_{29}, and H_{32} maintained thermodynamic stability within this pressure domain. Our observations indicate all four formations, namely $P4/mmm$-$YCeH_8$, $P4/mmm$-$LaCeH_8$, $P\bar{6}m2$-$YCeH_{18}$, and $P4/mmm$-$YCeH_{20}$, can facilitate high-temperature superconductivity, with $P\bar{6}m2$-$YCeH_{18}$ reaching the highest T_c of 173 K at 150 GPa.

In summary, our study sheds light on the structures and superconducting characteristics of ternary hydrides, creating a path for novel superconducting material development with potential applications in areas like energy storage, transportation, and electronics. Furthermore, our findings suggest that the fusion of binary superconducting hydrides exhibiting similar traits might result in the creation of novel, stable ternary hydrides, thereby broadening the scope of prospective high-T_c superconducting compounds. To substantiate our predictions and explore other ternary hydride systems with potential for high-T_c superconductivity, further experimental and theoretical investigations are warranted.

7.0.2 Future Works

For the advancement of our understanding of superconducting hydrides and the discovery of new materials with unique properties, several potential directions for future research have been identified:

1. General rules governing superconductivity in hydride materials: A comprehensive investigation of the underlying principles governing superconductivity in various hydride systems could lead to the development of guidelines for designing and predicting new high-T_c superconducting hydrides.

2. Determining the nature of ternary clathrate hydrides: A thorough examination of ternary cage-like hydrides is required to establish whether they should be classified as alloys or compounds, which would help clarify their structural and electronic properties.

3. Machine learning for discovering thermodynamically stable hydrogen-rich compounds at low pressures: Employing machine learning techniques to search for new hydrogen-rich compounds with thermodynamic stability at low pressures can potentially lead to the discovery of novel materials with practical applications and enhanced properties.

4. Machine learning for finding dynamically stable room-temperature superconducting hydrides: The application of machine learning methods to identify dynamically stable hydrides capable of exhibiting room-temperature superconductivity could significantly advance the field of superconductivity research and pave the way for groundbreaking applications in various industries.

Bibliography

[1] José A. Flores-Livas, Lilia Boeri, Antonio Sanna, Gianni Profeta, Ryotaro Arita, and Mikhail Eremets. A perspective on conventional high-temperature superconductors at high pressure: Methods and materials. *Phys. Rep.*, 856:1–78, apr 2020.

[2] A. P. Drozdov, M. I. Eremets, I. A. Troyan, V. Ksenofontov, and S. I. Shylin. Conventional superconductivity at 203 kelvin at high pressures in the sulfur hydride system. *Nature*, 525(7567):73–76, aug 2015.

[3] Defang Duan, Yunxian Liu, Fubo Tian, Da Li, Xiaoli Huang, Zhonglong Zhao, Hongyu Yu, Bingbing Liu, Wenjing Tian, and Tian Cui. Pressure-induced metallization of dense (h2s)2h2 with high-tc superconductivity. *Sci. Rep.*, 4(1):6968, nov 2014.

[4] Feng Peng, Ying Sun, Chris J. Pickard, Richard J. Needs, Qiang Wu, and Yanming Ma. Hydrogen clathrate structures in rare earth hydrides at high pressures: Possible route to room-temperature superconductivity. *Phys. Rev. Lett.*, 119(10):107001, sep 2017.

[5] A. P. Drozdov, P. P. Kong, V. S. Minkov, S. P. Besedin, M. A. Kuzovnikov, S. Mozaffari, L. Balicas, F. F. Balakirev, D. E. Graf, V. B. Prakapenka, E. Greenberg, D. A. Knyazev, M. Tkacz, and M. I. Eremets. Superconductivity at 250 k in lanthanum hydride under high pressures. *Nature*, 569(7757):528–531, may 2019.

[6] Ion Errea, Francesco Belli, Lorenzo Monacelli, Antonio Sanna, Takashi Koretsune, Terumasa Tadano, Raffaello Bianco, Matteo Calandra, Ryotaro Arita, Francesco

Mauri, and José A. Flores-Livas. Quantum crystal structure in the 250-kelvin superconducting lanthanum hydride. *Nature*, 578(7793):66–69, feb 2020.

[7] Fengyuan Xuan, Jeng-Da Chai, and Haibin Su. Local density approximation for the short-range exchange free energy functional. *ACS Omega*, 4(4):7675–7683, apr 2019.

[8] Koichi Momma and Fujio Izumi. Vesta: a three-dimensional visualization system for electronic and structural analysis. *J. Appl. Crystallogr.*, 41(3):653–658, may 2008.

[9] Chris J. Pickard and Richard J. Needs. Structure of phase III of solid hydrogen. *Nat. Phys.*, 3(7):473–476, may 2007.

[10] S. Dawson, C. Jackson, L. H. Orr, L. Reina, and D. Wackeroth. Associated higgs boson production with top quarks at the CERN large hadron collider: NLO QCD corrections. *Phys. Rev. D*, 68(3):034022, aug 2003.

[11] H Kamerlingh Onnes. The superconductivity of mercury. *Comm. Phys. Lab. Univ. Leiden*, 122:124, 1911.

[12] J. G. Bednorz and K. A. Moller. Possible highT c superconductivity in the ba?la?cu?o system. *Zeitschrift for Physik B Condensed Matter*, 64(2):189–193, jun 1986.

[13] N. W. Ashcroft. Hydrogen dominant metallic alloys: High temperature superconductors? *Phys. Rev. Lett.*, 92(18):187002, may 2004.

[14] A. Jayaraman. Diamond anvil cell and high-pressure physical investigations. *Rev. Mod. Phys.*, 55(1):65–108, jan 1983.

[15] William A. Bassett. Diamond anvil cell, 50th birthday. *High Pressure Res.*, 29(2):163–186, may 2009.

[16] Alexander F. Goncharov, Vitali B. Prakapenka, Viktor V. Struzhkin, Innokenty Kantor, Mark L. Rivers, and D. Allen Dalton. X-ray diffraction in the pulsed laser heated diamond anvil cell. *Rev. Sci. Instrum.*, 81(11):113902, nov 2010.

[17] Maddury Somayazulu, Muhtar Ahart, Ajay K. Mishra, Zachary M. Geballe, Maria Baldini, Yue Meng, Viktor V. Struzhkin, and Russell J. Hemley. Evidence for superconductivity above 260 k in lanthanum superhydride at megabar pressures. *Phys. Rev. Lett.*, 122(2):027001, jan 2019.

[18] Ion Errea, Matteo Calandra, Chris J. Pickard, Joseph Nelson, Richard J. Needs, Yinwei Li, Hanyu Liu, Yunwei Zhang, Yanming Ma, and Francesco Mauri. High-pressure hydrogen sulfide from first principles: A strongly anharmonic phonon-mediated superconductor. *Phys. Rev. Lett.*, 114(15):157004, apr 2015.

[19] Paul F. McMillan. Chemistry at high pressure. *Chem. Soc. Rev.*, 35(10):855, 2006.

[20] Zhiwen Li, Xin He, Changling Zhang, Xiancheng Wang, Sijia Zhang, Yating Jia, Shaomin Feng, Ke Lu, Jianfa Zhao, Jun Zhang, Baosen Min, Youwen Long, Richeng Yu, Luhong Wang, Meiyan Ye, Zhanshuo Zhang, Vitali Prakapenka, Stella Chariton, Paul A. Ginsberg, Jay Bass, Shuhua Yuan, Haozhe Liu, and Changqing Jin. Superconductivity above 200 k discovered in superhydrides of calcium. *Nat. Commun.*, 13(1):2863, may 2022.

[21] Panpan Kong, Vasily S. Minkov, Mikhail A. Kuzovnikov, Alexander P. Drozdov, Stanislav P. Besedin, Shirin Mozaffari, Luis Balicas, Fedor Fedorovich Balakirev, Vitali B. Prakapenka, Stella Chariton, Dmitry A. Knyazev, Eran Greenberg, and Mikhail I. Eremets. Superconductivity up to 243 k in the yttrium-hydrogen system under high pressure. *Nat. Commun.*, 12(1):5075, aug 2021.

[22] Ivan A. Troyan, Dmitrii V. Semenok, Alexander G. Kvashnin, Andrey V. Sadakov, Oleg A. Sobolevskiy, Vladimir M. Pudalov, Anna G. Ivanova, Vitali B. Prakapenka, Eran Greenberg, Alexander G. Gavriliuk, Igor S. Lyubutin, Viktor V. Struzhkin,

Aitor Bergara, Ion Errea, Raffaello Bianco, Matteo Calandra, Francesco Mauri, Lorenzo Monacelli, Ryosuke Akashi, and Artem R. Oganov. Anomalous high-temperature superconductivity in yh6. *Adv. Mater.*, 33(15):2006832, mar 2021.

[23] Bin Li, Zilong Miao, Lei Ti, Shengli Liu, Jie Chen, Zhixiang Shi, and Eugene Gregoryanz. Predicted high-temperature superconductivity in cerium hydrides at high pressures. *J. Appl. Phys.*, 126(23):235901, dec 2019.

[24] Y. Nakamori, M. Matsuo, K. Yamada, T. Tsutaoka, and S. Orimo. Effects of microwave irradiation on metal hydrides and complex hydrides. *J. Alloys Compd.*, 446-447:698–702, oct 2007.

[25] Di Zhou, Dmitrii V. Semenok, Hui Xie, Xiaoli Huang, Defang Duan, Alex Aperis, Peter M. Oppeneer, Michele Galasso, Alexey I. Kartsev, Alexander G. Kvashnin, Artem R. Oganov, and Tian Cui. High-pressure synthesis of magnetic neodymium polyhydrides. *J. Am. Chem. Soc.*, 142(6):2803–2811, jan 2020.

[26] Miriam Peña-Alvarez, Jack Binns, Andreas Hermann, Liam C. Kelsall, Philip Dalladay-Simpson, Eugene Gregoryanz, and Ross T. Howie. Praseodymium polyhydrides synthesized at high temperatures and pressures. *Phys. Rev. B*, 100(18):184109, nov 2019.

[27] Liang Ma, Mi Zhou, Yingying Wang, Saori Kawaguchi, Yasuo Ohishi, Feng Peng, Hanyu Liu, Guangtao Liu, Hongbo Wang, and Yanming Ma. Experimental clathrate superhydrides euh6 and euh9 at extreme pressure conditions. *Physical Review Research*, 3(4):043107, nov 2021.

[28] Yoshichika Ōnuki, Rikio Settai, Kiyohiro Sugiyama, Tetsuya Takeuchi, Tatsuo C. Kobayashi, Yoshinori Haga, and Etsuji Yamamoto. Recent advances in the magnetism and superconductivity of heavy fermion systems. *J. Phys. Soc. Jpn.*, 73(4):769–787, apr 2004.

[29] Dmitrii V. Semenok, Ivan A. Kruglov, Igor A. Savkin, Alexander G. Kvashnin, and Artem R. Oganov. On distribution of superconductivity in metal hydrides. *Curr. Opin. Solid State Mater. Sci.*, 24(2):100808, apr 2020.

[30] V. S. Minkov, S. L. Bud'ko, F. F. Balakirev, V. B. Prakapenka, S. Chariton, R. J. Husband, H. P. Liermann, and M. I. Eremets. Magnetic field screening in hydrogen-rich high-temperature superconductors. *Nat. Commun.*, 13(1):3194, jun 2022.

[31] Michael J. Hutcheon, Alice M. Shipley, and Richard J. Needs. Predicting novel superconducting hydrides using machine learning approaches. *Phys. Rev. B*, 101(14):144505, apr 2020.

[32] S. R. Xie, Y. Quan, A. C. Hire, B. Deng, J. M. DeStefano, I. Salinas, U. S. Shah, L. Fanfarillo, J. Lim, J. Kim, G. R. Stewart, J. J. Hamlin, P. J. Hirschfeld, and R. G. Hennig. Machine learning of superconducting critical temperature from eliashberg theory. *npj Comput. Mater.*, 8(1):14, jan 2022.

[33] Xiaowei Liang, Aitor Bergara, Xudong Wei, Xiaoxu Song, Linyan Wang, Rongxin Sun, Hanyu Liu, Russell J. Hemley, Lin Wang, Guoying Gao, and Yongjun Tian. Prediction of high- tc superconductivity in ternary lanthanum borohydrides. *Phys. Rev. B*, 104(13):134501, oct 2021.

[34] Ying Sun, Jian Lv, Yu Xie, Hanyu Liu, and Yanming Ma. Route to a superconducting phase above room temperature in electron-doped hydride compounds under high pressure. *Phys. Rev. Lett.*, 123(9):097001, aug 2019.

[35] W. Kohn, A. D. Becke, and R. G. Parr. Density functional theory of electronic structure. *The Journal of Physical Chemistry*, 100(31):12974–12980, jan 1996.

[36] Colin W. Glass, Artem R. Oganov, and Nikolaus Hansen. USPEX—evolutionary crystal structure prediction. *Comput. Phys. Commun.*, 175(11-12):713–720, dec 2006.

[37] Aron J. Cohen, Paula Mori-Sánchez, and Weitao Yang. Challenges for density functional theory. *Chem. Rev.*, 112(1):289–320, dec 2011.

[38] P. Hohenberg and W. Kohn. Inhomogeneous electron gas. *Phys. Rev.*, 136(3B):B864–B871, nov 1964.

[39] John P. Perdew, J. A. Chevary, S. H. Vosko, Koblar A. Jackson, Mark R. Pederson, D. J. Singh, and Carlos Fiolhais. Atoms, molecules, solids, and surfaces: Applications of the generalized gradient approximation for exchange and correlation. *Phys. Rev. B*, 46(11):6671–6687, sep 1992.

[40] Stefano Baroni, Stefano de Gironcoli, Andrea Dal Corso, and Paolo Giannozzi. Phonons and related crystal properties from density-functional perturbation theory. *Rev. Mod. Phys.*, 73(2):515–562, jul 2001.

[41] W. Kohn and L. J. Sham. Self-consistent equations including exchange and correlation effects. *Phys. Rev.*, 140(4A):A1133–A1138, nov 1965.

[42] Miguel A.L. Marques, Micael J.T. Oliveira, and Tobias Burnus. Libxc: A library of exchange and correlation functionals for density functional theory. *Comput. Phys. Commun.*, 183(10):2272–2281, oct 2012.

[43] Axel D. Becke. A new mixing of hartree–fock and local density-functional theories. *The Journal of Chemical Physics*, 98(2):1372–1377, jan 1993.

[44] Tamar Stein, Leeor Kronik, and Roi Baer. Prediction of charge-transfer excitations in coumarin-based dyes using a range-separated functional tuned from first principles. *The Journal of Chemical Physics*, 131(24):244119, dec 2009.

[45] Yan Zhao, Benjamin J. Lynch, and Donald G. Truhlar. Doubly hybrid meta DFT: new multi-coefficient correlation and density functional methods for thermochemistry and thermochemical kinetics. *J. Phys. Chem. A*, 108(21):4786–4791, may 2004.

[46] Volker Bach, Elliott H. Lieb, and Jan Philip Solovej. Generalized hartree-fock theory and the hubbard model. *J. Stat. Phys.*, 76(1-2):3–89, jul 1994.

[47] J. P. Perdew, E. R. McMullen, and Alex Zunger. Density-functional theory of the correlation energy in atoms and ions: A simple analytic model and a challenge. *Phys. Rev. A*, 23(6):2785–2789, jun 1981.

[48] Paula Mori-Sánchez, Aron J. Cohen, and Weitao Yang. Many-electron self-interaction error in approximate density functionals. *The Journal of Chemical Physics*, 125(20):201102, nov 2006.

[49] A. Svane and O. Gunnarsson. Transition-metal oxides in the self-interaction–corrected density-functional formalism. *Phys. Rev. Lett.*, 65(9):1148–1151, aug 1990.

[50] D. M. Bylander and Leonard Kleinman. Good semiconductor band gaps with a modified local-density approximation. *Phys. Rev. B*, 41(11):7868–7871, apr 1990.

[51] Sarah A Tolba, Kareem M Gameel, Basant A Ali, Hossam A Almossalami, and Nageh K Allam. The dft+ u: Approaches, accuracy, and applications. *Density Functional Calculations-Recent Progresses of Theory and Application*, 1:5772, 2018.

[52] Matteo Cococcioni. The lda+ u approach: a simple hubbard correction for correlated ground states. *Correlated Electrons: From Models to Materials Modeling and Simulation*, 2, 2012.

[53] Burak Himmetoglu, Andrea Floris, Stefano de Gironcoli, and Matteo Cococcioni. Hubbard-corrected dft energy functionals: The lda+u description of correlated systems. *Int. J. Quantum Chem.*, 114(1):14–49, jul 2013.

[54] Vladimir I Anisimov, F Aryasetiawan, and A I Lichtenstein. First-principles calculations of the electronic structure and spectra of strongly correlated systems: thelda+ u method. *J. Phys.: Condens. Matter*, 9(4):767–808, jan 1997.

[55] S. L. Dudarev, G. A. Botton, S. Y. Savrasov, C. J. Humphreys, and A. P. Sutton. Electron-energy-loss spectra and the structural stability of nickel oxide: An lsda+u study. *Phys. Rev. B*, 57(3):1505–1509, jan 1998.

[56] Matteo Cococcioni and Stefano de Gironcoli. Linear response approach to the calculation of the effective interaction parameters in thelda+umethod. *Phys. Rev. B*, 71(3):035105, jan 2005.

[57] Joachim Paier, Connie J. Nelin, Paul S. Bagus, Agata Plucienik, Helmut Kuhlenbeck, and Hans-Joachim Freund. Electronic structure of reduced CeO2(111) surfaces interacting with hydrogen as revealed through electron energy loss spectroscopy in comparison with theoretical investigations. *J. Electron Spectrosc. Relat. Phenom.*, 257:147088, may 2022.

[58] Haiyan Lu and Li Huang. Unraveling the 4 f electronic structures of cerium monopnictides. *J. Phys.: Condens. Matter*, 32(48):485601, sep 2020.

[59] Soma Banik, A Arya, Azzedine Bendounan, M Maniraj, A Thamizhavel, I Vobornik, S K Dhar, and S K Deb. Estimate of the coulomb correlation energy in ceag2ge2from inverse photoemission and high resolution photoemission spectroscopy. *J. Phys.: Condens. Matter*, 26(33):335502, jul 2014.

[60] Huai-Jun Lin, Jia-Jun Tang, Qian Yu, Hui Wang, Liu-Zhang Ouyang, Yu-Jun Zhao, Jiang-Wen Liu, Wei-Hua Wang, and Min Zhu. Symbiotic CeH 2.73 /CeO 2 catalyst: A novel hydrogen pump. *Nano Energy*, 9:80–87, oct 2014.

[61] B.Y. Ao, X.L. Wang, P. Shi, P.H. Chen, X.Q. Ye, X.C. Lai, J.J. Ai, and T. Gao. Lattice contraction of cerium hydrides from first-principles lda + u calculations. *Int. J. Hydrogen Energy*, 37(6):5108–5113, mar 2012.

[62] T. S. Bush, C. R. A. Catlow, and P. D. Battle. Evolutionary programming techniques for predicting inorganic crystal structures. *J. Mater. Chem.*, 5(8):1269, 1995.

[63] Scott M. Woodley, Peter D. Battle, Julian D. Gale, and C Richard A. Catlow. The prediction of inorganic crystal structures using a genetic algorithm and energy minimisation. *Phys. Chem. Chem. Phys.*, 1(10):2535–2542, 1999.

[64] Yanchao Wang, Jian Lv, Li Zhu, and Yanming Ma. CALYPSO: A method for crystal structure prediction. *Comput. Phys. Commun.*, 183(10):2063–2070, oct 2012.

[65] David C. Lonie and Eva Zurek. XtalOpt: An open-source evolutionary algorithm for crystal structure prediction. *Comput. Phys. Commun.*, 182(2):372–387, feb 2011.

[66] V. L. Solozhenko, O. O. Kurakevych, and A. R. Oganov. On the hardness of a new boron phase, orthorhombic γ-b28. *J. Superhard Mater.*, 30(6):428–429, dec 2008.

[67] Brad A. Steele and Ivan I. Oleynik. Sodium pentazolate: A nitrogen rich high energy density material. *Chem. Phys. Lett.*, 643:21–26, jan 2016.

[68] Ye-Fei Li and Annabella Selloni. Mosaic texture and double c -axis periodicity of β-niooh: Insights from first-principles and genetic algorithm calculations. *The Journal of Physical Chemistry Letters*, 5(22):3981–3985, nov 2014.

[69] Atsushi Togo and Isao Tanaka. First principles phonon calculations in materials science. *Scr. Mater.*, 108:1–5, nov 2015.

[70] W. L. McMillan. Transition temperature of strong-coupled superconductors. *Phys. Rev.*, 167(2):331–344, mar 1968.

[71] P. B. Allen and R. C. Dynes. Transition temperature of strong-coupled superconductors reanalyzed. *Phys. Rev. B*, 12(3):905–922, aug 1975.

[72] Paolo Giannozzi, Stefano Baroni, Nicola Bonini, Matteo Calandra, Roberto Car, Carlo Cavazzoni, Davide Ceresoli, Guido L Chiarotti, Matteo Cococcioni, Ismaila Dabo, Andrea Dal Corso, Stefano de Gironcoli, Stefano Fabris, Guido Fratesi, Ralph Gebauer, Uwe Gerstmann, Christos Gougoussis, Anton Kokalj, Michele Lazzeri, Layla Martin-Samos, Nicola Marzari, Francesco Mauri, Riccardo Mazzarello, Stefano Paolini, Alfredo Pasquarello, Lorenzo Paulatto, Carlo Sbraccia, Sandro Scandolo, Gabriele Sclauzero, Ari P Seitsonen, Alexander Smogunov, Paolo Umari, and Renata M Wentzcovitch. QUANTUM ESPRESSO: a modular and open-source

software project for quantum simulations of materials. *J. Phys.: Condens. Matter*, 21(39):395502, sep 2009.

[73] G. Kresse and J. Furthmüller. Efficiency of ab-initio total energy calculations for metals and semiconductors using a plane-wave basis set. *Computational Materials Science*, 6(1):15–50, jul 1996.

[74] S. Poncé, E.R. Margine, C. Verdi, and F. Giustino. EPW: Electron–phonon coupling, transport and superconducting properties using maximally localized wannier functions. *Comput. Phys. Commun.*, 209:116–133, dec 2016.

[75] X. Gonze, B. Amadon, P.-M. Anglade, J.-M. Beuken, F. Bottin, P. Boulanger, F. Bruneval, D. Caliste, R. Caracas, M. Côté, T. Deutsch, L. Genovese, Ph. Ghosez, M. Giantomassi, S. Goedecker, D.R. Hamann, P. Hermet, F. Jollet, G. Jomard, S. Leroux, M. Mancini, S. Mazevet, M.J.T. Oliveira, G. Onida, Y. Pouillon, T. Rangel, G.-M. Rignanese, D. Sangalli, R. Shaltaf, M. Torrent, M.J. Verstraete, G. Zerah, and J.W. Zwanziger. ABINIT: First-principles approach to material and nanosystem properties. *Comput. Phys. Commun.*, 180(12):2582–2615, dec 2009.

[76] N. W. Ashcroft. Metallic hydrogen: A high-temperature superconductor? *Phys. Rev. Lett.*, 21(26):1748–1749, dec 1968.

[77] M. I. Eremets, I. A. Trojan, S. A. Medvedev, J. S. Tse, and Y. Yao. Superconductivity in hydrogen dominant materials: Silane. *Science*, 319(5869):1506–1509, mar 2008.

[78] D Szczesniak and T P Zemla. On the high-pressure superconducting phase in platinum hydride. *Supercond. Sci. Technol.*, 28(8):085018, jul 2015.

[79] Elliot Snider, Nathan Dasenbrock-Gammon, Raymond McBride, Xiaoyu Wang, Noah Meyers, Keith V. Lawler, Eva Zurek, Ashkan Salamat, and Ranga P. Dias. Synthesis of yttrium superhydride superconductor with a transition temperature

up to 262 k by catalytic hydrogenation at high pressures. *Phys. Rev. Lett.*, 126(11):117003, mar 2021.

[80] Christoph Heil, Simone di Cataldo, Giovanni B. Bachelet, and Lilia Boeri. Superconductivity in sodalite-like yttrium hydride clathrates. *Phys. Rev. B*, 99(22):220502, jun 2019.

[81] Elliot Snider, Nathan Dasenbrock-Gammon, Raymond McBride, Mathew Debessai, Hiranya Vindana, Kevin Vencatasamy, Keith V. Lawler, Ashkan Salamat, and Ranga P. Dias. RETRACTED ARTICLE: Room-temperature superconductivity in a carbonaceous sulfur hydride. *Nature*, 586(7829):373–377, oct 2020.

[82] Yanbin Ma, Defang Duan, Ziji Shao, Da Li, Liyuan Wang, Hongyu Yu, Fubo Tian, Hui Xie, Bingbing Liu, and Tian Cui. Prediction of superconducting ternary hydride mggeh6: from divergent high-pressure formation routes. *Phys. Chem. Chem. Phys.*, 19(40):27406–27412, 2017.

[83] Yanbin Ma, Defang Duan, Ziji Shao, Hongyu Yu, Hanyu Liu, Fubo Tian, Xiaoli Huang, Da Li, Bingbing Liu, and Tian Cui. Divergent synthesis routes and superconductivity of ternary hydridemgsih6at high pressure. *Phys. Rev. B*, 96(14):144518, oct 2017.

[84] Da Li, Yan Liu, Fu-Bo Tian, Shu-Li Wei, Zhao Liu, De-Fang Duan, Bing-Bing Liu, and Tian Cui. Pressure-induced superconducting ternary hydride h3sxe: A theoretical investigation. *Frontiers of Physics*, 13(5):137107, aug 2018.

[85] Xiaowei Liang, Aitor Bergara, Linyan Wang, Bin Wen, Zhisheng Zhao, Xiang-Feng Zhou, Julong He, Guoying Gao, and Yongjun Tian. Potential high- tc superconductivity in cayh12 under pressure. *Phys. Rev. B*, 99(10):100505, mar 2019.

[86] Martin Rahm, Roald Hoffmann, and N. W. Ashcroft. Ternary gold hydrides: Routes to stable and potentially superconducting compounds. *J. Am. Chem. Soc.*, 139(25):8740–8751, jun 2017.

[87] Xiaowei Liang, Shutao Zhao, Cancan Shao, Aitor Bergara, Hanyu Liu, Linyan Wang, Rongxin Sun, Yang Zhang, Yufei Gao, Zhisheng Zhao, Xiang-Feng Zhou, Julong He, Dongli Yu, Guoying Gao, and Yongjun Tian. First-principles study of crystal structures and superconductivity of ternary ysh6 and lash6 at high pressures. *Phys. Rev. B*, 100(18):184502, nov 2019.

[88] Yong Kai Wei, Liang Quan Jia, Yan Yan Fang, Long Jun Wang, Zhi Xiu Qian, Jiao Nan Yuan, Gurudeeban Selvaraj, Guang Fu Ji, and Dong Qing Wei. Formation and superconducting properties of predicted ternary hydride scyh6 under pressures. *Int. J. Quantum Chem.*, 121(4):PLACEHOLDER, sep 2020.

[89] Hui Xie, Defang Duan, Ziji Shao, Hao Song, Youchun Wang, Xuehui Xiao, Da Li, Fubo Tian, Bingbing Liu, and Tian Cui. High-temperature superconductivity in ternary clathrate ycah12 under high pressures. *J. Phys.: Condens. Matter*, 31(24):245404, apr 2019.

[90] Christian Kokail, Wolfgang von der Linden, and Lilia Boeri. Prediction of high- tc conventional superconductivity in the ternary lithium borohydride system. *Physical Review Materials*, 1(7):074803, dec 2017.

[91] Ziji Shao, Defang Duan, Yanbin Ma, Hongyu Yu, Hao Song, Hui Xie, Da Li, Fubo Tian, Bingbing Liu, and Tian Cui. Ternary superconducting cophosphorus hydrides stabilized via lithium. *npj Comput. Mater.*, 5(1):104, oct 2019.

[92] Peiyu Zhang, Ying Sun, Xue Li, Jian Lv, and Hanyu Liu. Structure and superconductivity in compressed li-si-h compounds: Density functional theory calculations. *Phys. Rev. B*, 102(18):184103, nov 2020.

[93] Jin Zhang, Jeffrey M. McMahon, Artem R. Oganov, Xinfeng Li, Xiao Dong, Huafeng Dong, and Shengnan Wang. High-temperature superconductivity in the ti-h system at high pressures. *Phys. Rev. B*, 101(13):134108, apr 2020.

[94] Xue Guo, Ru-Lin Wang, Hai-Liang Chen, Wen-Cai Lu, K.M. Ho, and C.Z. Wang. Stability and superconductivity of TiPHn (n = 1-8) under high pressure. *Phys. Lett. A*, 384(9):126189, mar 2020.

[95] Wenwen Cui, Tiange Bi, Jingming Shi, Yinwei Li, Hanyu Liu, Eva Zurek, and Russell J. Hemley. Route to high- tc superconductivity via ch4 -intercalated h3s hydride perovskites. *Phys. Rev. B*, 101(13):134504, apr 2020.

[96] Hai-Yan Lv, Si-Yuan Zhang, Meng-Hu Li, Yu-Long Hai, Ning Lu, Wen-Jie Li, and Guo-Hua Zhong. Metallization and superconductivity in methane doped by beryllium at low pressure. *Phys. Chem. Chem. Phys.*, 22(3):1069–1077, 2020.

[97] Yan Yan, Tiange Bi, Nisha Geng, Xiaoyu Wang, and Eva Zurek. A metastable cash3 phase composed of hs honeycomb sheets that is superconducting under pressure. *The Journal of Physical Chemistry Letters*, 11(22):9629–9636, oct 2020.

[98] Takaki Muramatsu, Wilson K. Wanene, Maddury Somayazulu, Eugene Vinitsky, Dhanesh Chandra, Timothy A. Strobel, Viktor V. Struzhkin, and Russell J. Hemley. Metallization and superconductivity in the hydrogen-rich ionic salt bareh9. *The Journal of Physical Chemistry C*, 119(32):18007–18013, aug 2015.

[99] Dezhong Meng, Masafumi Sakata, Katsuya Shimizu, Yuki Iijima, Hiroyuki Saitoh, Toyoto Sato, Shigeyuki Takagi, and Shin ichi Orimo. Superconductivity of the hydrogen-rich metal hydride li5moh11 under high pressure. *Phys. Rev. B*, 99(2):024508, jan 2019.

[100] Guoying Gao, Artem R. Oganov, Yanming Ma, Hui Wang, Peifang Li, Yinwei Li, Toshiaki Iitaka, and Guangtian Zou. Dissociation of methane under high pressure. *The Journal of Chemical Physics*, 133(14):144508, oct 2010.

[101] Binbin Liu, Wenwen Cui, Jingming Shi, Li Zhu, Ju Chen, Shuyi Lin, Ruiming Su, Jiayu Ma, Kang Yang, Meiling Xu, Jian Hao, Artur P. Durajski, Jingshan Qi,

Yanling Li, and Yinwei Li. Effect of covalent bonding on the superconducting critical temperature of the h-s-se system. *Phys. Rev. B*, 98(17):174101, nov 2018.

[102] P.-H. Chang, S. Silayi, D.A. Papaconstantopoulos, and M.J. Mehl. Pressure-induced high-temperature superconductivity in hypothetical h3x (x=as, se, br, sb, te and i) in the h3s structure with im3¯m symmetry. *J. Phys. Chem. Solids*, 139:109315, apr 2020.

[103] Akitaka Nakanishi, Takahiro Ishikawa, and Katsuya Shimizu. First-principles study on superconductivity of p- and cl-doped h3s. *J. Phys. Soc. Jpn.*, 87(12):124711, dec 2018.

[104] Wiwittawin Sukmas, Prutthipong Tsuppayakorn-aek, Udomsilp Pinsook, and Thiti Bovornratanaraks. Near-room-temperature superconductivity of mg/ca substituted metal hexahydride under pressure. *J. Alloys Compd.*, 849:156434, dec 2020.

[105] Takahiro Ishikawa, Takashi Miyake, and Katsuya Shimizu. Materials informatics based on evolutionary algorithms: Application to search for superconducting hydrogen compounds. *Phys. Rev. B*, 100(17):174506, nov 2019.

[106] P. Song, Z. Hou, P. Castro, K. Nakano, Kenta Hongo, Y. Takano, and R. Maezono. High-T_c ternary metal hydrides, YKH_{12} and $LaKH_{12}$, discovered by machine learning. *arXiv preprint arXiv:2103.00193*, 2021.

[107] Dmitrii V. Semenok, Ivan A. Troyan, Anna G. Ivanova, Alexander G. Kvashnin, Ivan A. Kruglov, Michael Hanfland, Andrey V. Sadakov, Oleg A. Sobolevskiy, Kirill S. Pervakov, Igor S. Lyubutin, Konstantin V. Glazyrin, Nico Giordano, Denis N. Karimov, Alexander L. Vasiliev, Ryosuke Akashi, Vladimir M. Pudalov, and Artem R. Oganov. Superconductivity at 253 k in lanthanum yttrium ternary hydrides. *Mater. Today*, 48:18–28, sep 2021.

[108] G. Kresse and J. Hafner. Ab initio molecular dynamics for liquid metals. *Phys. Rev. B*, 47(1):558–561, jan 1993.

[109] G. Kresse and J. Hafner. Ab initio molecular-dynamics simulation of the liquid-metal–amorphous-semiconductor transition in germanium. *Phys. Rev. B*, 49(20):14251–14269, may 1994.

[110] G. Kresse and J. Furthmüller. Efficient iterative schemes for ab initio total-energy calculations using a plane-wave basis set. *Phys. Rev. B*, 54(16):11169–11186, oct 1996.

[111] John P. Perdew, Kieron Burke, and Matthias Ernzerhof. Generalized gradient approximation made simple. *Phys. Rev. Lett.*, 77(18):3865–3868, oct 1996.

[112] Kousuke Nakano, Kenta Hongo, and Ryo Maezono. Investigation into structural phase transitions in layered titanium-oxypnictides by a computational phonon analysis. *Inorg. Chem.*, 56(22):13732–13740, nov 2017.

[113] Kousuke Nakano, Kenta Hongo, and Ryo Maezono. Phonon dispersions and fermi surfaces nesting explaining the variety of charge ordering in titanium-oxypnictides superconductors. *Sci. Rep.*, 6(1):29661, jul 2016.

[114] Nicola Marzari, David Vanderbilt, Alessandro De Vita, and M. C. Payne. Thermal contraction and disordering of the al(110) surface. *Phys. Rev. Lett.*, 82(16):3296–3299, apr 1999.

[115] Hui Wang, John S. Tse, Kaori Tanaka, Toshiaki Iitaka, and Yanming Ma. Superconductive sodalite-like clathrate calcium hydride at high pressures. *Proceedings of the National Academy of Sciences*, 109(17):6463–6466, apr 2012.

[116] Xiao hui Wang, Fa wei Zheng, Zhuo wei Gu, Fu li Tan, Jian heng Zhao, Cang li Liu, Cheng wei Sun, Jian Liu, and Ping Zhang. Hydrogen clathrate structures in uranium hydrides at high pressures. *ACS Omega*, 6(5):3946–3950, jan 2021.

[117] Nilesh P. Salke, M. Mahdi Davari Esfahani, Youjun Zhang, Ivan A. Kruglov, Jianshi Zhou, Yaguo Wang, Eran Greenberg, Vitali B. Prakapenka, Jin Liu, Artem R.

Oganov, and Jung-Fu Lin. Synthesis of clathrate cerium superhydride CeH9 at 80-100 GPa with atomic hydrogen sublattice. *Nat. Commun.*, 10(1):4453, oct 2019.

[118] Anubhav Jain, Shyue Ping Ong, Geoffroy Hautier, Wei Chen, William Davidson Richards, Stephen Dacek, Shreyas Cholia, Dan Gunter, David Skinner, Gerbrand Ceder, and Kristin A. Persson. Commentary: The materials project: A materials genome approach to accelerating materials innovation. *APL Materials*, 1(1):011002, jul 2013.

[119] Joseph I Goldstein, Dale E Newbury, Joseph R Michael, Nicholas WM Ritchie, John Henry J Scott, and David C Joy. *Scanning electron microscopy and X-ray microanalysis*. Springer, 2017.

[120] G. Kresse and J. Furthmüller. Efficient iterative schemes for ab initio total-energy calculations using a plane-wave basis set. *Phys. Rev. B*, 54(16):11169–11186, oct 1996.

[121] Stefan Maintz, Volker L. Deringer, Andrei L. Tchougréeff, and Richard Dronskowski. LOBSTER: A tool to extract chemical bonding from plane-wave based DFT. *J. Comput. Chem.*, 37(11):1030–1035, feb 2016.

[122] Hanyu Liu, Ivan I. Naumov, Roald Hoffmann, N. W. Ashcroft, and Russell J. Hemley. Potential high-tc superconducting lanthanum and yttrium hydrides at high pressure. *Proceedings of the National Academy of Sciences*, 114(27):6990–6995, jun 2017.

[123] Xiaolei Feng, Jurong Zhang, Guoying Gao, Hanyu Liu, and Hui Wang. Compressed sodalite-like mgh6 as a potential high-temperature superconductor. *RSC Advances*, 5(73):59292–59296, 2015.

[124] P Giannozzi, O Andreussi, T Brumme, O Bunau, M Buongiorno Nardelli, M Calandra, R Car, C Cavazzoni, D Ceresoli, M Cococcioni, N Colonna, I Carnimeo, A Dal Corso, S de Gironcoli, P Delugas, R A DiStasio, A Ferretti, A Floris, G Fratesi,

G Fugallo, R Gebauer, U Gerstmann, F Giustino, T Gorni, J Jia, M Kawamura, H-Y Ko, A Kokalj, E Küçükbenli, M Lazzeri, M Marsili, N Marzari, F Mauri, N L Nguyen, H-V Nguyen, A Otero de-la Roza, L Paulatto, S Poncé, D Rocca, R Sabatini, B Santra, M Schlipf, A P Seitsonen, A Smogunov, I Timrov, T Thonhauser, P Umari, N Vast, X Wu, and S Baroni. Advanced capabilities for materials modelling with quantum ESPRESSO. *J. Phys.: Condens. Matter*, 29(46):465901, oct 2017.

[125] Paolo Giannozzi, Oscar Baseggio, Pietro Bonfà, Davide Brunato, Roberto Car, Ivan Carnimeo, Carlo Cavazzoni, Stefano de Gironcoli, Pietro Delugas, Fabrizio Ferrari Ruffino, Andrea Ferretti, Nicola Marzari, Iurii Timrov, Andrea Urru, and Stefano Baroni. Quantum espresso toward the exascale. *The Journal of Chemical Physics*, 152(15):154105, apr 2020.

[126] Shifeng Qian, Xiaowei Sheng, Xiaozhen Yan, Yangmei Chen, and Bo Song. Theoretical study of stability and superconductivity ofschn(n=4–8) at high pressure. *Phys. Rev. B*, 96(9):094513, sep 2017.

[127] Xiaoqiu Ye, Niloofar Zarifi, Eva Zurek, Roald Hoffmann, and N. W. Ashcroft. High hydrides of scandium under pressure: Potential superconductors. *The Journal of Physical Chemistry C*, 122(11):6298–6309, feb 2018.

[128] David C. Lonie, James Hooper, Bahadir Altintas, and Eva Zurek. Metallization of magnesium polyhydrides under pressure. *Phys. Rev. B*, 87(5):054107, feb 2013.

[129] Qiuxiang Liu, Changzeng Fan, and Ruijun Zhang. First-principles study of high-pressure structural phase transitions of magnesium. *J. Appl. Phys.*, 105(12):123505, jun 2009.

[130] Yuichi Akahama, Hiroshi Fujihisa, and Haruki Kawamura. New helical chain structure for scandium at 240 GPa. *Phys. Rev. Lett.*, 94(19):195503, may 2005.

[131] Mari Einaga, Masafumi Sakata, Takahiro Ishikawa, Katsuya Shimizu, Mikhail I. Eremets, Alexander P. Drozdov, Ivan A. Troyan, Naohisa Hirao, and Yasuo Ohishi. Crystal structure of the superconducting phase of sulfur hydride. *Nat. Phys.*, 12(9):835–838, may 2016.

[132] A. Jayaraman. Ultrahigh pressures. *Rev. Sci. Instrum.*, 57(6):1013–1031, jun 1986.

[133] A. Ohmura, A. Machida, T. Watanuki, K. Aoki, S. Nakano, and K. Takemura. Pressure-induced structural change from hexagonal to fcc metal lattice in scandium trihydride. *J. Alloys Compd.*, 446-447:598–602, oct 2007.

[134] Tetsuji Kume, Hiroyuki Ohura, Tomoo Takeichi, Ayako Ohmura, Akihiko Machida, Tetsu Watanuki, Katsutoshi Aoki, Shigeo Sasaki, Hiroyasu Shimizu, and Kenichi Takemura. High-pressure study of sch3: Raman, infrared, and visible absorption spectroscopy. *Phys. Rev. B*, 84(6):064132, aug 2011.

[135] Mengyao Shao, Su Chen, Wuhao Chen, Kexin Zhang, Xiaoli Huang, and Tian Cui. Superconducting sch3 and luh3 at megabar pressures. *Inorg. Chem.*, 60(20):15330–15335, sep 2021.

[136] M Bortz, B Bertheville, G Böttger, and K Yvon. Structure of the high pressure phase mgh2 by neutron powder diffraction. *J. Alloys Compd.*, 287(1-2):L4–L6, jun 1999.

[137] P. Vajeeston, P. Ravindran, B. C. Hauback, H. Fjellvåg, A. Kjekshus, S. Furuseth, and M. Hanfland. Structural stability and pressure-induced phase transitions in-mgh2. *Phys. Rev. B*, 73(22):224102, jun 2006.

[138] Xiaoqiu Ye, Roald Hoffmann, and N. W. Ashcroft. Theoretical study of phase separation of scandium hydrides under high pressure. *The Journal of Physical Chemistry C*, 119(10):5614–5625, feb 2015.

[139] Kazutaka Abe. Hydrogen-rich scandium compounds at high pressures. *Phys. Rev. B*, 96(14):144108, oct 2017.

[140] Yong-Kai Wei, Jiao-Nan Yuan, Faez Iqbal Khan, Guang-Fu Ji, Zhuo-Wei Gu, and Dong-Qing Wei. Pressure induced superconductivity and electronic structure properties of scandium hydrides using first principles calculations. *RSC Advances*, 6(85):81534–81541, 2016.

[141] Arndt Simon. Superconductivity and chemistry. *Angewandte Chemie International Edition in English*, 36(17):1788–1806, sep 1997.

[142] J. Bardeen, L. N. Cooper, and J. R. Schrieffer. Microscopic theory of superconductivity. *Phys. Rev.*, 106(1):162–164, apr 1957.

[143] Duck Young Kim, Ralph H. Scheicher, and Rajeev Ahuja. Predicted high-temperature superconducting state in the hydrogen-dense transition-metal hydrideyh3at 40 k and 17.7 gpa. *Phys. Rev. Lett.*, 103(7):077002, aug 2009.

[144] Michael Tinkham. *Introduction to superconductivity*. Courier Corporation, 2004.

[145] P. G. De Gennes. *Superconductivity of Metals and Alloys*. CRC Press, March 2018.

[146] Jacob Linder and Jason W. A. Robinson. Superconducting spintronics. *Nat. Phys.*, 11(4):307–315, apr 2015.

[147] B.D. Josephson. Possible new effects in superconductive tunnelling. *Physics Letters*, 1(7):251–253, jul 1962.

[148] Anne Bergen, Rasmus Andersen, Markus Bauer, Hermann Boy, Marcel ter Brake, Patrick Brutsaert, Carsten Bührer, Marc Dhallé, Jesper Hansen, Herman ten Kate, Jürgen Kellers, Jens Krause, Erik Krooshoop, Christian Kruse, Hans Kylling, Martin Pilas, Hendrik Pütz, Anders Rebsdorf, Michael Reckhard, Eric Seitz, Helmut Springer, Xiaowei Song, Nir Tzabar, Sander Wessel, Jan Wiezoreck, Tiemo Winkler, and Konstantin Yagotyntsev. Design and in-field testing of the world's first ReBCO rotor for a 3.6 MW wind generator. *Supercond. Sci. Technol.*, 32(12):125006, oct 2019.

[149] Md. Rabiul Islam, Youguang Guo, and Jianguo Zhu. A review of offshore wind turbine nacelle: Technical challenges, and research and developmental trends. *Renewable Sustainable Energy Rev.*, 33:161–176, may 2014.

[150] Heiko Thomas, Adela Marian, Alexander Chervyakov, Stefan Stückrad, Delia Salmieri, and Carlo Rubbia. Superconducting transmission lines – sustainable electric energy transfer with higher public acceptance? *Renewable Sustainable Energy Rev.*, 55:59–72, mar 2016.

[151] M. Tinkham. Resistive transition of high-temperature superconductors. *Phys. Rev. Lett.*, 61(14):1658–1661, oct 1988.

[152] Swarn S Kalsi. *Applications of high temperature superconductors to electric power equipment*. John Wiley & Sons, 2011.

[153] J. Bardeen. Theory of the meissner effect in superconductors. *Phys. Rev.*, 97(6):1724–1725, mar 1955.

[154] Leon N. Cooper. Bound electron pairs in a degenerate fermi gas. *Phys. Rev.*, 104(4):1189–1190, nov 1956.

[155] J. Bardeen, L. N. Cooper, and J. R. Schrieffer. Theory of superconductivity. *Phys. Rev.*, 108(5):1175–1204, dec 1957.

[156] E. Wigner and H. B. Huntington. On the possibility of a metallic modification of hydrogen. *The Journal of Chemical Physics*, 3(12):764–770, dec 1935.

[157] P. Loubeyre, R. LeToullec, D. Hausermann, M. Hanfland, R. J. Hemley, H. K. Mao, and L. W. Finger. X-ray diffraction and equation of state of hydrogen at megabar pressures. *Nature*, 383(6602):702–704, oct 1996.

[158] Jeremy McMinis, Raymond C. Clay, Donghwa Lee, and Miguel A. Morales. Molecular to atomic phase transition in hydrogen under high pressure. *Phys. Rev. Lett.*, 114(10):105305, mar 2015.

[159] M. I. Eremets and I. A. Troyan. Conductive dense hydrogen. *Nat. Mater.*, 10(12):927–931, nov 2011.

[160] Philip Dalladay-Simpson, Ross T. Howie, and Eugene Gregoryanz. Evidence for a new phase of dense hydrogen above 325 gigapascals. *Nature*, 529(7584):63–67, jan 2016.

[161] Ranga P. Dias and Isaac F. Silvera. Observation of the wigner-huntington transition to metallic hydrogen. *Science*, 355(6326):715–718, feb 2017.

[162] Davide Castelvecchi. Physicists doubt bold report of metallic hydrogen. *Nature*, 542(7639):17–17, feb 2017.

[163] Peter M. Celliers, Marius Millot, Stephanie Brygoo, R. Stewart McWilliams, Dayne E. Fratanduono, J. Ryan Rygg, Alexander F. Goncharov, Paul Loubeyre, Jon H. Eggert, J. Luc Peterson, Nathan B. Meezan, Sebastien Le Pape, Gilbert W. Collins, Raymond Jeanloz, and Russell J. Hemley. Insulator-metal transition in dense fluid deuterium. *Science*, 361(6403):677–682, aug 2018.

[164] Xiaofeng Li and Feng Peng. Superconductivity of pressure-stabilized vanadium hydrides. *Inorg. Chem.*, 56(22):13759–13765, nov 2017.

[165] Shuyin Yu, Xiaojing Jia, Gilles Frapper, Duan Li, Artem R. Oganov, Qingfeng Zeng, and Litong Zhang. Pressure-driven formation and stabilization of superconductive chromium hydrides. *Sci. Rep.*, 5(1):17764, dec 2015.

[166] Wuhao Chen, Dmitrii V. Semenok, Alexander G. Kvashnin, Xiaoli Huang, Ivan A. Kruglov, Michele Galasso, Hao Song, Defang Duan, Alexander F. Goncharov, Vitali B. Prakapenka, Artem R. Oganov, and Tian Cui. Synthesis of molecular metallic barium superhydride: pseudocubic BaH12. *Nat. Commun.*, 12(1):273, jan 2021.

[167] Mengyao Shao, Wuhao Chen, Kexin Zhang, Xiaoli Huang, and Tian Cui. High-pressure synthesis of superconducting clathratelike yh4. *Phys. Rev. B*, 104(17):174509, nov 2021.

[168] Wuhao Chen, Dmitrii V. Semenok, Xiaoli Huang, Haiyun Shu, Xin Li, Defang Duan, Tian Cui, and Artem R. Oganov. High-temperature superconducting phases in cerium superhydride with a tc up to 115 k below a pressure of 1 megabar. *Phys. Rev. Lett.*, 127(11):117001, sep 2021.

[169] Yinwei Li, Jian Hao, Hanyu Liu, Yanling Li, and Yanming Ma. The metallization and superconductivity of dense hydrogen sulfide. *The Journal of Chemical Physics*, 140(17):174712, may 2014.

[170] Peng Song, Zhufeng Hou, Pedro Baptista de Castro, Kousuke Nakano, Kenta Hongo, Yoshihiko Takano, and Ryo Maezono. High-tc superconducting hydrides formed by lah24 and yh24 cage structures as basic blocks. *Chem. Mater.*, 33(24):9501–9507, dec 2021.

[171] Jiang Zheng, Weiguo Sun, Xilong Dou, Ai-Jie Mao, and Cheng Lu. Pressure-driven structural phase transitions and superconductivity of ternary hydride mgvh6. *The Journal of Physical Chemistry C*, 125(5):3150–3156, jan 2021.

[172] Lan-Ting Shi, Yong-Kai Wei, A-Kun Liang, Robin Turnbull, Cai Cheng, Xiang-Rong Chen, and Guang-Fu Ji. Prediction of pressure-induced superconductivity in the novel ternary system sccah2n (n = 1–6). *J. Mater. Chem. C*, 9(23):7284–7291, 2021.

[173] Peng Song, Zhufeng Hou, Pedro Baptista de Castro, Kousuke Nakano, Kenta Hongo, Yoshihiko Takano, and Ryo Maezono. High-tc superconducting hydrides formed by lah24 and yh24 cage structures as basic blocks. *Chem. Mater.*, 33(24):9501–9507, dec 2021.

[174] Xiaowei Liang, Shutao Zhao, Cancan Shao, Aitor Bergara, Hanyu Liu, Linyan Wang, Rongxin Sun, Yang Zhang, Yufei Gao, Zhisheng Zhao, Xiang-Feng Zhou, Julong He, Dongli Yu, Guoying Gao, and Yongjun Tian. First-principles study of crystal structures and superconductivity of ternary ysh6 and lash6 at high pressures. *Phys. Rev. B*, 100(18):184502, nov 2019.

[175] Meng-Jing Jiang, Hui-Li Tian, Yu-Long Hai, Ning Lu, Pei-Fei Tong, Shuang-Yuan Wu, Wen-Jie Li, Chun-Lei Yang, and Guo-Hua Zhong. Phonon-mediated low-pressure superconductivity in ternary hydride ba–ch4. *ACS Applied Electronic Materials*, 3(9):4172–4179, sep 2021.

[176] Simone Di Cataldo, Wolfgang von der Linden, and Lilia Boeri. Phase diagram and superconductivity of calcium borohyrides at extreme pressures. *Phys. Rev. B*, 102(1):014516, jul 2020.

[177] Simone Di Cataldo, Wolfgang von der Linden, and Lilia Boeri. First-principles search of hot superconductivity in la-x-h ternary hydrides. *npj Comput. Mater.*, 8(1):2, jan 2022.

[178] R. Vocaturo, C. Tresca, G. Ghiringhelli, and G. Profeta. Prediction of ambient-pressure superconductivity in ternary hydride pdcuhx. *J. Appl. Phys.*, 131(3):033903, jan 2022.

[179] J. E. Hirsch and F. Marsiglio. Unusual width of the superconducting transition in a hydride. *Nature*, 596(7873):E9–E10, aug 2021.

[180] J. E. Hirsch. Comment on "room-temperature superconductivity in a carbonaceous sulfur hydride" by elliot snider et al. *Europhys. Lett.*, 137(3):36001, feb 2022.

[181] Maximilian Amsler. Thermodynamics and superconductivity of sxse1-xh3. *Phys. Rev. B*, 99(6):060102, feb 2019.

[182] Hongyi Guan, Ying Sun, and Hanyu Liu. Superconductivity of h3s doped with light elements. *Physical Review Research*, 3(4):043102, nov 2021.

[183] Wuhao Chen, Xiaoli Huang, Dmitrii V Semenok, Su Chen, Kexin Zhang, Artem R Oganov, and Tian Cui. Enhancement of superconducting critical temperature realized in la-ce-h system at moderate pressures. *arXiv preprint arXiv:2203.14353*, 2022.

[184] Andriy O. Lyakhov, Artem R. Oganov, Harold T. Stokes, and Qiang Zhu. New developments in evolutionary structure prediction algorithm USPEX. *Comput. Phys. Commun.*, 184(4):1172–1182, apr 2013.

[185] G. Kresse and D. Joubert. From ultrasoft pseudopotentials to the projector augmented-wave method. *Phys. Rev. B*, 59(3):1758–1775, jan 1999.

[186] Iurii Timrov, Nicola Marzari, and Matteo Cococcioni. Hp–a code for the calculation of hubbard parameters using density-functional perturbation theory. *arXiv preprint arXiv:2203.15684*, 2022.

[187] Yue Chen, Qing-Miao Hu, and Rui Yang. Predicted suppression of the superconducting transition of new high-pressure yttrium phases with increasing pressure from first-principles calculations. *Phys. Rev. Lett.*, 109(15):157004, oct 2012.

[188] Yogesh K. Vohra, Steven L. Beaver, Jagannadham Akella, Chantel A. Ruddle, and Samuel T. Weir. Ultrapressure equation of state of cerium metal to 208 GPa. *J. Appl. Phys.*, 85(4):2451–2453, feb 1999.

[189] Ling Chen, Tianxiao Liang, Zihan Zhang, Hao Song, Zhengtao Liu, Qiwen Jiang, Yue Chen, and Defang Duan. Phase transitions and properties of lanthanum under high pressures. *J. Phys.: Condens. Matter*, 34(20):204005, mar 2022.

[190] A. R. Akbarzadeh, V. Ozoliņš, and C. Wolverton. First-principles determination of multicomponent hydride phase diagrams: Application to the li-mg-n-h system. *Adv. Mater.*, 19(20):3233–3239, sep 2007.

[191] Pauli Virtanen, , Ralf Gommers, Travis E. Oliphant, Matt Haberland, Tyler Reddy, David Cournapeau, Evgeni Burovski, Pearu Peterson, Warren Weckesser, Jonathan Bright, Stéfan J. van der Walt, Matthew Brett, Joshua Wilson, K. Jarrod Millman, Nikolay Mayorov, Andrew R. J. Nelson, Eric Jones, Robert Kern, Eric Larson, C J Carey, İlhan Polat, Yu Feng, Eric W. Moore, Jake VanderPlas, Denis Laxalde, Josef Perktold, Robert Cimrman, Ian Henriksen, E. A. Quintero, Charles R. Harris,

Anne M. Archibald, Antônio H. Ribeiro, Fabian Pedregosa, and Paul van Mulbregt. Author correction: SciPy 1.0: fundamental algorithms for scientific computing in python. *Nat. Methods*, 17(3):352–352, feb 2020.

[192] Andrea Dal Corso. Pseudopotentials periodic table: From h to pu. *Computational Materials Science*, 95:337–350, dec 2014.

[193] Francesco Belli, Trinidad Novoa, J. Contreras-García, and Ion Errea. Strong correlation between electronic bonding network and critical temperature in hydrogen-based superconductors. *Nat. Commun.*, 12(1):5381, sep 2021.

[194] Jingkai Bi, Yuki Nakamoto, Katsuya Shimizu, Mi Zhou, Hongbo Wang, Guangtao Liu, and Yanming Ma. Efficient route to achieve superconductivity improvement via substitutional lace alloy superhydride at high pressure. *arXiv preprint arXiv:2204.04623*, 2022.

[195] Ge Huang, Tao Luo, Philip Dalladay Simpson, LiuCheng Chen, ZiYu Cao, Di Peng, Federico A Gorelli, GuoHua Zhong, HaiQing Lin, and XiaoJia Chen. Synthesis of superconducting phase of la0.5ce0.5h10 at high pressures. *arXiv preprint arXiv:2208.05199*, 2022.

[196] LiuCheng Chen, Tao Luo, Philip Dalladay Simpson, Ge Huang, ZiYu Cao, Di Peng, Federico Aiace Gorelli, GuoHua Zhong, HaiQing Lin, and XiaoJia Chen. Synthesis and superconductivity in yttriumcerium hydrides at moderate pressures. *arXiv preprint arXiv:2208.05191*, 2022.

[197] Peng Song, Zhufeng Hou, Pedro Baptista de Castro, Kousuke Nakano, Kenta Hongo, Yoshihiko Takano, and Ryo Maezono. The systematic study on the stability and superconductivity of Y-Mg-H compounds under high pressure. *arXiv preprint arXiv:2107.05498*, 2021.

Publications

International journal

[1] D. Kato, P. Song, H. Ubukata, H. Taguro, C. Tassel, K. Miyazaki, T. Abe, K. Nakano, K. Hongo, R. Maezono, H. Kageyama, Angew. Chem. Int. Ed. (2023).(In press)

[2] P. Song, M. Khawakuch, Y. Masubuchi, K. Oqmhsla, K. Nakano, R. Maezono, K. Hongo, Comput. Mater. Sci., 226, 112202 (2023).

[3] P. Song, Z. Hou, K. Nakano, K. Hongo and R. Maezono, Mater. Today Phys., 28,100873 (2022).

[4] Y. Masubuchi, S. Miyazaki, P. Song, T. Yamamoto, K. Nakano, K. Hongo and R. Maezono, J. Alloys Compd., 918, 165632 (2022).

[5] P. Song, Z. Hou, P. B. de Castro, K. Nakano, K. Hongo, Y. Takano and R. Maezono, J. Phys. Chem. C., 125, 2747-2755 (2022).

[6] P. Song, Z. Hou, P. B. de Castro, K. Nakano, Y. Takano, R. Maezono and K. Hongo, Adv. Theory Simul., 2100364 (2022).

[7] P. Song, Z. Hou, P. B. de Castro, K. Nakano, K. Hongo, Y. Takano and R. Maezono, Chem. Mater., 33, 9501 (2021).

Domestic conferences

- P. Song, K. Nakano, Y. Takano, R. Maezono, and K. Hongo, "Potential high-Tc superconductivity in $YCeH_x$ and $LaCeH_x$ under pressure," The 83rd Autumn Meeting of the Physical Society of Japan, Sep. 21, 2022, Tohoku University, Kawauchi Campus, (Physical Society of Japan/Oral/Not peer-reviewed)
- P. Song, K. Nakano, Y. Takano, R. Maezono, and K. Hongo, "High-pressure Mg-Sc-H phase diagram and its superconductivity from first-principles calculations," The 5th International Conference of Young Researchers on Advanced Materials, Mar. 6, 2022, Centennial Hull, Kyushu University, (ICYRAM/Oral/Not peer-reviewed)
- P. Song, K. Nakano, Y. Takano, R. Maezono, and K. Hongo, "The systematic study on the stability and superconductivity of Y-Mg-H compounds under high pressure," The 69th Spring Meeting of the Physical Society of Japan, Mar. 23, 2022, Aoyama Gakuin University, Sagamihara Campus, (Physical Society of Japan/Oral/Not peer-reviewed)
- P. Song, K. Nakano, Y. Takano, R. Maezono, and K. Hongo, "High-T_c superconducting hydrides formed by LaH_{24} and YH_{24} cage structures as basic blocks," The 77th Spring Meeting of the Physical Society of Japan, Mar. 17, 2022, Online Conference, (Physical Society of Japan/Oral/Not peer-reviewed)

Acknowledge

At the end of this thesis, I would like to express my heartfelt gratitude to everyone who has contributed to my research. First and foremost, I would like to thank Professor Maezono for his guidance and support. During the JSPS grant application process, Professor Maezono provided me with invaluable assistance. Moreover, I am grateful to Professor Hongo for inviting me to join the $BaCN_2$ research project.

I am also appreciative of Professor Maezono for introducing me to numerous collabo-

rative supervisors, enhancing my personal experience, and helping me establish many new collaborative projects. I would like to thank Nakano-sensei for his professional guidance in superconducting T_c calculations and Hou-san for his help in writing the paper and discussing research topics. I would also like to thank the laboratory secretaries for their significant assistance and guidance in the application process. I am particularly grateful to Professor Maezono for taking me to the hospital when I was ill (during my facial paralysis) and providing me with care and support.

Lastly, I would like to thank the Japan Society for the Promotion of Science (JSPS) for their financial support during my doctoral studies, which allowed me to focus on my research work. The completion of this thesis would not have been possible without the support and help of all these people, and I express my heartfelt gratitude to them once again.